Summer 2015

Computing and the electrical transport properties of coupled quantum networks

Casey Andrew Cain

Department: Electrical and Computer Engineering

COMPUTING AND THE ELECTRICAL TRANSPORT PROPERTIES OF COUPLED QUANTUM NETWORKS

by

CASEY ANDREW CAIN

A DISSERTATION

Presented to the Faculty of the Graduate School of the

MISSOURI UNIVERSITY OF SCIENCE AND TECHNOLOGY

In Partial Fulfillment of the Requirements for the Degree

DOCTOR OF PHILOSOPHY

in

COMPUTER ENGINEERING

2015

Approved by

Dr. Cheng-Hsiao Wu, Advisor
Dr. Daryl Beetner
Dr. James Drewniak
Dr. Jun Fan
Dr. Paul Parris

PUBLICATION DISSERTATION OPTION

This dissertation has been prepared in the form of four papers.

Paper 1. Pages 8–30 have been published as *Scaling relations and the role of bond-charge to the electron transmission through two coupled Aharonov-Bohm rings*, Journal of Applied Physics **111** 094304 (2012) with C. H. Wu and L. Tran.

Paper 2. Pages 31–48 have been published as *Quantum network theory of computing with respect to entangled flux qubits and external perturbation*, Journal of Applied Physics **113** 154309 (2013) with C. H. Wu.

Paper 3. Pages 49–64 have been published as *Thévenin equivalence in disorderless quantum networks*, Journal of Applied Physics **117** 024308 (2015) with C. H. Wu.

Paper 4. Pages 65–85 have been submitted as *Sixteen two-variable Boolean functions from quantum networks of Aharonov-Bohm rings* to Journal of Applied Physics (2015).

ABSTRACT

In this dissertation a number of investigations were conducted on ballistic quantum networks in the mesoscopic range. In this regime, the wave nature of electron transport under the influence of transverse magnetic fields leads to interesting applications for digital logic and computing circuits. The work specifically looks at characterizing a few main areas that would be of interest to experimentalists who are working in nanostructure devices, and is organized as a series of papers. The first paper analyzes scaling relations and normal mode charge distributions for such circuits in both isolated and open (terminals attached) form. The second paper compares the flux-qubit nature of quantum networks to the well-established spintronics theory. The results found exactly contradict the conventional school of thought for what is required for quantum computation. The third paper investigates the requirements and limitations of extending the Thévenin theorem in classic electric circuits to ballistic quantum transport. The fourth paper outlines the optimal functionally complete set of quantum circuits that can completely satisfy all sixteen Boolean logic operations for two variables.

ACKNOWLEDGMENTS

There are many special people who I would like to thank for helping me along this journey. The first, my wife Stephanie, has always been loving and supportive of my goals and studies. Without her, there is no way I could have made it this far. Secondly, I would like to thank my family for being understanding of all of the missed times and infrequent visits as a sacrifice of my studies. Thirdly, I would like to thank my advisor Dr. Wu for providing a wonderful and stimulating research problem to investigate. His kindness, guidance, and mentorship have been crucial in helping me grow both professionally and personally as a researcher. I would also like to thank many of the great faculty I have had the chance to work with and learn from over the years. In the ECE department, I would like to thank Drs. Fan, Beetner, DuBroff, Stanley, and Watkins for teaching some of my program of study and assisting the graduate students. Additionally, I received a lot of support and training from the Physics department. Dr. Parris is thanked for teaching quantum mechanical fundamentals and being available to help with research questions. Dr. Hale is thanked for teaching advanced mathematics and electrodynamics, particularly for Green's functions and complex analysis. Dr. Vojta is thanked for extending his solid-state physics and numerical methods knowledge. I would also like to specifically thank the ECE Department, notably Dr. Erickson, for providing very generous department funding and giving me the opportunity to build a teaching portfolio during my studies in Rolla. I would finally like to thank the Office of Graduate Studies for providing scholarship funding through the Chancellor's Fellowship program. Without these two funding sources, I would not have been able to begin and successfully complete this research and degree.

TABLE OF CONTENTS

Page

LIST OF ILLUSTRATIONS

LIST OF TABLES

1. INTRODUCTION

1.1. STRUCTURE OF DISSERTATION

As this dissertation consists of a collection of journal publications, it is important to establish a base background for the research to help make the transitions between each chapter logical and smooth. This work focuses on the problem of scaling down traditional semiconductor process technologies into the nanoscale range. As the feature sizes get smaller and smaller, undesirable parasitic and quantum mechanical effects begin to dominate for traditional transistor and memory architectures. At this point, a logical question could be whether new circuits can instead leverage these quantum mechanical effects to their advantage to create new and unique devices. Regardless of the operating mechanisms, any practical device needs to be able to be fabricated with processes that are not radically different from how current CMOS devices are constructed. In addition to being physically smaller, hence faster operating frequencies, another goal is to simplify how the devices are used to form logic gates and arithmetic logic units. Parallel processing, the breaking down of sequential calculations into separate jobs, needs to be a main focal point at the hardware level. Optical computing was one of the first unique architectures that attempted to move the field forward. It employed a number of focused light-emitting sources, lenses, and polarizing filters to construct logic gates and memories. It was able to perform parallel Boolean logic in a simpler manner than static or dynamic CMOS transistor implementations. Unfortunately, the field largely died out because of the impracticalities of size and cost of such schemes. Quantum computing, or spintronics, was the next big idea to come along. Its foundation is built on the idea of preparing a closed system of N qubits (bits in a $|0\rangle$ or $|1\rangle$ state simultaneously) in

a superposition that can then be operated on with unitary (reversible) gates. These gates simply rotate the system in the state space spanned by the basis of the direct product ($|\psi_1\rangle \otimes |\psi_2\rangle \otimes ... |\psi_N\rangle$) and entangled states. The idea, mathematically speaking, is that every single input/output possibility for the operation exists at once. When the system is measured, the state collapses to a single state with a given probability. The trick is then to attempt to figure out how to measure such a system to give the answer(s) to the computation that is desired. This has proven to be extremely difficult; to date there are no experimental devices that can do even basic Boolean algebra. One conjecture of why, considered in a paper in this dissertation, is how the fundamental unit, the qubit, and the measurement process are treated as separate and independent processes.

A newer alternative to spintronics computing is quantum network circuits. A quantum network can be considered as a quasi-1D construction of electron waveguides that are arranged into small loops at the nanoscale. An example of this is shown in Fig. 1.1. At this size, the charge transport (conductance) is highly dependent upon the discrete energy states of the carrier. The electron behaves like a wave packet, and hence undergoes many elastic scattering events as it transports through the network. Furthermore, when a magnetic field is normal and present to the electron's wavevector $\vec{k}$, the wave picks up an additional phase factor. By tuning the magnetic field's magnitude and direction, it is possible to control the constructive/destructive interference effects in the network. This is called the Aharonov-Bohm (AB) effect and was first predicted in 1959 [2]. This is similar to the Mach-Zehnder effect in electro-optics [3]. This effect is the basis for this type of computing and was first proposed by Wu [4]. Later on, a half-adder circuit that operated on this principle was proposed by Cain and Wu [1]. This dissertation focuses on developing more in-depth investigations into these circuits and help establish foundational work in this

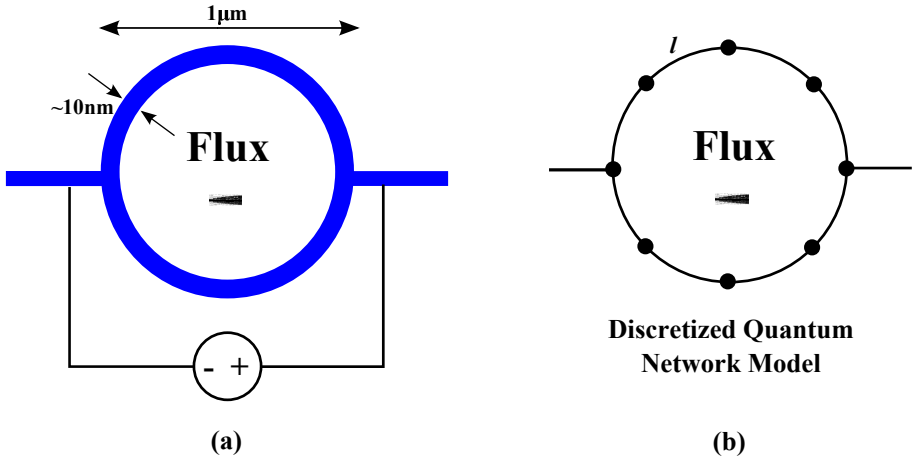

Figure 1.1: (a) A typical quasi-1D quantum network, an AB ring, in a two terminal setup. The loop diameter is typically up to a micron, and is much larger than the thickness. This constricts the various electronic modes to their fundamental mode, much like is done for classical rectangular waveguides. A magnetic flux Φ is assumed to be present and penetrating the ring. (b) A discrete quantum network model that represents that of the continuous ring. The scattering sites (dots) have equal lattice spacings l. This model allows for good approximation for a defect and disorder-free network within the coherence limit.

area. In order to assist the reader, a more complete set of derivations based on the original work in Ref. [4] is provided in Appendix A.

A first area of interest was to numerically investigate the scaling relations of the lowest-order mode of a given quantum network, and determine their operating characteristics as they are enlarged to the microscopic scale. At the same time, how the electric charge distributes itself in a quantum network can have important implications for potential applications such as memory cells. Both of these topics are outlined and discussed in the first paper of this work.

Another important topic to attract interest to quantum networks was to thoroughly investigate its relation to spintronics. A single AB loop at zero flux can be considered as a flux-qubit, whose angular momentum vector is in a superposition of spin-up or spin-down states. Two loops are then coupled (entangled) together. This

coupling is then paired with varying measurement strengths to determine how the transport and logic gate operations are affected. The published results were then compared and contrasted in the second paper.

Conventional electric circuits can be characterized by Thévenin and Norton equivalent models. An interesting area that had yet to be explored was whether it was possible to extend these concepts to much more restrictive quantum mechanical models such as previously proposed quantum circuits. It was obvious that the theorems would not universally apply, however the main goal was to identify the set of requirements that need to be fulfilled, and unique examples that satisfy them. These were the subject of the third paper.

While basic inverting and half-adder circuits have already been demonstrated, a minimal functionally complete set of quantum circuits had not yet been proposed to perform each of the sixteen possible Boolean algebraic operations on two input operands. The fourth paper focuses on finding the optimal set of four different circuits that are able to satisfy all these operations. Each circuit is capable of performing multiple jobs by simply changing the biasing of the magnetic fluxes to each circuit.

In the subsequent section, a brief review of the current state of the art for these nanotechnologies is given. This focuses on current fabrication schemes, experimental setups, spintronic progress, and the future outlook of the field.

1.2. CURRENT STATE OF THE ART

1.2.1. AB Ring Technology. Aharonov-Bohm ring technologies have significantly advanced in the last few decades. The classic experiment was performed at IBM in the mid 1980s [5]. It consisted of a clean gold ring on the order of a micron in diameter used in a two-terminal setup. By Fourier transforming the measured magnetoresistance values that change as a function of flux, the predicted periodic

components hc/e and $hc/2e$ were recovered. As time moved on process technologies have increasingly turned to heterostructure devices. These devices consist of different elemental materials layered together or embedded (deposited) within one another, often being doped in specific ways to produce electronic band structures that are useful for the specific application. A very common example is sandwiching GaAs against AlGaAs (GaAs:AlGaAs). This results in a triangular quantum well that confines the electrons near the interface on the GaAs side. They are then free to move tangential to the interface, and make up what is commonly referred to as a 2D electron gas (2DEG). An alternative that also is used frequently is InGaAs:InAlAs, due to the very high carrier mobilities of InGaAs. In 2013 a $1300nm$ diameter ring of InGaAs:InAlAs was investigated [6]. Not only were the AB effects clearly observable at low temperature ($T = 400mK$), but the coherence length was approximately $3\mu m$. This allows the circuit to be accurately measured before the effects begin to wash out. Alternatively, a recent experiment looked at creating a ring by doping a planar phosphorous layer in silicon (Si:P) [7]. This is motivated due to the fact Si:P transports diffusively, and with very high carrier concentration. The particular ring structure was quite small at $85nm$. At $T = 100mK$ the coherence length was observed to be upwards of $100nm$, and thus can be useful for circuit outputs. Current experimental research continues to investigate different heterostructure, semiconducting (such as graphene), and dopant devices that can operate more efficiently.

1.2.2. Magnetic Flux Generation. One particular issue that makes constructing a practical device that operates on the AB effect difficult is how to physically build the components that generate the magnetic flux inputs to the circuit. In the previous subsection, the experimental results for rings of this size required magnetic flux densities in the mT range. Obviously, one possibility is to use a solenoidal setup or a Halbach array to generate a constant B-field. However, this is cumbersome and

inefficient when attempting to pair it with a nanodevice. One very recent development has been the fabrication of nanomagnets. Most recently in 2014, a relevant experimental implementation was realized [8]. Physically, they are constructed in a similar way as the AB ring circuits. They employ a substrate that insulates in the bulk but allows for surface current states, called a topological insulator. A very thin ferromagnetic film is then deposited on top of the substrate. A source and drain electrode configuration, much like an n/p-FET, is then implanted on either end of the substrate. When a potential source is connected, the surface current density $\vec{J}_s$ flowing across the boundary between the insulator and the ferromagnetic film induces a magnetization vector $\vec{M}$. By controlling the voltage bias an appropriate magnetic field up to $\approx 2T$ can be achieved, though typical values to drive the AB ring circuits need only be in the tens of mV range. A nanomagnet could then be placed above or below an AB ring to provide the necessary flux input to control the circuit.

1.2.3. Spintronics Progress. There are a variety of different spintronic-based technologies. One of the most common are superconducting quantum interference devices, or SQUID. They are formed into loops similar to an AB-based quantum network, but instead rely on two electrons as a result of the Cooper pairing. In each arm of the superconducting loop, there are thin insulating Josephson junctions. A magnetic field penetrates the loop and induces a persistent current, which in cooperation with the junctions can tune the interference effects. This current, also called a flux qubit, can be prepared in a state that is a superposition of clockwise-counterclockwise spins. In addition, by tuning the flux the energy gap spacing between states can be changed. This changes the coupling between the lowest two level states useful for computation. Experimental results have demonstrated an ability to entangle up to three qubits using this scheme [9]. However from an algorithm standpoint, a two-qubit device is the current limit [10]. One of the main algorithms that people want to solve, particularly for cryptography applications, is the Shor algorithm

for prime factorization [11]. In 2001, the first experimental demonstration of this was performed at IBM [12]. The algorithm relies on the use of the quantum Fourier transform (QFT) to repeatedly detect and filter out periodic components until a solution is found. This algorithm can be done in a superposition because there is no coupling or dependencies between any given state. Another recent quantum algorithm proposed solves a 2×2 linear system [13]. This linear algebra operation is a natural fit due to the reversible nature of spintronic-based quantum gates. Semiconductor quantum dots are another popular choice for charge-based qubits. When a quantum dot is made to be small relative to the exciton Bohr radius, the energy states for the valence and conduction bands become discrete. By confining the electron for a given spin configuration, it is possible to use an external magnetic field to flip their spin since the magnetic moment $\vec{u}$ will align with the field. A functional device has been demonstrated recently [14]. One of the large challenges for spintronics is how to entangle many qubits together so they interact. Currently, fourteen (14) qubits is the limit of what has been reported [15]. This was achieved using an ion trap configuration, which is not well-suited for practical implementations. Additionally as the number of qubits increases, it becomes more challenging to keep them entangled for enough time to perform an operation (coherence time).

PAPER

I. SCALING RELATIONS AND THE ROLE OF BOND-CHARGE TO THE ELECTRON TRANSMISSION THROUGH TWO COUPLED AHARONOV-BOHM RINGS

C. H. Wu[1], L. Tran[1], and C. A. Cain[1]

[1]*Department of Electrical & Computer Engineering*

Missouri University of Science & Technology

301 W 16th St, Rolla, Missouri 65409, USA

ABSTRACT*

Electron transport and the exact scaling relations for two irreducibly coupled Aharonov-Bohm (AB) rings with two external terminals attached are investigated. In coupled AB rings, a center common path exists where the phase of the electron wave function can be modulated by two applied fluxes simultaneously. The two coupled rings can be considered as two coupled atoms where Fermi level crossings exist not only between bonding states, but also between bonding and anti-bonding states when the applied flux is varied in one of the two cases studied. We show that when the smallest atomic-sized coupled rings are scaled up any odd number of times an identical electron transmission is preserved. When two terminals are attached to isolated coupled AB rings, there is a further redistribution of bond-charge stored

*Published in Journal of Applied Physics **111** 094304 (2012).

within the center common path. The shift of the electron charge distribution to favor one end of the common path is accompanied by the redistribution of the two partial waves that traverse through the two arms from the input to the output terminal. The flux can control which arm the electron traverses through more favorably, and hence the center path behaves like a flux-controlled charge reservoir for the electron transport. The unbalanced charge in the entire structure creates a space-charge effect much like a p-n junction. The paradox of the delocalization of the electron wave when two AB rings are coupled and the subsequent localization effect of the electron transport in a quantum network are described.

1. INTRODUCTION

In the mesoscopic and microscopic world, it can be useful to investigate strictly one-dimensional networks in order to gain physical insights. An Aharonov-Bohm (AB) ring of this size with two terminals was first investigated experimentally over two decades ago and the effect has since been studied extensively [5, 16, 17, 18, 19, 20, 21, 22]. While there are several allowed one-dimensional paths that can be embedded into a mesoscopic ring of small cross section, it has been calculated and experimentally shown that only one dominant path will persist [23, 24, 25, 26, 27, 28, 29]. The behavior of this dominant class is of key interest. There are similarities between classical waveguides and the electron waveguides presented here in a two-terminal AB ring. In a rectangular waveguide (in the microwave region) with cross-sectional dimensions a and b, there are two distinctive classes of propagation, transverse electric (TE_{mn}) and transverse (TM_{mn}) magnetic, described by zero electric and magnetic fields in the direction of wave vector $\vec{k}$, respectively. Each propagation mode (mn) within the TE or TM class is then determined by how many half-integer wavelengths can fit within the cross section. The higher divisions are the high-frequency modes while the lowest division (fundamental mode) is simply a and b. In the corresponding electron waveguide situation, this is reversed. The minimum division of an AB ring is the atomic spacing, with the lowest-order mode corresponding to an atomic-sized ring. In principle, rings of a higher-order can exist in a larger structure, such as in carbon nanotubes or graphene lattice structures [30, 31]. Mesoscopic rings will possess small cross-sectional areas consisting of several embedded one-dimensional rings. This raises an important question of the scaling relations between the lowest division AB ring and its higher-order counterparts. In a one-dimensional AB ring, the total number of atoms, M, is large but finite. Even when the value of M approaches very

large values, it is not valid to assume the $M \to \infty$ limit. This is because three distinctive classes of propagation exist, much like the TE and TM classes in microwaves. It has been shown [4] that the value of M is one of the determining parameters for this classification. In strictly one-dimensional rings with two terminals, the total number of atoms is denoted by $M = m + n$, where m is the number of atoms in the upper arm while n is the corresponding number in the lower arm. In Class I, m and n are both even numbers. Class II is when m and n are both odd, making M even. Lastly, Class III is when M is odd which constricts m and n to differ in parity. The asymmetrical result is that the upper arm and the lower arm must differ by at least one atomic spacing and hence the flux periodicity is doubled at $(\Phi_0/2)$. This is the universal double periodicity for any combination of an odd-numbered ring [4]. The important result is that this finiteness prevents one from treating the network as a continuum. Therefore a mesoscopic ring consists of 1D rings which propagate like a TE_{mn} or TM_{mn} class at a high-frequency mode or at a higher-order division of the length a or b. To demonstrate a lower-order mode, an AB ring has to be reduced in atomic size and hence there must be fewer embedded one-dimensional rings. In this case three distinctive classes of AB rings can be exhibited separately. At a low-order propagation mode, an AB ring appears as a 1D atomic-sized ring with small M, while at a higher-order mode, a collection of integrated one-dimensional rings. When M is monotonically increased the electron transport cycles through three different classes of propagation or three different transmissions and two flux periodicities, and hence uniquely distinguishes mesoscopic from macroscopic systems. Scaling relations exist which demonstrate a preservation of transmission behavior within each class if the value of M (m, n) is scaled up properly. The scaling relations for simple two-terminal rings will be briefly revisited first before we present relations for coupled AB rings.

Earlier investigations by one of us has shown [4] that the electron transmission through a two-terminal AB ring is physically equivalent to a chain of flux-assisted

harmonic oscillators of the same topology (see Fig. 2 in Ref. [1]) when subjected to an external perturbation by using a set of linear node equations described in Sec II. Therefore intuitively it is very easy to visualize that a four-atom AB ring ($M = 4$) can have equal arm lengths (two atomic spacings) between the input to the output terminals. At zero flux, the two partial waves scattered at the input will arrive at the output in phase, resulting in total transmission. However, at the flux value of $\Phi = \pm(\Phi_0/2)$, where Φ_0 is the elementary flux quanta hc/e, the two partial waves will arrive with a phase difference $|\delta| = \pi$, resulting in a total reflection. If the number of atoms were doubled ($M = 8$), phase conditions will remain the same. The harmonic oscillators are topologically equivalent in both cases (the scaling relation), hence the flux dependence of the electron transmission from zero at $\Phi = \pm(\Phi_0/2)$ to 1 at $\Phi = 0$ remains unchanged. The governing set of equations for the network are unchanged except the atomic spacing a is changed to $2a$ in all the $\cos(ka)$ terms (the $M\beta$ term in Eq. (36) of Ref. [4] is an invariant quantity). Thus an $M = 400$ AB ring with $m = n = 200$ corresponds to an arbitrary higher-order mode of Class I, whose fundamental mode is given by $M = 4$ ($m = n = 2$). The important consequence of this argument is that there is no need to investigate the electron transmission through a large structure. An equivalent small-scale toy model, corresponding to the fundamental propagation mode, is sufficient due to the manifestation of the scaling relations.

In this paper we investigate the electron transmission through two irreducibly coupled AB rings in terms of the added scaling relations (Sec. 3) and the important role played by the bond-charge storage behavior within the center common path (Sec. 4). An isolated AB ring can be considered a man-made atom with a circulating persistent current playing the role of the orbiting electron, except the positive charge is uniformly distributed in the ring. When two AB rings are irreducibly coupled by a center common path, the situation is similar to that of two coupled atoms where

bonding and anti-bonding effects are present [32]. The persistent currents are now controlled by the two external fluxes Φ_1 and Φ_2. The clockwise (counter-clockwise) persistent current is analogous to spin-up (spin-down) states so that computing networks comprised of AB rings can be described in a similar manner as spintronics [33]. Therefore correlating the charge storage behavior within the network to the electron transport is of significant interest. As we will show later, there is a charge redistribution along the center path that becomes asymmetrical when two terminals are attached as a result of the perturbation. Our investigation is motivated by the possible applications of using coupled AB rings for computing in place of two equivalent coupled spins [1].

2. NODE EQUATION APPROACH

In our work, we used the quantum network approach developed earlier [1, 4, 34, 35, 36] to calculate the one-dimensional electron transport of a given network with elastic scatterings at the node points. A quantum network is composed of nodes and bond lengths that connect adjacent nodes. Within a bond, the Schrödinger equation is satisfied. Furthermore, at each node point, the Kirchhoff law for conservation of current must also hold [37]. The resulting linear set of node equations is an exact relationship between the electron wave function at a given node with all neighboring nodes. This is physically similar to a network of coupled harmonic oscillators of the same topology with masses and springs, except the value of the spring constant is flux-modulated. The equivalence of this method compared to the traditional S-matrix approach has been established [4]. The set of node equations for a network can then be written as

$$\big[\sum_{y}\cot(kl_{xy}) - iD\big]\Psi(x) - \sum_{y}[\csc(kl_{xy})exp[i\phi l_{xy}]\Psi(y)] = 0, \tag{I.1}$$

where $k = \sqrt{2mE}/\hbar$, and E is the electron energy. The phase modulation between atoms in the ring is defined as $\phi = (2\pi/M)(\Phi/\Phi_0)$. $D = (1-R)/(1+R)$, where R is the reflection amplitude if node x is an input, $D = -1$ if node x is an output, and $D = 0$ otherwise. This set of node equations allow one to solve for all the electron wave functions at each node in the network and determine the transmission probabilities $T_{sum} = 1 - |R|^2$ if there are external terminals attached. The transmission probability is then used to calculate the conductance as described in the Landauer-Büttiker formalism [38, 39, 40, 41, 42, 43]. Note that Eq. (I.1) is not a tight-binding approximation but an exact solution.

3. SCALING RELATIONS FOR IRREDUCIBLY COUPLED AB RINGS

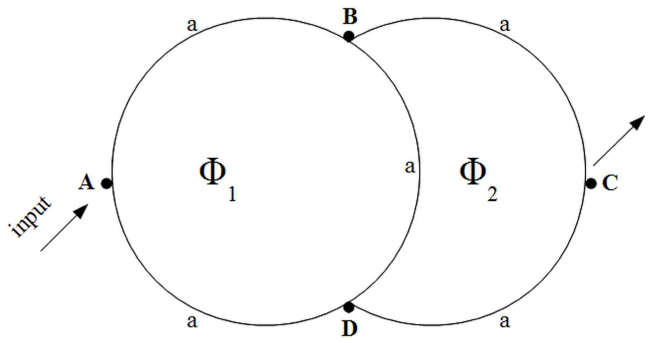

Figure 3.1: M3S AC network where two odd $M = 3$ rings are coupled together. If a second center path was connected between B and D, then the network would be considered a double bond, denoted by M3D. The areas for each ring are implied to be equal.

When two simple AB rings are merged together where they share a finite center common path [1, 30, 32, 36], they are referred to as irreducibly coupled. We examined two cases: a single bond and a double bond. In this configuration, the electron wave function along the center common path can be modulated by two fluxes Φ_1 and Φ_2. There are three primary classes of electron transmission: when the number of atoms in each ring of (I) are even, (II) odd, and (III) odd-even pairs [1]. We investigated the validity of extending the scaling relations from a simple ring to coupled AB rings. Two coupled rings can be generally described as (l, m, n), which defines the atomic spacings in the left ring, right ring, and center path respectively. Starting with the smallest M3S AC case, where $(l, m, n) = (2, 2, 1)$ and M3 stands for a total of three atoms (the smallest odd number) in each ring coupled together by a single center path with terminals at A and C as shown in Fig. 3.1, we demonstrate that the transmission is exactly preserved when the network is scaled up by any odd n-factor, with a half-period flux shift depending if the particular scaled up ring is

classified as $M = [5, 9, 13, 17, 21, ..., 4N + 1]$ or $M = [3, 7, 11, 15, 19, ..., 4N + 3]$. The results are shown in Fig. 3.2. There is a difference of a half-period flux shift between $M = 4N + 1$ and $M = 4N + 3$ of odd-numbered rings, and is not observed a single odd ring. If a second center path is added to the M3S structure, the network now has a double bond and is denoted by M3D. This additional path does not alter the flux period or possible flux shift, but does affect the transmission.

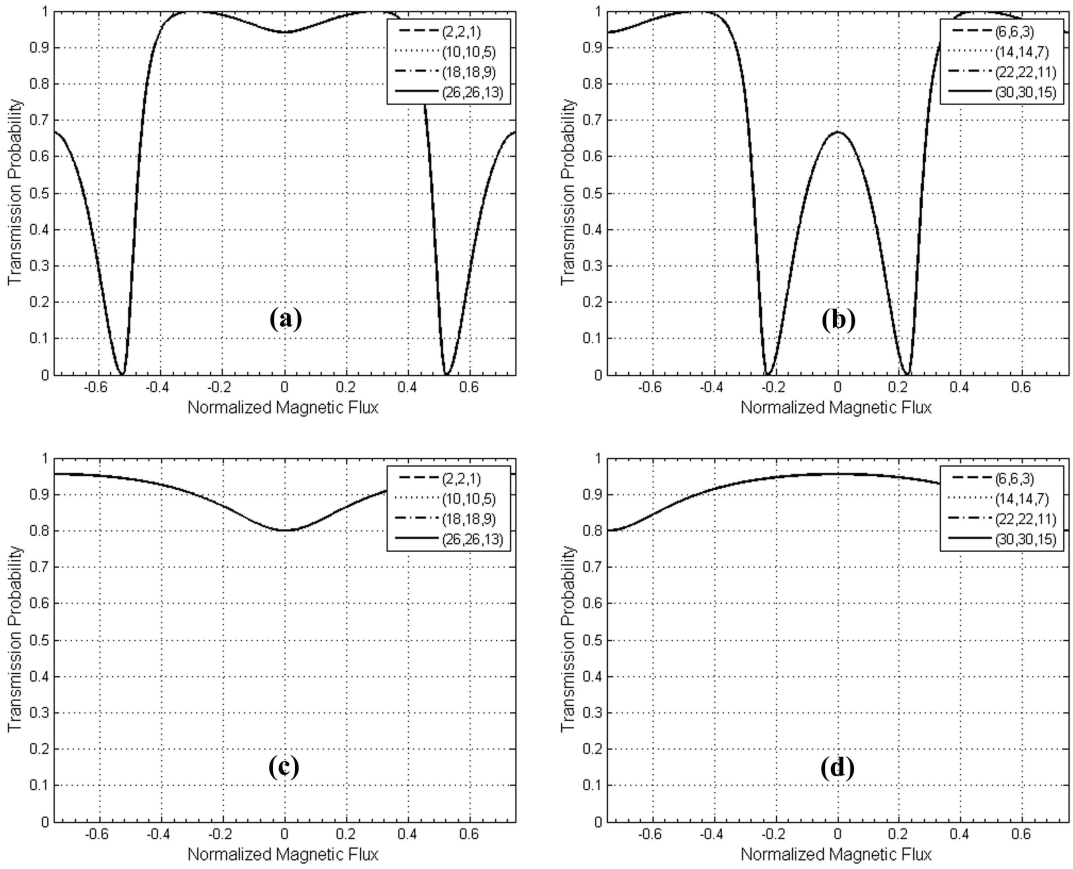

Figure 3.2: Transmission results when the smallest $(2, 2, 1)$ structure for M3S (a) and M3D (c) networks is scaled up by an odd n-factor leading to each ring having $M = [3, 7, 11, 15, 19, ..., 4N + 3]$ atoms. If the n-factor leads to $M = [5, 9, 13, 17, 21, ..., 4N + 1]$, then M3S is depicted by (b) and M3D by (d). Note the half-period flux shift of $(3/4)\Phi_0$ between the two classifications for both bonds.

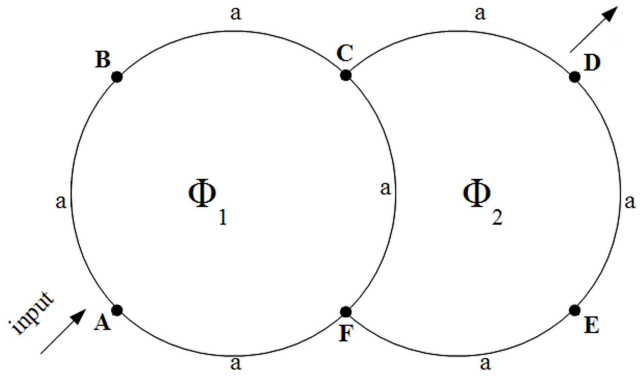

Figure 3.3: M4S AD network where two even $M = 4$ rings are coupled together. If a second center path was connected between C and F, then the network would be considered a double bond, denoted M4D. The areas of each ring are implied to be equal.

The M4S AD network is shown in Fig. 3.3, where $(l, m, n) = (3, 3, 1)$. This is the smallest even coupled ring configuration. Like the M3 structure, a double bond M4D network can be created by simply inserting another common path into an M4S. The transmission behavior is again preserved in Fig. 3.4 when scaling by any odd n-factor of M4. While the M3 cases exhibit a half-period flux shift, such a difference disappears in even networks since the total atoms always remain within the same $M = [4, 8, 12, 16, 20, ..., 4N]$ group, never crossing into $M = [6, 10, 14, 18, 22, ..., 4N + 2]$. The same would hold true if one were scaling a coupled network initially falling into the $4N + 2$ group.

Combining these results with previous works, it can be sufficiently stated that a fixed quantum network can be scaled any odd number of times and exhibit identical transmission behavior, i.e., changing the atomic spacings in the network from $(3, 3, 1)$ to $(9, 9, 3)$ and so on has no effect on the transmission. These observations are very important because together they state that an atomic-scale network can be scaled-up to a mesoscopic size as long as the electron coherence is maintained.

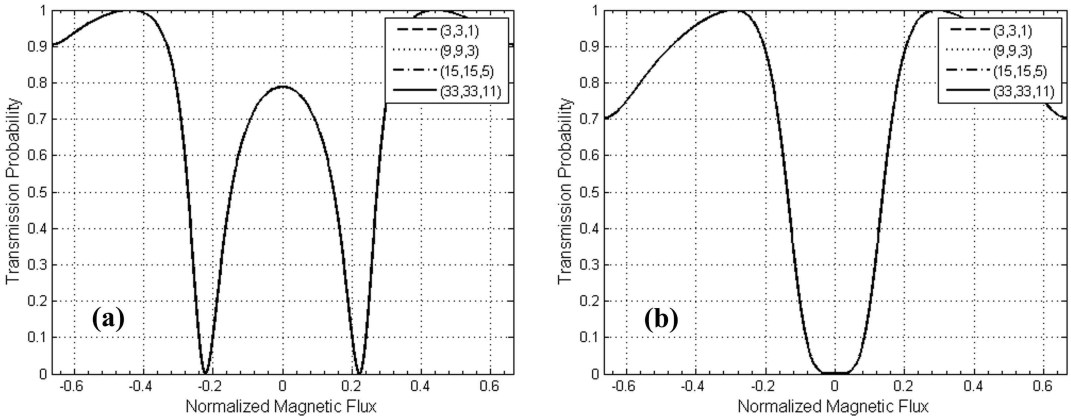

Figure 3.4: Transmission results for M4S AD (a) and M4D AD (b) networks. The transmission remains exact for any odd n-factor, without a flux shift since all odd scaling configurations fall into the same 4N group.

Since there are only three classes of coupled rings, the scaling relations imply that any fabricated mesoscopic structure of small cross section will exhibit the dominant electron transmission mode present in one of the three classes.

4. CHARGE DISTRIBUTION AND ITS RELATION TO THE ELECTRON TRANSMISSION IN TWO COUPLED AB RINGS

In an isolated situation of two even coupled AB rings, the total amount of electron charge accumulated along the center common path can be varied by the applied fluxes Φ_1 and Φ_2 to reach a peak value or total depletion. In our study, we examine when fluxes $\Phi_1 = \Phi_2 = \Phi$ only. As the electron charge starts to be depleted with an increasing value of the applied flux Φ, the electron density is redistributed so that the outer loop of the weakened bonding orbital get more share of the electron density as one expects. The corresponding electron density profiles are plotted in Figs. 4.1(a) and 5(b) for the entire flux period. The electron charge is integrated over the entire center path and then evaluated as a fraction of the total charge in the normalized unit of a single electron e, shown in Fig. 4.1(c). In the double bond situation, the electron charge is depleted monotonically as the flux increases due to the Fermi level residing at a bonding orbital over the entire flux period (Fig. 4.2(a)). The average charge at the center path over the entire flux period is calculated to be $0.2355e$ of the total charge in the entire structure, which is less than the value of $0.25e$ in the uniform charge distribution for two bonds out of the 8 total. However, for the single bond situation, the Fermi level of the coupled rings starts at an anti-bonding orbital, rather than a bonding orbital, with a small electron density along the center path at zero flux. There is then a Fermi level crossover to a lower energy bonding orbital at $\Phi = \pm(2/9)\Phi_0$ as the applied flux is increased where there is a sudden inrush of charge into the common path, as shown in Figs. 4.1 and 4.2(b). The average electron charge for the single bond case is $0.1112e$ of the total charge. Again this value is less than one expects ($0.143e$) from a uniform charge distribution for one bond out of 7 total. The Fermi level crossing uniquely defines where uniform charge distribution takes place between all bonds in the network. The discontinuity in our calculations can be attributed to the charge instantly being depleted from

a higher energy anti-bonding orbital to fill the lower bonding orbital at this Fermi level crossing. Note that right at the crossing, electron density will be adjusted to a uniform distribution first before any further changes. At flux values less than the crossing, there is no net current flowing through the center path since there is no electron density at the midpoint. Once the Fermi level crosses into the bonding orbital, the net current remains zero since the directional derivative of the electron density vanishes. From observing both the single and double bond situations, it is obvious that whenever two AB rings are coupled there is an equilibrium redistribution of electron charge from the center common path to the outer bonds, which can result in a fractional electron charge circulating around the larger outer loop. This space-charge effect is no different from bringing an n-type and a p-type semiconductor together to form a classical diode at equilibrium, except now the space-charge is from two metallic rings. This origin is of course from the delocalization tendency when two rings (two atoms) are coupled and the degree of which depends whether the Fermi level resides at a bonding or anti-bonding orbital.

There is an opposite effect in odd coupled AB rings. That is, as flux is increased there is now a monotonic increase in charge accumulation along the common path. As in the transmission perspective, this fundamental difference in charge accumulation behavior between even and odd networks is very interesting. The M3S (single bond) network possesses a Fermi level crossing at $\Phi \approx \pm 0.522\Phi_0$ where a stronger bonding orbital is then encountered out to the zone boundary, as depicted in Fig. 4.3(b). The existence of this Fermi crossover can be further explained by the sudden burst of charge at the center common path, leading to the average charge of the single-bond to possess $0.1296e$, dominating the double bond network (lacking such a crossing) which only has an average of $0.0407e$. These results are shown in Fig. 4.4. At the Fermi level crossing for the M3S case, there is again a uniform charge distribution among all of the bonds in the network, even though this crossing

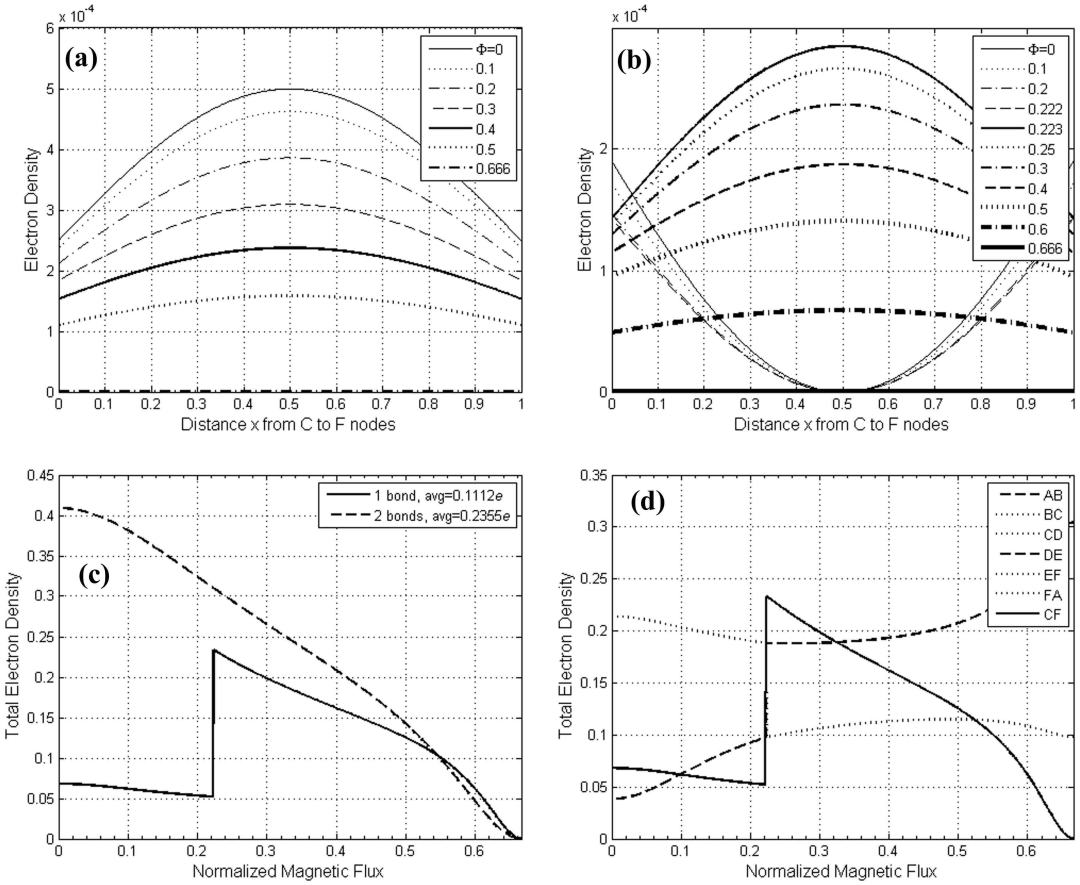

Figure 4.1: Isolated M4D (a) and isolated M4S (b) common path densities. (c) Total density along common path. (d) Total density for all bonds in M4S network. At the Fermi level crossing, there is uniform distribution and is the cause of the discontinuity.

is between two like (bonding) orbitals, unlike the M4S case discussed previously. The discontinuity in this region is again a signature of the Fermi level crossing.

We further examined the situation when two externals terminals are attached to even coupled rings and study the relation between the electron transport and the behavior of the electron density at the center common path. In Fig. 4.5, we show the corresponding electron density of Fig. 4.1 when two terminals are attached at nodes A and D. There is now an asymmetry between the upper and lower branches of the ring. The two electron partial waves scattered at the input terminal A are unequal in

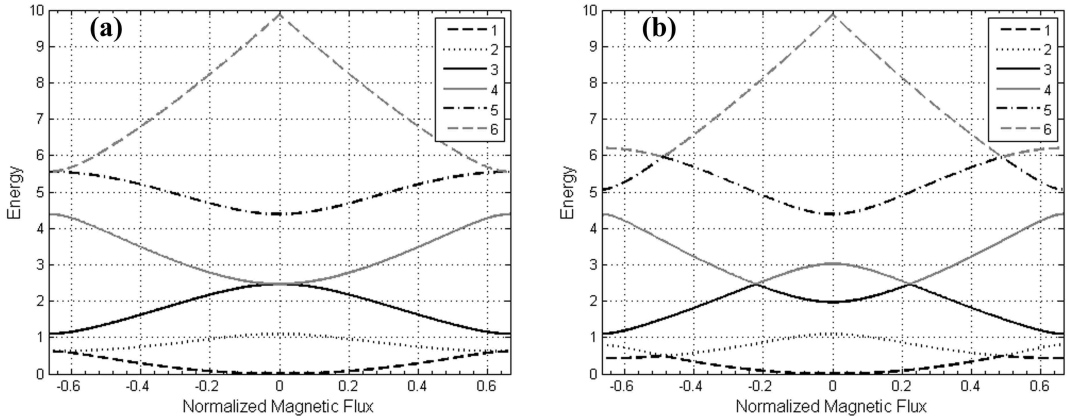

Figure 4.2: M4D (a) and M4S (b) band structures, also shown as part of Fig. 4 in Ref. [1]. The Fermi level for the M4S network encounters a crossover between an anti-bonding to bonding orbital, not present for M4D. Reprinted with permission from J. Appl. Phys. **110** 054315 (2011). Copyright 2011 American Institute of Physics.

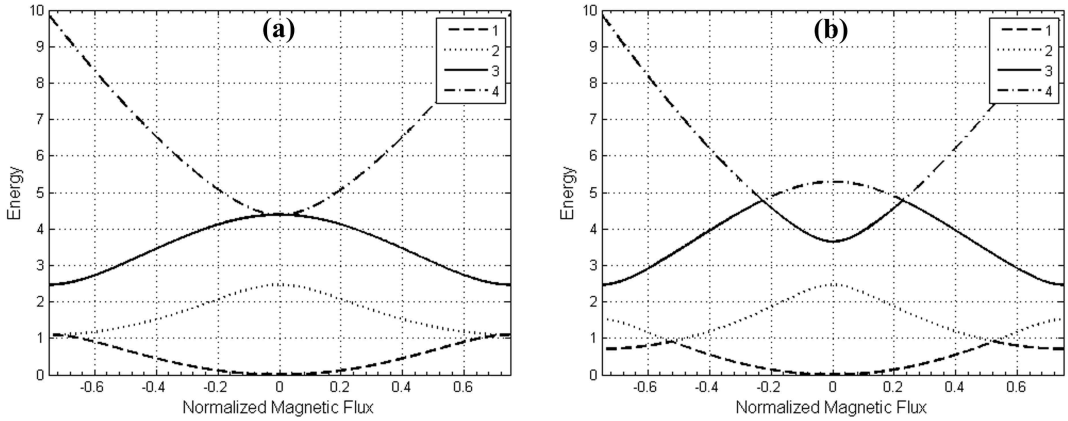

Figure 4.3: M3D (a) and M3S (b) band structures. Note that the Fermi level for the M3S network encounters a crossover to a stronger bonding orbital, which is not present for M3D.

amount and now favor passing more through node C and less through node F to arrive at the output D. This bond charge redistribution within the common path is closely related to the electron transmission through the terminals. It implies that when two external terminals are attached the electron charge stored within the segment of the

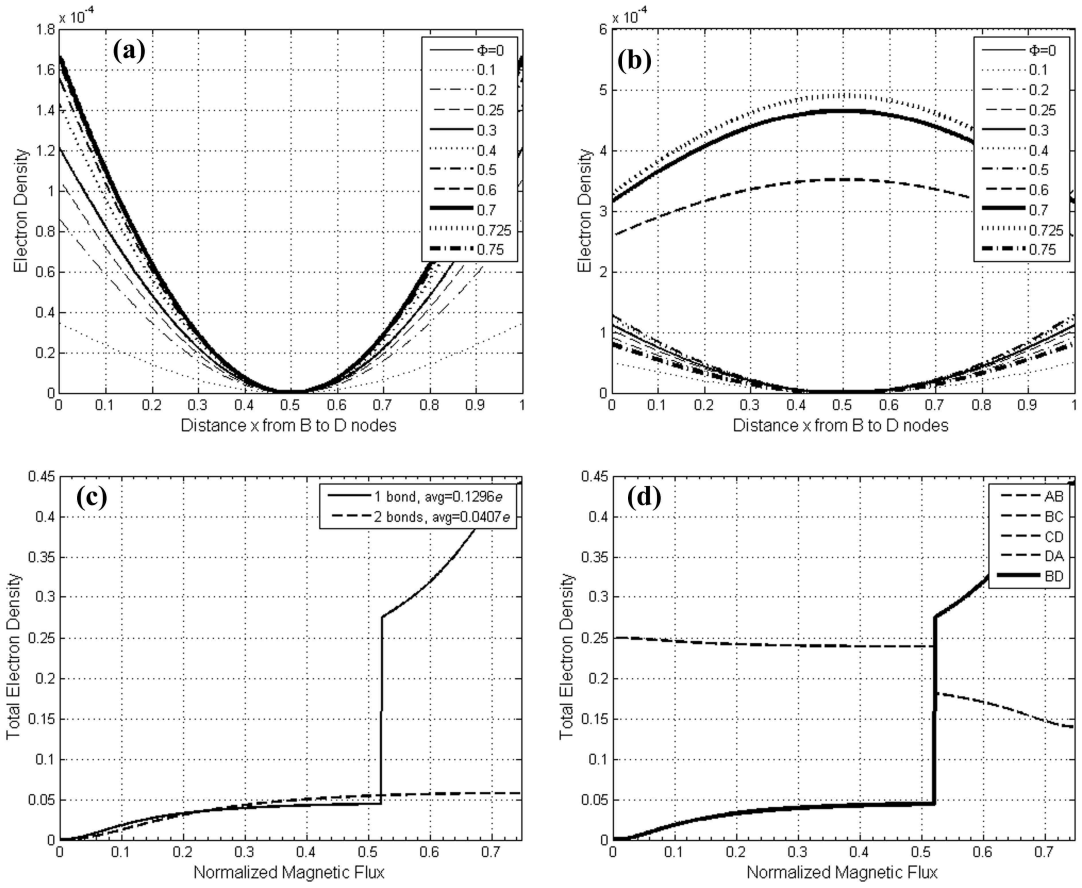

Figure 4.4: Isolated M3D (a) and isolated M3S (b) common path densities. (c) Total density along common path. (d) Total density for all bonds in M3S network. A uniform distribution exists at the Fermi crossing, leading to the discontinuity.

center path not only redistributes with the outer loop bonds, but also redistributes within the path itself by shifting more of its share of the charge to one end (at node C) to accommodate the mode of the electron transport. There is always a tiny amount of residual charge remaining in the path for both double and single bond situations at the flux value of $\Phi = (2/3)\Phi_0$. Thus whenever two external terminals are attached, the charge at the center common path cannot be totally emptied as in the case of isolated coupled rings if transmission is said to be possible. However the total integrated charge along the common path is very similar to the situation of the

two isolated coupled rings, even though at the zone boundary ($|\Phi| = (2/3)\Phi_0$) the total charge is not exactly zero, as shown in Fig. 4.5(c). As a result of charge density redistributing to the outer bonds along with the remaining charge shifting to one end of the center common path, the incoming electron will favor passing through one of the two arms (ACD) by adjusting the amount of the two partial waves in each arm accordingly. This is in sharp contrast with the situation of having two equal partial waves in a simple even AB ring of two equal paths with no center common path. Thus which path the electron can traverse through a network of two coupled AB rings is determined by the class said network belongs to. Those classes are determined by the parameters of (l, m, n) as discussed earlier in Sec. 3. We note there is a similarity between the electron transport when the Fermi energy is at a bonding orbital at the range of $(2/9)\Phi_0 < |\Phi| < (2/3)\Phi_0$ for a single bond and $0 < |\Phi| < (2/3)\Phi_0$ for the double bond situation, both depicted previously in Fig. 3.4. For the anti-bonding orbital at $0 < |\Phi| < (2/9)\Phi_0$ in the single bond case, there is a drop in the electron density along the common path, thus an electron traverses through the coupled ring in that flux range as if the two nodes at the ends of the center common path are weak scattering centers and the transmission probability peak is reduced to 0.8 from 1 for a simple AB ring. When two terminals are attached, the charge density discontinuities at the Fermi crossing previously observed in the isolated network (Fig. 4.1) are removed by the perturbation and a more subtle change is observed due to the mode of transport now controlling how the charge is allocated within the bonds.

When two odd coupled rings have terminals attached at A and C, forming equal upper and lower arm lengths, a similar general trend of charge shifting to the upper end (at node B) of the common path is present, as shown in Fig. 4.6. The single bond structure however exhibits this behavior up to the Fermi level crossing to the lower (and hence stronger) bonding orbital, but the charge then shifts more to the lower end (at node D) of the common path past this point to the zone boundary.

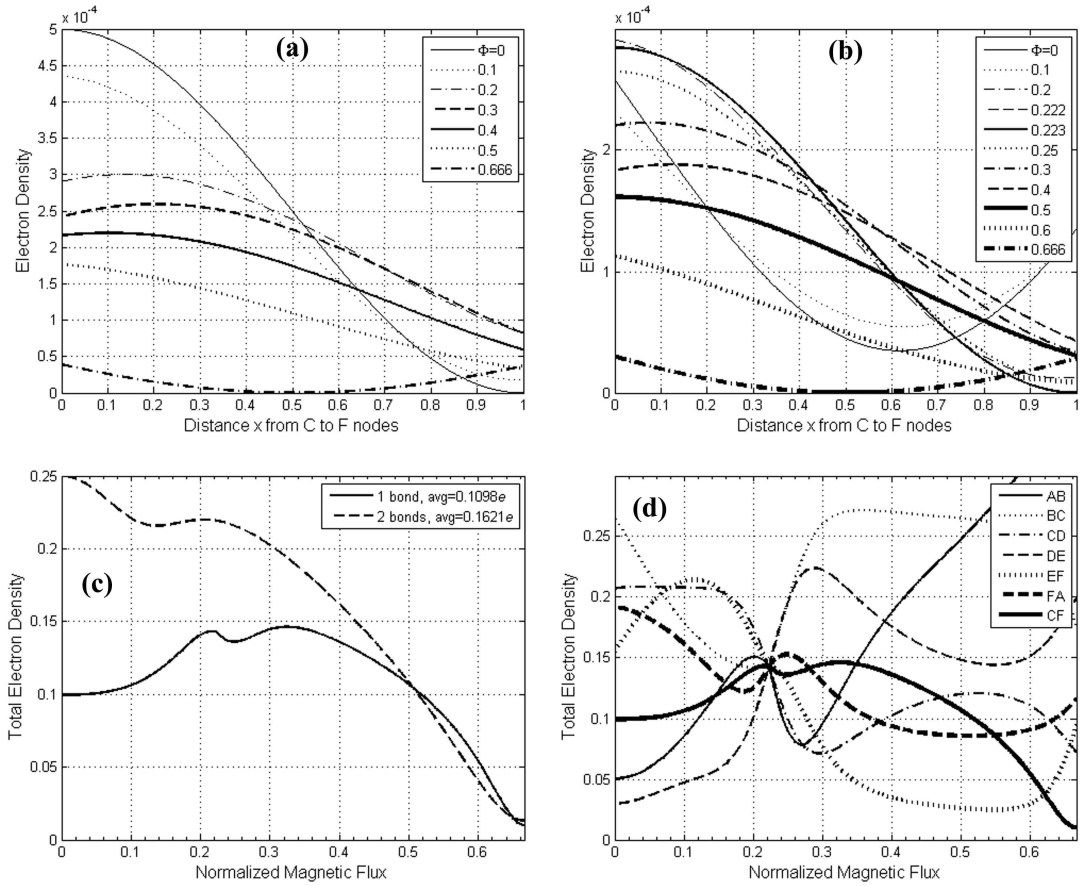

Figure 4.5: M4D AD (a) and M4S AD (b) common path densities. (c) Total density along common path. (d) Total density for all bonds in M4S AD network. Note that while there are no electron density discontinuities at the Fermi crossing flux, the uniform density distribution is achieved at the crossing nonetheless.

Since the terminal locations form a symmetric outer loop, there is a corresponding symmetrical charge distribution at the center common path for zero flux and at the zone boundary $|\Phi| = (3/4)\Phi_0$, which can be attributed to singularities in transmission at these values. Unlike the isolated odd coupled rings, there is now a clear difference of additional total charge accumulation in the common path for a double bond, compared to a single bond. Even though in the isolated situation the single bond contained a Fermi level crossing to a stronger (lower) bonding orbital, the

sudden burst of charge (at the discontinuity) for uniform distribution once present is now mitigated by the network having to accommodate the mode of transport for symmetric terminals. Thus the double bond takes a greater share of the charge, with an average of about $0.3e$, compared to the single bond taking only about $0.2e$. Note how both are very close to uniform charge distributions of 1/3, and 1/5, respectively. The physical significance of this observation is the mode of transport for symmetric terminals forces the charge to redistribute equivalently across the entire flux period, consistent with what one might predict. There is not a uniform charge distribution at the Fermi crossing for M3S AC, unlike its corresponding isolated network and the M4S AD case described earlier (Fig. 4.5(d)). This is due to its Fermi crossing being between orbitals of the same type (weaker to stronger bonding orbital). In other words, for a uniform charge distribution to exist at some finite flux value within the flux period for a two-terminal network, there must be a Fermi level crossing between bonding and anti-bonding orbitals, regardless of terminal arrangement. Additionally, we can deduce that symmetric terminal arrangements do not in general indicate a symmetrical charge distribution at the center common path, but instead lead to an average uniform charge distribution between all bonds within a single flux period.

The significance of a Fermi level crossing is bolstered by another observable phenomenon related to the transmission within a given network. By examining the transmission of structures containing Fermi crossings (M3S, M4S), shown in Figs. 3.2 and 3.4, respectively, it is clear the transmission probability being driven to zero (excluding zero flux and the zone boundary) is simply the manifestation of a crossing itself. Thus the reflected waves magnitude is always unity in this region. This strong pull-down of the transmission to zero is similar to having a simple two-terminal AB ring with a narrowed flux period whose zone boundary is now at the Fermi level crossing. By being able to identify Fermi level crossings by observing the transmission in coupled AB ring networks, one can additionally determine when the

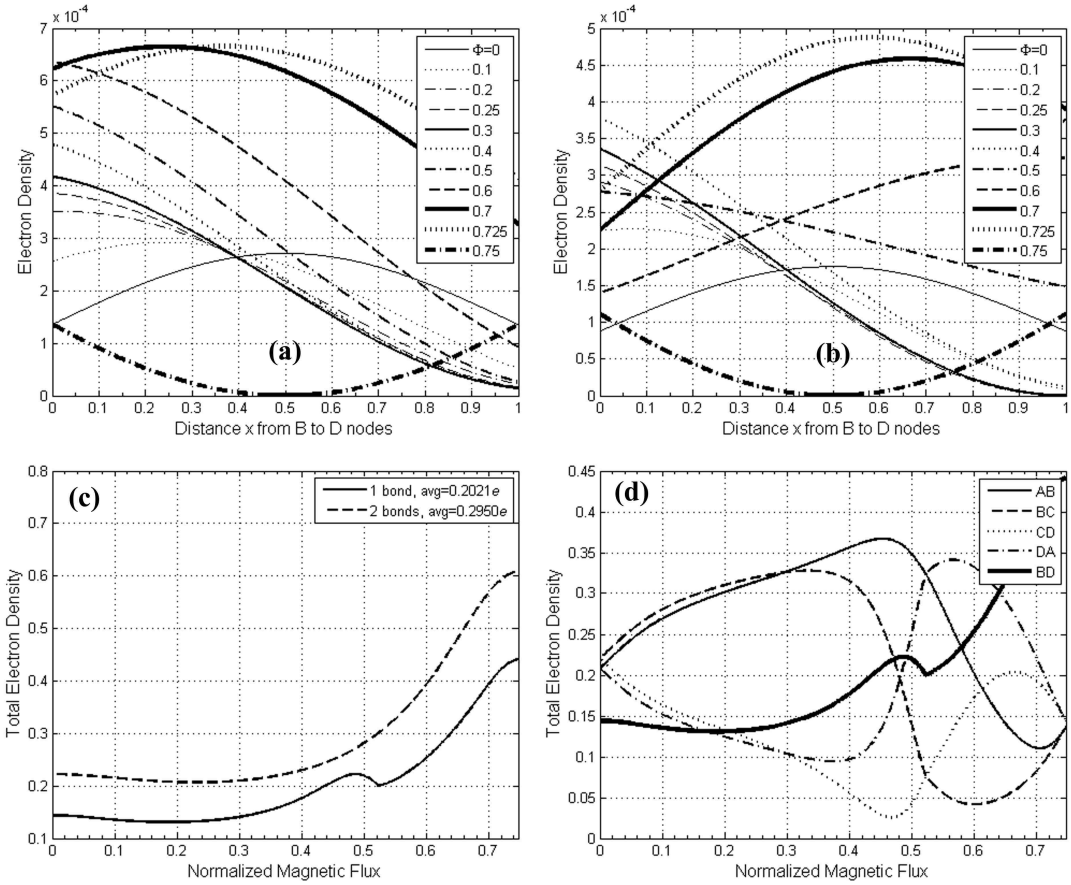

Figure 4.6: M3D AC (a) and M3S AC (b) common path densities. (c) Total density at the common path. (d) Total density for all bonds in M3S AC network. Note that at the Fermi crossing the uniform distribution that once existed in the isolated network is no longer present.

center common path has a large portion of the total charge stored within it in the case of bonding to bonding orbital crossings, or when there is likely to be a uniform charge distribution throughout all bonds in the network for bonding to anti-bonding orbital crossings.

5. CONCLUSIONS

We examine the coupled AB rings from a purely one-dimensional point of view. In any quantum network for guided electron partial waves, there cannot be an infinite number of atoms in the network. Instead, there exist several different classes of the smallest building blocks. When each of these smallest structures is magnified properly, an identical transmission behavior will be preserved for each class. This is in a reverse trend with respect to classical microwave waveguides as far as the division of length is concerned. The finiteness for the value of M, the total number of atoms in the one-dimensional network, is the same requirement as that on the finiteness of length in microwave waveguides. While small atomic-sized AB rings can exist in pure one-dimensional form, larger 1D rings can be embedded in a mesoscopic ring of small cross section and are thus experimentally observable. For two coupled AB rings, we showed that scaling relations exist which connect the smallest rings to larger sized rings with an identical electron transmission if the size is scaled-up any odd number of times, within the coherence length limit. The classification is determined by the parameters (l, m, n), where $l = m$ for two identical rings and $M = l + n$ is the total number of atoms. Since M is one of the classification parameters, mesoscopic rings cannot be treated as a continuum. The scaling relations presented suggest one only needs to investigate the electron transport based on the smallest atomic-sized structures.

When the two coupled AB rings are attached with two terminals, the bond-charge stored at the center common path is further redistributed as compared to the situation of two isolated coupled rings. In general, at zero applied flux charge flows to the outer loop to strengthen the anti-bonding orbital, or weaken the bonding orbital, depending on where the Fermi level is residing at. Therefore the space-charge capacitance of the coupled rings is also continuously varied with respect to the

applied flux. When the two terminals are attached, there is now an asymmetry of the charge storage in the common path that is correlated with the asymmetry of the two partial waves passing through the two arms between the input and output terminals. This asymmetry is flux-controllable, therefore the electron transport can be tuned between the two arms for a given network. The net current passing through the common path is always zero. The presence or depletion of charge in the common path, paired with the ability to modulate between both states, has potential applications in nanoelectronics such as a quantum capacitor or memory storage element. We have shown that there exist a few fundamental modes from the coupled electron waveguides based on the 1D structures. Therefore, experimentally, we expect a dominant mode can be observed from mesoscopic-sized coupled AB rings similar to the verification of a simple two-terminal AB ring in Ref. [5].

Finally there is a paradox of electron transport through a quantum network. When two AB rings are coupled, the electron wave function is spread out over a larger region. However this delocalization of the electron wave is at the expense of an increase of two more scattering centers created at the two ends of the common path. Thus the incoming electron from the input terminal will suffer more scattering events compared to when the center common path is removed. The electron wave is then decomposed into more partial waves every time a scattering event occurs. More scattering centers lead to more backscattering and hence to the Anderson localization for the electron transport [44]. Therefore at zero applied flux, the forward transmission will suffer generally as compared to the situation when the center common path is absent. The applied fluxes can reverse the localization trend (as in M4S and M4D cases where the bond-charge decreases) or increase the localization (as in M3S and M3D where the bond-charge increases) by being able to tune the two partial waves at the output terminal to be in or out of phase. We have shown even and odd coupled rings store the bond-charge in an opposite trend with respect to the increase of the

applied flux. Thus the ideal indicator is to observe the bond-charge at the center common path. If the common path has more than a uniform share of bond-charge, the electron wave is more localized than before and by the paradox theory stated earlier, the electron transport to the output terminal will improve. On the other hand, if the bond-charge is reduced to less than a uniform share, the electron wave is more delocalized than before and hence the Anderson localization effect prevails and the favorable forward transmission will be reduced to a smaller flux range.

II. QUANTUM NETWORK THEORY OF COMPUTING WITH RESPECT TO ENTANGLED FLUX QUBITS AND EXTERNAL PERTURBATION

C. A. Cain[1] and C. H. Wu[1]

[1]*Department of Electrical & Computer Engineering*

Missouri University of Science & Technology

301 W 16th St, Rolla, Missouri 65409, USA

ABSTRACT*

In this work, we attempt to show the differences between traditional qubit-based spintronic methodology for quantum computation and the possible ballistic quantum network implementations. Flux qubits can be considered topologically similar to the persistent currents possessed as the angular momentum in Aharonov-Bohm loops, which can be coupled and thus entangled together. Since entanglement is guaranteed for coupled quantum networks, starting from a point-contacted situation, we first investigate how varying the degree of entanglement strength can affect the superposition of the four possible states for two isolated flux qubits being brought together. In general the superposition is destroyed once the degree of entanglement is altered from the point-contact situation. However we show that for a specific network with maximum entanglement, a Bell state situation can be produced. We then examine

*Published in Journal of Applied Physics **113** 154309 (2013).

the effects of varying the external perturbation strength on the readout capability in quantum networks by changing the coupling strength through the cross-sectional area ratio. From the analysis of our results, we are persuaded to believe that two universally accepted components for quantum computing are not valid in the quantum network approach: the need of a weak perturbation for measurement of computational results, and the requirement of fixed entanglement among qubits. We show there is an interplay between the strength of the entanglement and that of the external perturbation for high-fidelity classical readouts.

1. INTRODUCTION

Quantum computing has been investigated extensively by many researchers founded on the qubit-based concept [9, 10, 14, 45, 46, 47, 48, 49, 50, 51, 52, 53, 54, 55, 56]. In the standard qubit formalism for a particle such as an electron, the state of the qubit can be written as the linear combination of the eigenstates of the Pauli spin matrix along the rotational (typically z) axis,

$$S_z = \frac{\hbar}{2}\begin{bmatrix} 1 & 0 \\ 0 & -1 \end{bmatrix} \tag{II.1}$$

with normalized eigenstates $\{(1,0),(0,1)\}$. In quantum network theory [4, 57, 58, 59, 60, 61] it is possible to extend the notion of a flux qubit to Aharonov-Bohm (AB) rings based on the angular momentum concept. The typical spin-up/spin-down eigenstates can be considered as the clockwise (CW)/counter-clockwise (CCW) circulating persistent currents flowing in an AB loop network, as shown in Fig. 1.1. Hence for a single isolated AB ring the CW or CCW angular momentum superposition exists periodically with a period of hc/e or Φ_0. For example in Fig. 1.1 at $\Phi = \pm 0.5\Phi_0$ or 0, the persistent current will discontinuously switch between the global maximum and minimum. This always occurs at the Brillouin zone boundary or a Fermi level crossing between bonding and anti-bonding states. Therefore the AB ring is similar to an atom whose angular momentum vector exhibits the switching of the eigenstates because the current oscillation is equivalent to a chain of coupled harmonic oscillator waves.

For a single qubit, the flux model for an AB ring seems to fit the traditional quantum computing concept. When two such isolated AB rings are entangled with each other by sharing a center common path, there are now two possible fluxes which can penetrate each loop, denoted by ϕ_1 and ϕ_2, with the flux periodicity deviating

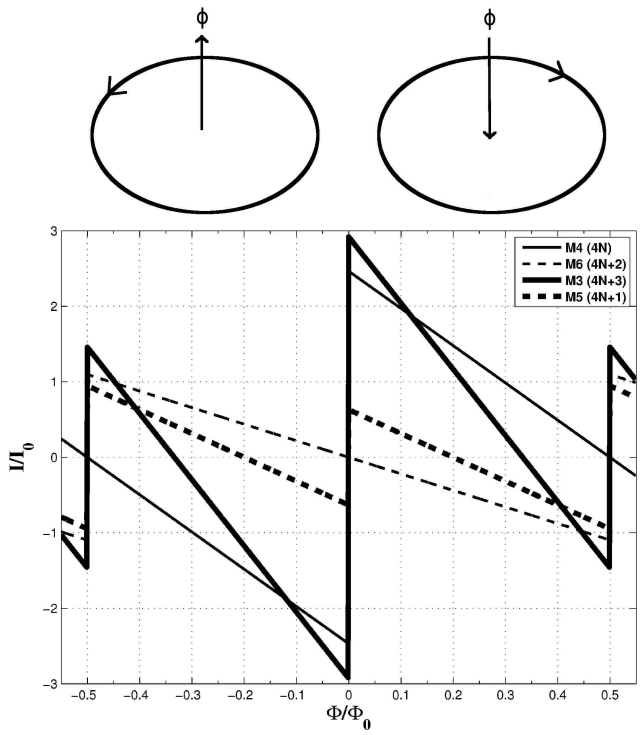

Figure 1.1: Single isolated AB ring whose angular momentum state is in a superposition. At zero flux there is an overlap at E_f between bonding and anti-bonding states which causes this, with the other case being the zone boundary. There are four possible groups, $M = 4N$, $4N + 2$, $4N + 1$, and $4N + 3$, where M is the number of scattering sites and N an integer. For the even and odd curves shown, we use the lowest M for each group. $I_0 = (\hbar^2 M)/(2m_e\Phi_0)$. The two odd groups are in superposition at zero flux and the zone boundary, while the even groups only have a single flux value for superposition. There is a half period flux shift between the superposition for the even $4N$ (zero flux) and $4N + 2$ (zone boundary), as well as the odd $4N + 1$ and $4N + 3$ (min/max switched) groups. We have described these relations in the past [4, 62].

from the elementary flux quanta accordingly [1]. There is now an interaction along this channel between the two partial waves embedded in each ring, and hence the Brillouin zone is two-dimensional. For quantum computing purposes, any ring-to-ring entanglement is supposed to provide the four possible spin pairings for parallel computation, which corresponds to the parallel execution of boolean algebra addition

for two values, typically called a half-adder. The two point-contacted AB rings (Fig. 2.1(a)) can fit into this picture with the superposition condition unaltered. However the ring-to-ring interaction, which can be arbitrarily and lithographically imposed (Fig. 2.1(b)), may or may not leave the superposition condition intact even if we allow the shift of applied flux at the superposition region. Secondly, the readout of the computation from the qubit concept requires that the external perturbation be very weak and brief as not to alter the state of the system's four spin pairing condition. In this paper, we show those two conditions are not valid from the quantum network theory. We describe in Sec. 2 how varying the entanglement strengths may change the existence of superposition for the four pairings. In essence, it depends on the ring-to-ring interaction (internal coupling) that is physically imposed on the system. Even if the entanglement between two AB rings manages to preserve the superposition at an altered flux period, any form of external readout measurement (external coupling), which is supposed to collapse the wavefunction of the network to provide a classical result, does not need to be weak or brief. In fact strong and permanent external perturbation to the isolated and entangled AB rings is desirable for a robust readout, provided that the strength of the entanglement is stronger in cooperation with the external perturbation.

The half-adder computing capability from two coupled AB rings is clear. The four angular momentum pairings can be mapped into the four rules for addition of two binary values: 00, 01, 10, and 11. Here the 00 pair indicates the angular momenta of the two AB rings are both CW, and so on. This mapping can be arbitrarily assigned and evaluated with flux values of the same magnitude. Such a circuit has been shown recently by us [1]. The classical readout requires a test signal (an input) to sample through the two coupled AB rings and the results (the outputs), namely "sum" and "carry,"need to be correctly separated. That requires two terminals alone. Furthermore, an additional third terminal is needed when the 00 operation case arises,

since the Boolean rules require the test signal not to reach the "sum" or "carry" terminals. Hence it must appear on the extra third terminal. Thus a half-adder is composed of a simple structure of two coupled AB rings with three attached external terminals for readouts, which is further characterized in Sec. 3.1. Such a half-adder replaces between one and two dozen MOSFET transistors (depending on static or dynamic implementation) used in current classical circuits. More broadly in Sec. 3, we examine how weak and strong external perturbations affect the readout from a quantum computing scheme that is implemented.

The demonstration of electron transmission through an AB ring with two strongly coupled terminals was shown in the mid-1980's [5]. This is the simplest form of a quantum network connected to two chemical potential reservoirs. Even in this form, there are three classes of electron transmission, depending on the locations of the two terminals and the total number of atoms (sites) in the ring. Each class is like a fundamental mode of a microwave waveguide. There is further a scaling relation where a properly scaled up version of the ring will exhibit an identical transmission to its smallest possible atomic sized ring [4]. Generalization of such quantum networks to three and four terminals have been investigated for possible wave-computing using the vector sum of two coherent inputs [34, 35].

Recently we tried to relate the qubit-concept based computing through a quantum network-based framework. We showed that with three such strongly perturbed external leads, a high-fidelity classical sequential readout is possible. In this paper we will further show how (I): weak and strong entanglements along with (II): how weak and strong external perturbations will affect the result for a classical readout separately. Our investigation of these quantum networks is based on an exact and non-tight-binding global node equation method formulated previously by one of these

authors, and can be reviewed in the literature [4]. Finally, we summarize the differences between mainstream qubit-based computing and the approach for quantum networks in Sec. 4.

2. ANGULAR MOMENTUM ENTANGLEMENT IN QUANTUM NETWORKS

If two AB rings are entangled together in a very weak manner, such as by quantum point contact, then each loop can be treated as their own Hilbert spaces. This leads to four possible system states $|A_{loop}\rangle \otimes |B_{loop}\rangle$, and is illustrated in Fig. 2.1(a) where the persistent current of the pair behaves similarly to that of a single AB ring shown in Fig. 1.1, with superpositions exhibited at $\Phi = 0$, $\pm 0.5\Phi_0$, $\pm\Phi_0$, and so on. Therefore with a point contact entanglement, the qubit model is still valid for any combination of input fluxes.

Generally when two AB rings are touching one another, there is an entanglement, or overlapping of the partial wavefunctions of the two rings. When two AB rings are point-contacted (Fig. 2.1(a)), this is a minimum entanglement where a superposition of the four states exists because the energy spectrum remains the same as that of a single AB ring. As two rings become closer, the overlapping is increased and there is a common path (one or two channels) such that the phase of the wavefunction can be modulated by two independent fluxes (Fig. 2.1(b)). This increases the degree of entanglement, and is reflected by the lowering of the Fermi level, E_f, with the overlap of bonding states being pulled up, and the anti-bonding states being pulled down, respectively, in energy space at one flux period. In isolated coupled AB networks that only share a middle common path (or two), the entanglement is much stronger with a broadened flux periodicity (dependent upon the geometry of the network), as given by Eqs. 6-7 in Ref. [1]. The entanglement is considered at its strongest when there is only a single common path, shown in the upper-left of Fig. 2.1(b). When the entanglement becomes this strong, the bonding and anti-bonding states can be at equal energy for certain flux values within the first Brillouin zone and when the applied fluxes to the loops are equal in magnitude [62]. At these Fermi level crossing points between states, there is an inherent uncertainty in the direction of the

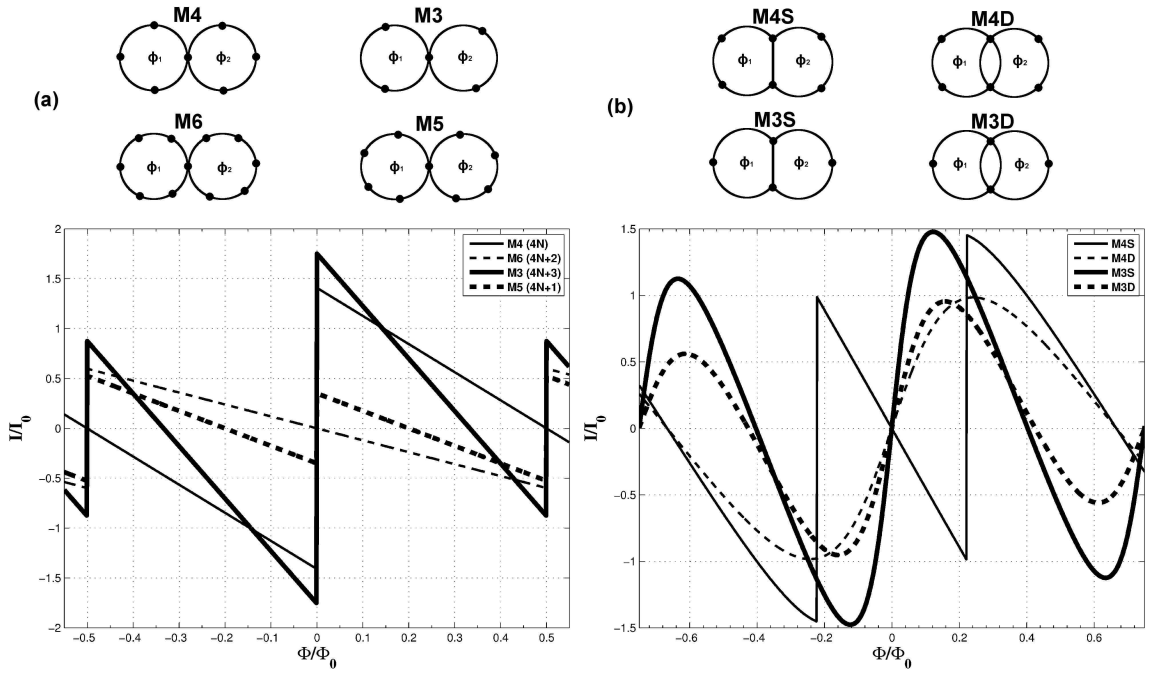

Figure 2.1: Change of superposition capability as the strength of entanglement increases. (a) Weak entanglement of the four possible groups for even and odd AB rings, coupled by a single scattering site (point contact rings). The superposition is preserved due to the band structure being unaltered from the single ring. (b) Strong entanglement for the two smallest even/odd groups ($4N$, $4N+3$), either with a single center common path (S) or a double (D). Generally the superposition is destroyed, but single bonds which represent the strongest entanglement in quantum networks can overlap the band states at E_f to a degree that also produces a superposition (as in M4S). The applied fluxes are given as $\Phi = \phi_1 = \phi_2$. Note that the other two groups ($4N+2$, $4N+1$) need not be investigated due to scaling laws we have noted earlier. Thus they will behave qualitatively similar to that of their respective sister group, though with a possible flux shift.

persistent current flowing in the network (hence in a superposition), at $|\Phi| = \frac{2}{9}\Phi_0$. Superposition is also observed for single AB loops with no applied flux, which was outlined in Sec. 1 (Fig. 1.1). It is important to note that for entanglements stronger than a point contact situation, this Fermi level crossover behavior is only observed in even-numbered rings (either groups $M = 4N$ or $4N+2$ due to scaling laws) that

are coupled by a single path (the strongest form). Since the charge density within the common path is either zero at its midpoint, or its divergence is [62], the portions of the persistent current in both rings must be flowing in the same direction of the angular momentum. Physically, if one were to measure the current for one loop, there would be no guarantee of a given direction. However, whatever the outcome for the first loop, the second loop's measurement is guaranteed to be identical with the first. This is true even for Fermi level crossings and at the zone boundary. Therefore the state of the system can be described by two Bell states,

$$|\Psi\rangle = \alpha \left|\psi^{+}\right\rangle + \beta \left|\psi^{-}\right\rangle \tag{II.2}$$

where $|\psi^{+}\rangle = \frac{1}{\sqrt{2}}(|00\rangle + |11\rangle)$ and $|\psi^{-}\rangle = \frac{1}{\sqrt{2}}(|00\rangle - |11\rangle)$. It is clear that as the degree of entanglement between the coupled rings increases past the point contact stage, there is no guarantee anymore of preserving all four possible states. We show that the ring-to-ring interaction destroys the superposition for the weaker double bond couplings, while moving to maximum entanglement (singe bond) will intuitively produce a Bell situation, though only for networks that fall into an even-numbered classification group. This provides a contrast with qubit-based quantum computing, where superposition is assumed during entanglement. Quantum computing at a minimum must be able to perform the algebraic operations first.

3. EXTERNAL COUPLING STRENGTH CONSIDERATION

In qubit-based quantum computing, the typical approach is to attempt to determine the state of the system without disturbing the internal state or superposition, meaning a closed system basically. In other words, for a readout a weak or indirect measurement is necessary. In the quantum network approach, external perturbations for readouts are typically permanently attached and strong. In this section we describe how varying the external coupling strengths for both weak and strong entangled quantum rings can affect the readout of the computations. We denote the external perturbation strength with the coupling parameter Δ, which is the cross-sectional area ratio of the terminal probe to the electron waveguides of the ring itself. In the global node equation approach we have used in our calculations, Δ can be derived for an intersection site A connected to three other scattering sites (labeled A_{1-3}) by leads of a single lattice spacing as (see Fig. 3.1):

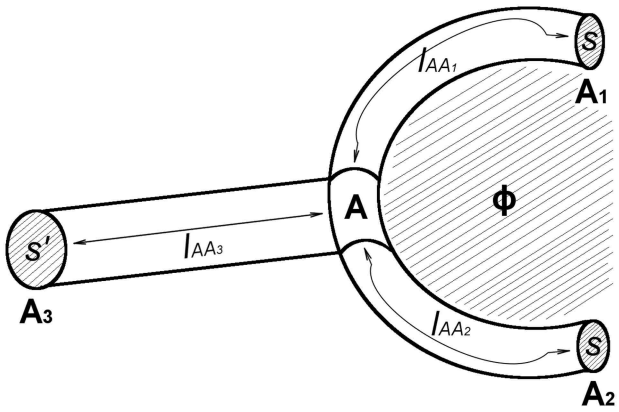

Figure 3.1: Lattice-structured quantum network which forms the basis for the global node equation method. The boundary condition for conservation of momentum at A allow us to form a linear set of equations describing the stationary states at each of the scattering sites.

$$s_1\Psi(A_1)\csc kl_{AA_1} = s_1\Psi(A)[\cot kl_{AA_1} - \tan\delta_{AA_1}]e^{-i\theta_{AA_1}}$$
$$s_2\Psi(A_2)\csc kl_{AA_2} = s_2\Psi(A)[\cot kl_{AA_2} - \tan\delta_{AA_2}]e^{-i\theta_{AA_2}}$$
$$s_3\Psi(A_3)\csc kl_{AA_3} = s_3\Psi(A)[\cot kl_{AA_3} - \tan\delta_{AA_3}]e^{-i\theta_{AA_3}} \qquad \text{(II.3)}$$

where cross sections $s_1 = s_2 = s$, $s_3 = s'$, lengths $l_{AA_1} = l_{AA_2} = l_{AA_3} = l$, and phase factor $\theta_{AA_j} = \frac{1}{\Phi_0}\int_0^l \mathbf{A}(x')\cdot d\mathbf{x}'$. Satisfying conservation of current, $\sum_{j=1}^{3}\tan\delta_{AA_j} = 0$, with $\tan\delta_{AA_j} = i\frac{C_{AA_j}-D_{AA_j}}{C_{AA_j}+D_{AA_j}}$, where C and D are the outgoing and incoming amplitudes along path AA_j, respectively. If the external terminal is connected along the non flux-modulated path l_{AA_3}, then $\theta_{AA_3} = 0$ and we can define $\Delta = \frac{s'}{s}$. Rewriting the localized linear set of equations in homogeneous form gives:

$$\Psi(A)[2\cot kl + \Delta\tan\delta_{AA_3}] - \csc kl\sum_{j=1}^{2} e^{i\theta_{AA_j}}\Psi(A_j) = 0 \qquad \text{(II.4)}$$

This is equivalent to the traditional S-matrix formulation shown by Büttiker [41]. Note that $\Delta = 1$ corresponds to maximum coupling while $\Delta = 0$ describes the isolated unperturbed rings. If this approach is globally extended to each scattering site in the network, a secular equation can be formed for the eigenenergies that will lead to the calculations of the reflection and transmission amplitudes of the test signal for given terminal sites [1].

3.1. STRONG ENTANGLEMENT WITH VARYING EXTERNAL PERTURBATION STRENGTHS

It is possible to construct a half-adder circuit with two AB rings entangled by two shared center bond lengths, where all four pairing states can be satisfied classically. This network presumes a strong and permanent perturbation, or $\Delta = 1$. Quantum networks are understood to be of a waveguide nature. We have shown previously how a test signal can be transported through multiple-terminal networks

[1, 34, 35, 62]. Transport with a test signal for a three-terminal network can be generally divided into three primary classes: dominant, half-sharing, or equal-sharing between the output terminals. From the truth table for a half-adder, it is simple to see that only a single output should be $|1\rangle$ for any given flux combination. Therefore a dominant class of transport is favorable for this form of computation. From our calculations, we see that if the coupling parameter between the external terminals and the rings begins to weaken, then the transport classification begins to change. The domination for the sum and carry terminals begins to be weakened slowly into a more distributed class. Therefore the ability to take a high-fidelity measurement of the computation through the test signal is absent at weak coupling parameters, leaving indistinguishable readout results. This is shown in Fig. 3.2.

3.2. WEAK ENTANGLEMENT WITH VARYING EXTERNAL PERTURBATION STRENGTHS

In Fig. 2.1(a), we show that for point-contact coupled AB loops, superposition of states exist at $|\Phi| = \frac{1}{2}\Phi_0$ and 0. This is the situation for a weakest entanglement. The question is whether this can be accompanied by a weak external perturbation to provide a classical readout. For comparison, we investigated the two weakest entangled AB rings, where superposition of all four states exists before the attachment of external terminals. Since there is no shared center path between the two partial waves in each ring, the eigenenergies remain unchanged for applied fluxes $\phi_1 = \pm\phi_2$. This is due to the associated secular equation only having flux terms contained within cosines [1]. The result is that the electron transport is sign-invariant for one of the fluxes, and thus there are only two possible electron wavefunction output vectors in the weakest entanglement, instead of four. For half-adder addition, this is not desirable since there needs to be a total of three distinct output states. The results are shown in Fig. 3.3. For the class of point-contacted AB rings, with an odd number

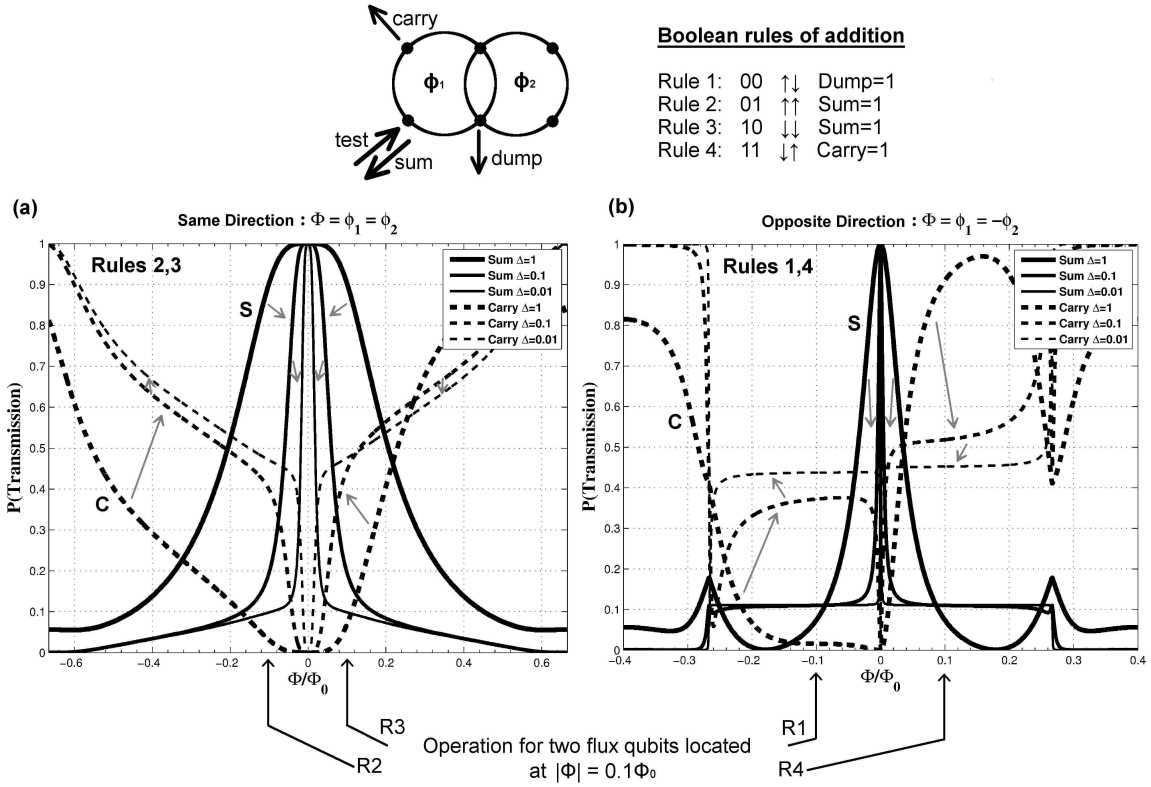

Figure 3.2: Two strongly-coupled AB rings, beyond the point-contact situation, is shown in the upper figures. When $\phi_1 = \phi_2 = \pm 0.1\Phi_0$ in (a), a test signal from the sum terminal, results in a total reflection, so that the output at the sum terminal ≈ 0.9, while the carry terminal output ≈ 0.1. The two results are mapped into the Boolean algebra rules of addition for two bits 1 and 0. This is shown in the bold solid curve when $\Delta = 1$ (strong external coupling). The grayscale arrows indicate the progression as the coupling is reduced. When Δ is reduced, the results are no longer valid because the sum/carry relation changes into different, less distinguishable modes ($\Delta = 0.1$ and 0.01). In (b) when $\phi_1 = -\phi_2 = 0.1\Phi_0$, the carry terminal ≈ 0.9 while the sum terminal ≈ 0.1. This maps into the Boolean algebra rules of addition for two bits 1 and 1. On the other hand when $\phi_1 = -\phi_2 = -0.1\Phi_0$, both carry and sum terminals are low, and the output goes to the third dump terminal (not shown). This maps into the addition for two bits 0 and 0. The above statement is valid only at $\Delta = 1$, the maximum external coupling situation. When Δ is reduced to 0.1 or 0.01, the results are not valid as shown in the dotted curves. Thus a workable half-adder we have shown here has uniform cross-sectional area throughout the rings and the external leads.

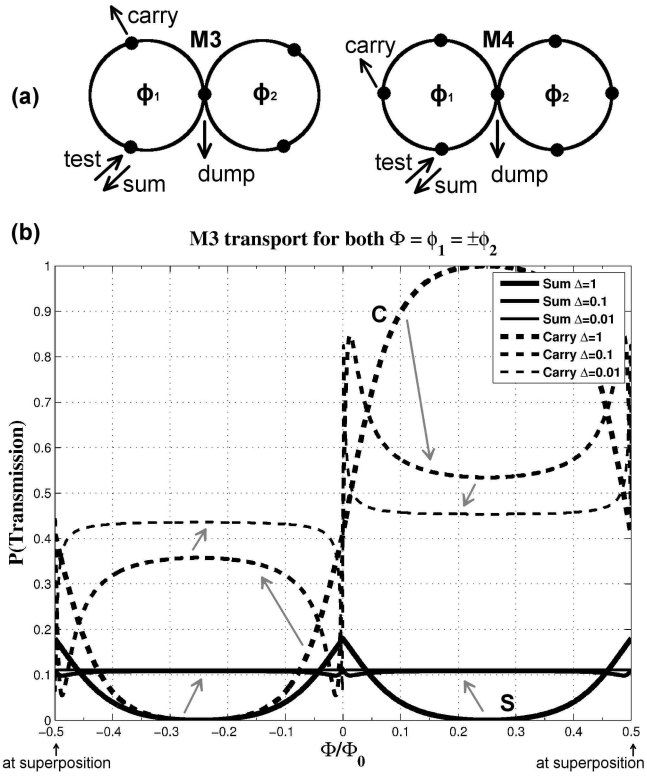

Figure 3.3: Weak entanglement versions of the half adder circuit. (a) Odd M3 and even M4 point-contact circuits. (b) M3 point-contact network transport as external terminal coupling is varied. The grayscale arrows indicate the progression as the coupling is reduced. The third (dump) terminal in our original work is not shown, since it only collects unwanted computations. Note that the results are for all four equal-magnitude angular momentum pairings, since the transport is sign-invariant for ϕ_2. In $\Delta = 1$ situation, it behaves like a quantum circulator [34]. As external terminals are weakened, the transport approaches equal-distribution between the carry and dump (not shown). Note the flux period for point-contact entanglements are the same as for a single ring, $\Phi = \Phi_0$.

of atoms in each ring, labeled as M3, we found a gradual transport trend. The two output states are slowly degraded from dominant transport at one terminal to a more distributed situation. For the second class of two even point-contacted rings, M4, the test signal is completely reflected across the entire flux period for all non-zero coupling strengths (not shown), and is therefore not useful for computation. In summary,

lowering the coupling strength between the external terminals and the network will generally degrade the readouts to such a point where the computation can no longer be reliably found or distinguished. Therefore there is no possibility of a classical readout, even though the unperturbed coupled rings can exhibit a superposition of states. This is because superposition of states holds true only in a closed system, while readout possibility is from an open system only. In special cases where there is total reflection of a test signal across the entire first Brillouin zone, this does not hold true as changes in coupling strength have no effect on the output.

4. CONCLUSIONS

In this paper, we show that as long as a single qubit, which is angular momentum based, can be established in a man-made atom, or an AB ring, quantum computing can be made without the need to check the extent of entanglement for superpositional flux qubits in order to guarantee the classical readouts. The superposition nature of such networks is due to the fact that electron wavefunctions are composed of coupled harmonic oscillators (in the global node equation) in an AB ring and hence at the Brillouin zone boundary a switching of the direction of the angular momentum can occur. Therefore the subsequent constructions for the entanglement of two coupled AB rings to serve as a half-adder circuit as well as the required setup for a classical readout do not necessarily follow the procedures outlined by earlier investigators. The existence of a superposition for qubits has long been assumed when there is entanglement. This is required strictly for a closed system only. However, our results lead us to believe that superposition of states may not be needed for classical readout results because the readouts require an open system. Our findings point out that there is an interplay between the entanglement (internal coupling) and the external perturbation configuration (external coupling). The entanglement can be provided in such a way that there is a loss of superposition while the external connections are attached. We show indeed that classical readouts are possible at the loss of superposition. The conventional wisdom of having a perfect internal quantum computation scheme first (closed system) and then reading the result with weak or indirect measurement, in order to keep the system closed, turn out not to be valid in our quantum network example shown here and therefore is necessarily not valid in the general situation. In general, attempting to sample a closed quantum network in a superposition with a test signal results in a rejection of the probes with complete reflection. We have shown that strong external perturbations can provide

high-fidelity classical readouts, while weak perturbations generally switch the quantum circuit from one class (dominant output) to another weaker (distributed output) class that cannot provide any useful readouts. In quantum computing, as long as it is qubit-based at the start, the internal couplings of qubits (the entanglement) and the external couplings for collapsing the internal quantum state to a classical distribution (the setup for readouts) are one integral part of a circuit that cannot be considered separately. For robust classical measurements, a strong external perturbation must be paired with a strong enough entanglement that can destroy the superposition of the two qubits. Any other combination of external and internal couplings will not lead to this desired computational output behavior.

While qubit-based quantum computing is shown to be able to perform so called "massive parallel computing" as shown by Shor's algorithm [11] for fast factorization, a fundamental problem still exists at the very elementary level of simply adding two n-bit binary strings together. This is analagous to performing the Fourier transform in optical computing [3], which is a special case that a single lens gate can solve in parallel. However this in no way implies that such parallelism can be extended to general arithmetic logic operations that depend on addition-based Boolean algebra. In quantum network theory, we show one possibility to integrate a quantum algorithm with strong external perturbations so that high-fidelity classical measurement is possible. In our scheme, superposition of angular momentum states can exist in a closed system fashion, but needs to be collapsed in coordination with the readout configuration in an open system. The coordination scheme we have demonstrated is to strengthen the internal coupling, at a loss of superposition with the attachment of strong externally coupled terminals to form said open system. Any other combination will not provide meaningful readout results in our model. In summary, a closed system has been transformed into an open and useful system.

III. THÉVENIN EQUIVALENCE IN DISORDERLESS QUANTUM NETWORKS

C. A. Cain[1] and C. H. Wu[1]

[1]*Department of Electrical & Computer Engineering*

Missouri University of Science & Technology

301 W 16th St, Rolla, Missouri 65409, USA

ABSTRACT*

We outline the procedure of extending the Thévenin equivalence principle for classical electric circuits to reducing Aharonov-Bohm-based quantum networks into equivalent models. With examples, we show from first principles how the requirements are related to the electron band structure's Fermi level and the lattice spacing of the network. Quantum networks of varying degrees of coupling strength from four basic classifications of single and double entangled loops sharing symmetry and highly-correlated band structures are used to demonstrate the concept. We show the limitations of how the principle may be applied. Several classes of examples are given and their equivalent forms are shown.

*Published in Journal of Applied Physics **117** 024308 (2015).

1. INTRODUCTION

Quantum networks in the mesoscopic range have been well-studied over the last few decades [5, 16, 17, 18, 19, 21, 22, 37, 39, 40, 41, 61], with more recent work focusing on higher-order effects and topics such as spin transport due to their potential development for quantum computation [20, 63, 64, 65, 66, 67, 68, 69, 70, 71, 72, 73]. Quantum networks consist of quasi-one-dimensional paths and nodes connected together. Because of the existence of loops, the Aharonov-Bohm (AB) effect can be applied to further modulate the phase of the electron wavefunction along the paths where Schrödinger's equation is satisfied. Over the last few years, we have been investigating the behavior when a few AB rings are coupled for quantum computing [1, 62, 74]. For this purpose, it is important to identify whether these quantum networks have the potential to replace conventional electric circuits with new ones based on the phase-modulation concept.

One area that has yet to be explored for these complex quantum networks is the concept of equivalence. In classical circuits, such as the simple resistive network shown in Fig. 1.1(a), Léon Thévenin famously showed in the 1800's that it is possible to form a simpler equivalent version for part of the circuit [75]. The simplified network preserves the total current and voltage difference being delivered to the unaltered part of the circuit. This has long been a useful analysis tool in simplifying complex electronic designs to better understand their behavior. We have recently shown a quantum network-based processor utilizing symbolic substitution rules, not superposition of flux qubits [76]. Therefore the question of extending Thévenin's theorem to quantum networks becomes an important means for simplification and gaining physical insight about them. For a general classic circuit the system is lossy and the transport is incoherent. Thus when forming an equivalent circuit, the equivalent current being delivered to the unaltered part of the circuit in both models will

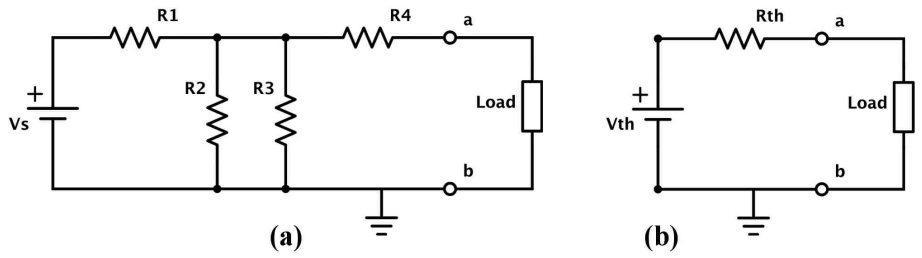

Figure 1.1: (a) Simple resistor network with a voltage source Vs driving a load connected at terminals a and b. (b) Thévenin equivalent model that delivers an equal current through the terminals a and b to the same unaltered load. Vth is the open circuit voltage of the original network without the load connected, and Rth is the equivalent output resistance.

be a scalar. However at the mesoscopic level, where ballistic transport and elastic scattering are possible, the quantum circuits take into effect the magnitude and phase of the electron wavefunction in relation to the band structure and chemical potential. These can obviously differ between the original and equivalent models. In this work we attempt to determine how these restrictions affect the possibility of finding such equivalent networks.

The remainder of the paper is divided into three parts. Sec. 2 will define a quantum network and its properties as well as outline the analytical model used in our calculations. Sec. 3 is divided into three subsections, with the first describing the general requirements that need to be met between two networks in order to satisfy an equivalence. The remaining two subsections focus on determining which specific quantum networks can meet this criteria based on their coupling strength. Finally the results and observations are summarized in Sec. 4.

2. PHYSICAL MODEL AND CALCULATION METHOD

Electron transport in AB-modulated networks can be modeled in a multiply-connected space of uniform quasi-1D paths of length l interconnected by M nodes. It is placed between two thermal reservoirs with a small chemical potential difference $\mu_H - \mu_L$ at infinity, which acts as the source and sink of the electron. There is also an external magnetic flux Φ present, as shown in Fig. 2.1. In these quantum networks, the well-known Landauer-Büttiker formula for conductance applies between any two points in the network. In Fig. 2.1, nodes A and C are the elastic scatterers. The system's transport can be tuned by modifying the flux inside the loop, which alters the phase of the electron wavefunction within the paths. The transport between any two points i and j needs to satisfy the Büttiker symmetry principle $T_{ij}(\Phi) = T_{ji}(-\Phi)$ [43, 77].

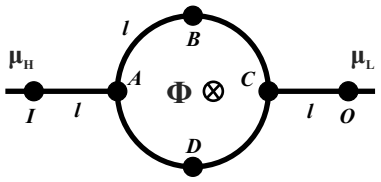

Figure 2.1: Single symmetric two-terminal AB ring consisting of four nodes and lattice spacing l, placed between terminals of chemical potential difference $\mu_H - \mu_L$. H and L are the higher and lower potentials, respectively. A magnetic flux Φ penetrates the loop, adding an additional phase factor to the electron wavefunction. At each node (A,B,C,D), there is an associated node equation that relates the wavefunctions between other adjacent nodes.

A brief formulation of the model will be presented here, with a more complete description given in previous work [4]. The Schrödinger equation must be satisfied at any point in the ring. For a single free electron situation, the solution between nodes A and B can be given as

$$\Psi_{AB}(x) = [P_{AB}e^{-ikx} + Q_{AB}e^{ikx}]e^{-iS(x)/\hbar} \tag{III.1}$$

where $\Psi_{AB}(0) = \Psi_{AB}(A)$, and $\Psi_{AB}(l) = \Psi_{AB}(B)$. P_{AB} and Q_{AB} are the complex outgoing and incoming wave amplitudes from A in the path, respectively. S is a phase factor introduced due to the magnetic vector potential $\mathbf{A}$ and is given by the path integral

$$S(x)/\hbar = \frac{e}{\hbar c}\int_0^x \mathbf{A}(x')\cdot d\mathbf{x}' = \frac{x}{r}\left[\frac{\Phi}{\Phi_0}\right] \tag{III.2}$$

where x/r is the angular displacement and the elementary flux quantum $\Phi_0 = hc/e$. A is connected to a total of three nodes: B, D, and I. A simplified set of equations can then be formed as

$$\begin{aligned}
\Psi(B) &= \Psi(A)[\cos kl - \tan\delta_{AB}\sin kl]e^{-i\phi} \\
\Psi(D) &= \Psi(A)[\cos kl - \tan\delta_{AD}\sin kl]e^{i\phi} \\
\Psi(I) &= \Psi(A)[\cos kl - \tan\delta_{AI}\sin kl]
\end{aligned} \tag{III.3}$$

where $\phi = (2\pi/M)(\Phi/\Phi_0)$. For a neighbor node j, $\tan\delta_{Aj} = i\frac{P_{Aj}-Q_{Aj}}{P_{Aj}+Q_{Aj}}$ and the reflection coefficient $R_{Aj} = (P_{Aj}/Q_{Aj})$. Conservation of probability current requires $\sum_j \tan\delta_{Aj} = 0$, and allows one to reduce the set of Eq. (III.3) into a single node equation for A as

$$\Psi(A)\left[2\cos kl + \tan\delta_{AI}\sin kl\right] - e^{i\phi}\Psi(B) - e^{-i\phi}\Psi(D) = 0. \tag{III.4}$$

A similar node equation can be found for the other three nodes in the ring. To calculate the energy spectrum, the isolated system is considered first (no terminals). This fixes $\tan\delta_{AI} = 0$ in Eq. (III.4). The secular determinant for the four node equations becomes

$$16\cos^4 kl - 16\cos^2 kl - 2\cos 4\phi + 2 = 0. \tag{III.5}$$

The four possible energy states $E_n = k_n^2(h^2/8\pi^2 m)$ can then be found, with m being the electron mass. The half-filled Fermi energy state E_F at $T = 0K$ is then used to solve for the transport. The terminals are considered a perturbation to the system, leading to the transmission and reflection coefficients. This is consistent with the S-matrix results first reported by Büttiker, et al [41]. We have used this method to study more complicated AB ring configurations in the past [34, 35].

3. THÉVENIN EQUIVALENCE

3.1. REQUIREMENTS

There are four basic classes of AB rings, determined by the number of M nodes in the ring: $M = 4N$, $4N + 2$, $4N + 1$, and $4N + 3$, with N an integer. More complicated quantum networks can then be formed by coupling these AB rings together with different strengths and attaching several terminals. The key question is, under what circumstances can these quantum networks be simplified like the classical circuit example in Fig. 1.1? Clearly, if the state of a system and its equivalent form need to be identical at a node, significant restrictions will be imposed. The band structure becomes the first factor in determining whether or not a given network can be substituted for another. The scaling relations for the transport in AB rings investigated previously provide some insight [62]. For a symmetric ring such as the example in Fig. 2.1, it is possible to scale the network by any integer factor and still preserve the general band structure and hence the transport. The Fermi energy E_F and wavevector k_F for both structures are identical. When attempting to replace a portion of a quantum network with a simplified equivalent form, the node equations (as in Eq. (III.4)) for the unaltered portion of the network need to be identical. Due to these requirements, the correlation between the band structures of two different networks needs to be strong but not necessarily identical. In general, they will need to share some form of symmetry. Also, the correlation depends on the strength of the coupling between the AB rings. Ideally, E_F should be equal across the entire flux period to have the highest likelihood of satisfying the equivalence. This is satisfied by point-contact coupled rings and will be shown first. The following two subsections are divided by coupling strength for the four basic classes of coupled AB rings.

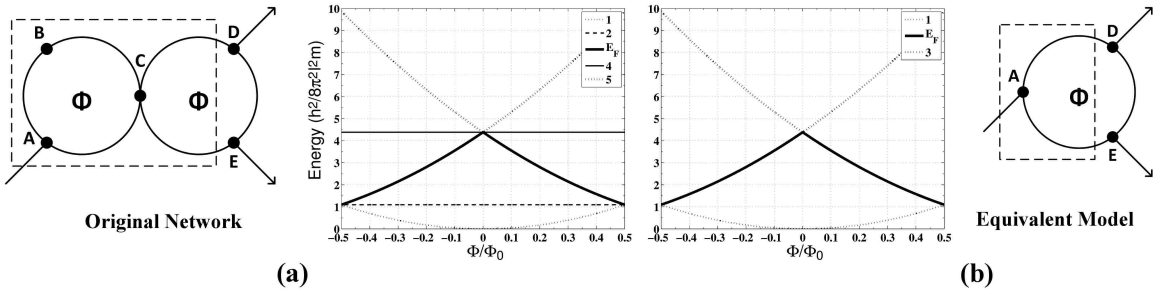

Figure 3.1: (a) Network diagram and energy band structure (in units of $h^2/8\pi^2 l^2 m$) for two $M = 3$ point-contacted loops. The dashed portion of the network will be replaced with an equivalent form shown in (b). The output nodes D and E remain unchanged. The lines in the band diagrams correspond to the energy states computed from the secular determinants of each network, similar to that of Eq. (III.5). Note that in (a) there are five nodes and thus five energy states, two of which are flux invariant. In (b) there are three nodes and three energy states, which are identical to the flux dependent states in (a). The Fermi energies E_F for both networks are aligned across the entire flux period.

3.2. POINT-CONTACTED LOOPS

Point-contacted AB loops are a suitable starting point to demonstrate Thévenin equivalence. They share an identical band structure with a single ring, only with extra flux-invariant states added. Even though the Fermi energies are equal, it is not possible to meet the equivalence conditions across the entire flux range. We show an equivalent circuit is only possible at a pair of flux values. Beginning with a network consisting of odd point-contacted $M = 3$ rings belonging to the $4N + 3$ class, shown in Fig. 3.1, it can be shown that its Fermi energy is equivalent to that of a single ring. This is due to the symmetry of the structure, though the point-contact causes the transmission to be compressed into a narrower flux range due to a resonant tunneling effect.

If three terminals are attached, as shown in Fig. 3.1(a), a Thévenin equivalent can be given in Fig. 3.1(b) where the left portion of the network is replaced with a

single odd three-terminal ring. This happens to be a quantum circulator [34]. The wavefunction magnitudes for nodes D and E in both networks are shown in Fig. 3.2, with peaks at $|\Phi| = \Phi_0/4$ with Fermi wavevector $k_F = \pi/2l$. This value leads to the $\cos kl$ term in Eq. (III.4) vanishing at each node. The two node equations at B and C in the original network now only contain phase terms between the wavefunctions at adjacent nodes. The remaining three node equations take on a similar form of the equivalent single ring. The preserved part of the network does not necessarily have to contain two output terminals. For instance, if either one of the output terminals were removed to form a simpler two-terminal network, the Thévenin conditions would still hold. The wavefunctions at D and E between the two networks do however vary by a constant phase factor $\theta = \pi/3$. This can be offset by preparing the incident electron with a phase of θ to align the two network states. This means the inputs for the two equivalent networks need to differ by θ in phase space to obtain complete equivalence. Note that by scaling the number of nodes M in both rings by any odd integer, the same equivalence can be maintained.

The second example is the $M = 4N+1$ class. The point-contacted $M = 5$ AB rings are shown for the two-terminal situation in Fig. 3.3(a). It is possible to replace the left side of the network with the smaller equivalent form of a single loop. In this case four nodes (E,F,G,H) are in the unaltered part of the network, one being the output terminal. In this case, the Fermi energy levels between the two networks are identical across the entire flux period. The Thévenin condition is again satisfied at $|\Phi| = \Phi_0/4$.

However for the even-numbered $4N$ or $4N+2$ class, it is not possible to satisfy the equivalence requirements since their Fermi levels are independent of the applied flux. The incident electron is totally reflected to the input terminal, which does not occur for even-numbered, single rings. Therefore none of the Thévenin conditions are satisfied other than sharing the same lattice spacing l.

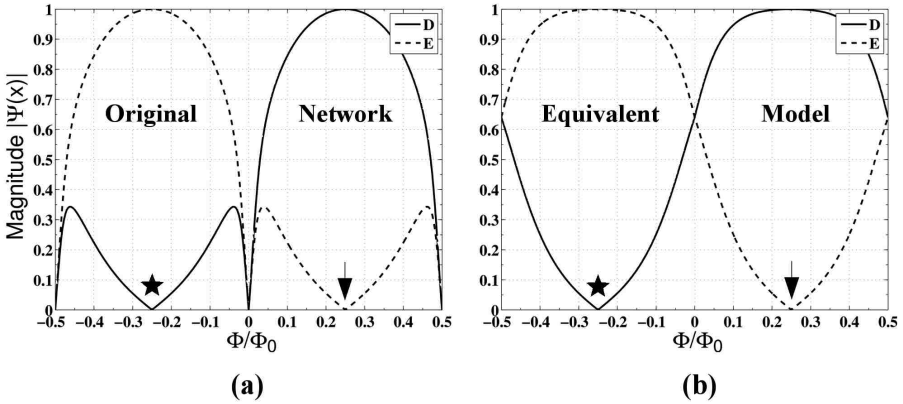

Figure 3.2: Wavefunction magnitude of outputs D and E for the point-contacted network and its equivalent model given in Fig. 3.1. While the Fermi energies are equivalent across the entire period, the equivalence conditions are only met at two flux values $|\Phi| = \Phi_0/4$. This is indicated by the pair of arrows and stars, with corresponding energy $E = h^2/32l^2m$. This is because the $\cos kl$ terms vanish in the node equations since the Fermi wavevector $k_F = \pi/2l$. There is a phase shift of $\pi/3$ rad between the two networks for both flux values at nodes D and E. To obtain complete equivalence, the inputs at A in both networks need to differ by this constant phase.

3.3. STRONG COUPLED LOOPS

There are two types of strong coupling: the loops can share a single scattering path, or they can share two. A single path is the strongest form. For a single path in each of the four classes, the energy states that form the band structures are distorted from those of a single ring. Another issue that complicates stronger coupling is that the flux period becomes a rational number, not Φ_0 [1]. However there are instances where the Fermi levels happen to align with an equivalent single loop. The problem is this may only be true for a single flux value, as opposed to a wide range. This gives little flexibility in trying to meet the other Thévenin requirements such as matching the wavefunctions and transmission in the preserved part of the circuit. Due to this, forming an equivalent model from a network of loops coupled by single paths is not possible.

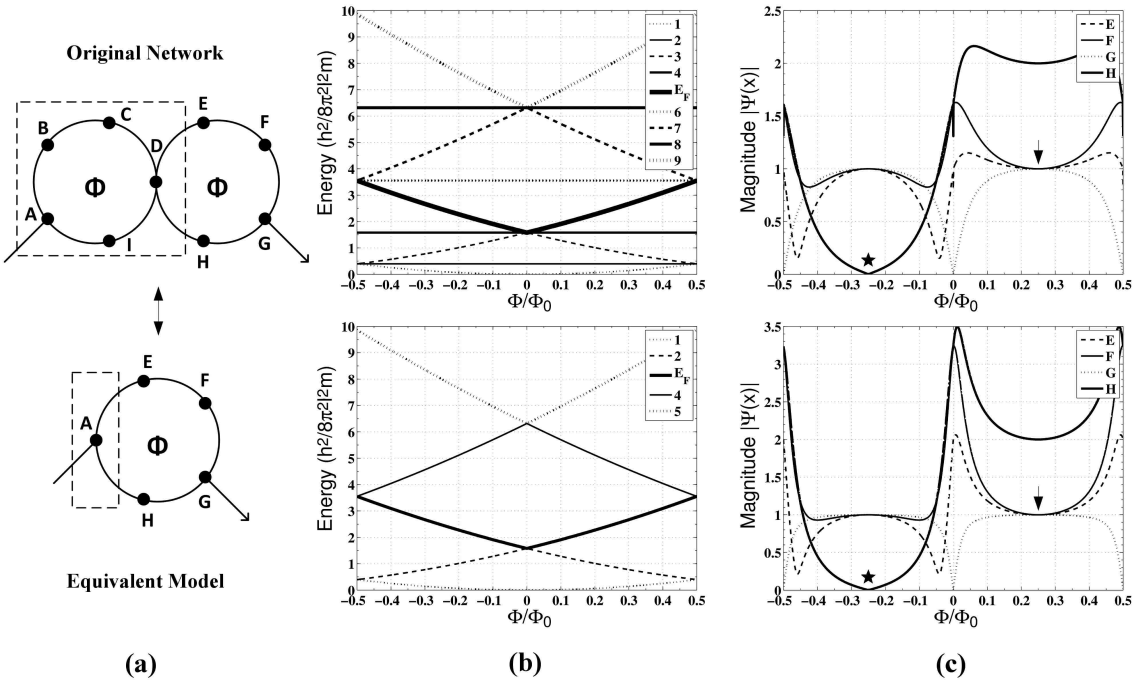

Figure 3.3: (a) Diagram of point-contacted $M = 5$ loops with an equivalent single ring. (b) Energy band structures (in units of $h^2/8\pi^2 l^2 m$) of both networks computed from their secular determinants, similar to Eq. (III.5). (c) Wavefunction magnitude for the preserved nodes in each system. The equivalence conditions are only met at two flux values $|\Phi| = \Phi_0/4$, indicated by the pair of arrows and stars, with corresponding energy $E = h^2/32l^2m$. This is because the $\cos kl$ terms vanish in the node equations since the Fermi wavevector $k_F = \pi/2l$. There is a phase difference of $\approx 5/2$ rad between the two networks for both flux values at nodes E, F, G, and H. To obtain complete equivalence, the inputs at A in both networks need to differ by this constant phase.

Since the strongest form of coupled AB rings is ruled out for equivalence, we examine the coupled networks which share two center common paths. While providing two paths for an electron to scatter, the energy levels are altered. In this case, it is not possible to meet all equivalence conditions when the two applied fluxes $\Phi_1 = \Phi_2$. However, an interesting pattern in the band structures for all four classes is found when $\Phi_1 = -\Phi_2$. The Fermi levels for these coupled networks show similarities to a single ring by scaling the value of the electron charge in the ring. In Fig. 3.4(b),

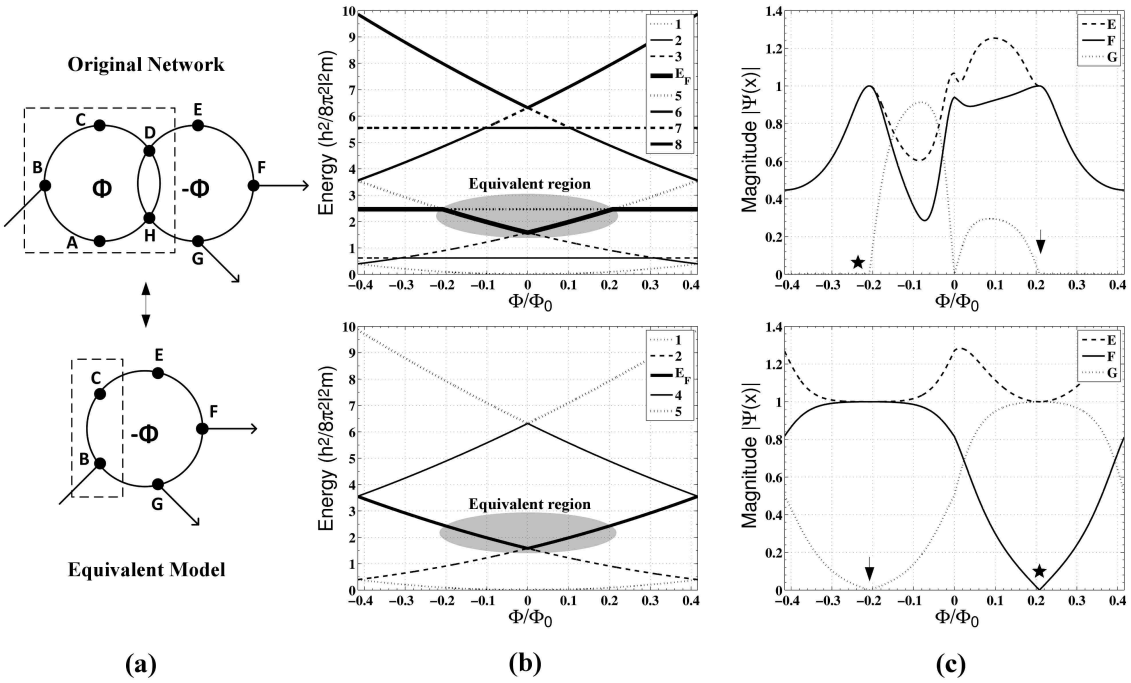

Figure 3.4: (a) Diagram of two path coupled $M = 5$ loops with an equivalent single ring. (b) Energy band structures (in units of $h^2/8\pi^2 l^2 m$) of both networks computed from their secular determinants, similar to Eq. (III.5). The Fermi energies are equivalent in the range $|\Phi| \leq 5\Phi_0/24$, indicated by the shaded region. (c) Wavefunction magnitude for the preserved nodes in each system. All equivalence requirements are satisfied at the two flux values $\pm 5\Phi_0/24$, indicated by the pair of arrows and stars. These points correspond to the same energy as in the point-contact examples, $E = h^2/32l^2m$. This is because the $\cos kl$ terms vanish in the node equations since the Fermi wavevector $k_F = \pi/2l$. The phase difference at nodes E, F, and G between both networks is $\approx \pi^2/4$ rad for the arrow flux values and $\approx 43/64$ rad for the starred values. To obtain complete equivalence, the inputs at B in both networks need to differ by these constant phases.

the equivalent Fermi energy region is shown after the electron charge in a single ring is adjusted. Note that when the applied fluxes are opposite in direction, the phase modulation along the center common paths is no longer zero (compared to when the applied fluxes are equal). This leads to a net persistent current flowing in the two

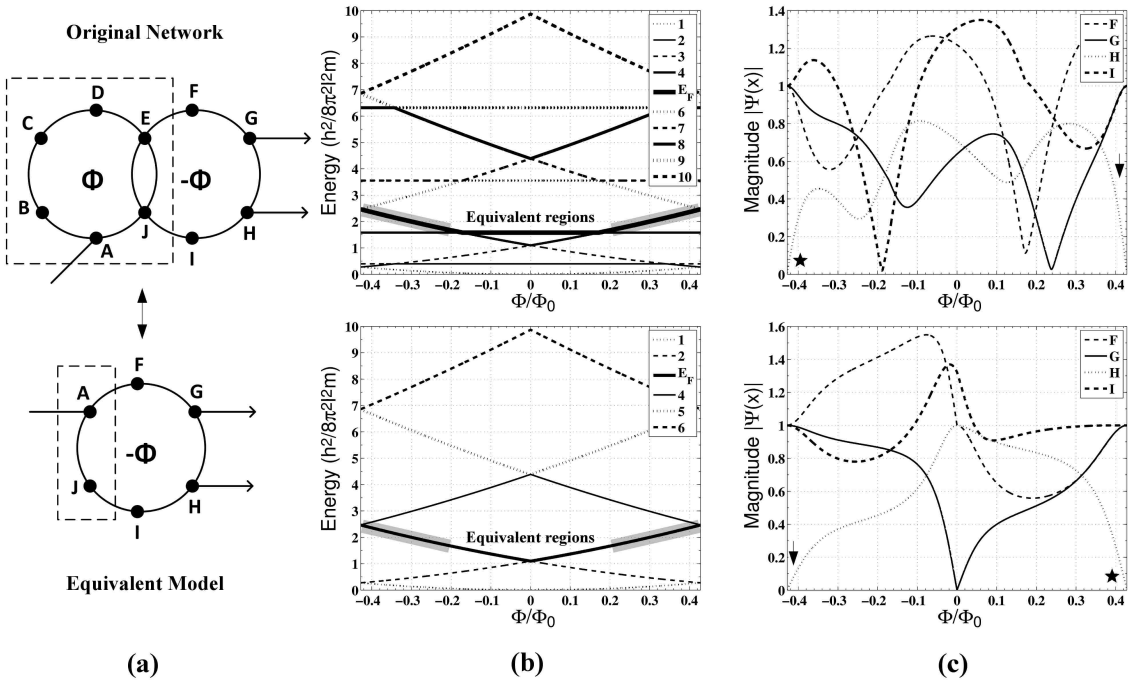

Figure 3.5: (a) Diagram of two path coupled $M = 6$ loops with an equivalent single ring. (b) Energy band structures (in units of $h^2/8\pi^2 l^2 m$) of both networks computed from their secular determinants, similar to Eq. (III.5). The Fermi energies are equivalent between $6\Phi_0/35 \leq |\Phi| \leq 6\Phi_0/14$, indicated by the two shaded regions. (c) Wavefunction magnitude for the preserved nodes in each system. At the zone boundary all equivalence conditions are met, which like the other examples corresponds to energy $E = h^2/32l^2m$. This is because the $\cos kl$ terms vanish in the node equations since the Fermi wavevector $k_F = \pi/2l$. The phase difference at nodes F, G, H and I between both networks is ≈ 2 rad for the arrow flux values and $\approx 15/8$ rad for the starred values. To obtain complete equivalence, the inputs at A in both networks need to differ by these constant phases.

common paths and indicates that the band structure must be similar to a single ring (where persistent current is present in all paths).

By considering all possible terminal configurations, the smallest odd $4N + 3$ ($M = 3$) and even $4N$ ($M = 4$) coupled networks are ruled out. While their Fermi levels can be aligned by renormalizing the value of charge in the single rings, the wavefunction distributions do not match for any terminal configuration. However for

the smallest $4N+1$ network ($M = 5$), which is larger than the previous two ($M = 3$, $M = 4$), we can find all equivalence requirements satisfied. In the Fig. 3.4 example, the Fermi levels can be aligned between the coupled network with period $5\Phi_0/6$ and a single $M = 5$ ring. The single ring has to be prepared with fractional charge $6e/5$ to yield $\Phi_0' = 5\Phi_0/6$. This allows the Fermi energies to be equal in half of the flux range $|\Phi| \leq 5\Phi_0/24$. If three terminals are attached as shown in Fig. 3.4(a), an exact equivalence can be achieved at the boundaries of this region $|\Phi| = 5\Phi_0/24$. The transmission circulates between unity at each output, and occurs at the same Fermi wavevector value as the point contact examples discussed previously, $k_F = \pi/2l$. This is not the only viable terminal configuration. By symmetry, one can rearrange the output terminal from G to E while inverting the two flux directions and still satisfy all the equivalence requirements.

The last example is for an even-numbered $4N+2$ class represented by $M = 6$ and shown in Fig. 3.5(a), which happens to have particular regions that are able to meet all equivalence conditions. The flux period of this network is $6\Phi_0/7$. A fractional charge of $7e/6$ can be prepared in the single $M = 6$ ring to alter the flux period and align the Fermi energies in the range $6\Phi_0/35 \leq |\Phi| \leq 6\Phi_0/14$ as shown in Fig. 3.5(b). At the zone boundary $|\Phi| = 6\Phi_0/14$, both networks fully transport through terminal G. Note that the boundary of the equivalent network portion could be extended to include nodes F and I if desired. The Fermi energy and wavevector are consistent with the same values found in all the other examples presented. This is clearly an interesting observation.

4. CONCLUSION

We have shown there are possibilities to extend Thévenin's theorem for classical electric circuits into the quantum network regime. For an equivalence to be valid, the node equations for both networks need to be identical in the unaltered part of the circuit. The requirements dictate that the two equivalent networks need to have the same Fermi energies, attributable to the specific structures and applied fluxes involved. In order for the band structures of two networks to be equivalent, and hence suitable for such a transformation, there needs to be some form of symmetry or scaling relation between the two respective networks. This requires the same lattice spacing in both structures. We began with the concept of a single ring being scaled, known to be valid from prior work. The idea was then extended to the four basic AB ring classes, $M = 4N$, $4N+1$, $4N+2$, and $4N+3$, at point-contact coupling. These networks share identical band structures with that of a single ring of the same class but with extra flux invariant states added. With the ability to look for an equivalence across the entire flux period, several examples were identified. Only two classes of rings exist where Thévenin's principle can be applied, when $M = 4N+1$ or $4N+3$. For the even-numbered classes the Fermi energy levels are flux invariant. There is total reflection for any input, making it impossible to find an equivalent network. The Thévenin equivalent is valid up to where the inputs can differ by a constant phase factor. If two point-contacted loops can satisfy all Thévenin requirements, then it is reasonable to assume this can be extended to an arbitrarily large number of point-contacted loops. This would simply reduce the valid flux range consistent with multi-stage resonant tunneling.

We further investigated the four classes of coupled AB rings with varying coupling strengths. Two cases are presented: a single path (strongest) and a weaker double path. For double paths, the entanglement of the loops is still weak enough

that the band structure is similar to a single ring if the two fluxes are opposite in direction. If the fluxes are equal there will be no net persistent current flowing in the shared center path, indicating the band structure will vary too greatly from the single ring spectrum. This kind of coupling changes the flux period to be a fraction of Φ_0. To have any potential Thévenin equivalence, the Fermi level needs to be aligned with that of a single ring. To achieve this, there must be a charge renormalization ($e \rightarrow 7e/6$, as an example). Only two suitable classes exist that meet all of the equivalence requirements. They are the odd-numbered $4N + 1$ and even-numbered $4N + 2$ classes. Consistent with the point-contact cases, the equivalence is only valid at specific flux values and only for a few select terminal configurations. In the valid instances presented, the Fermi energy is $h^2/32l^2m$ with wavevector $\pi/2l$. This leads to vanishing $\cos kl$ terms in the node equations for each network. The result is a more simplified set of node equation relations that allow for an equivalence to be obtained.

In summary, the possibility to extend Thévenin's equivalence principle to the mesoscopic regime is limited to specific circumstances, as one would expect. Here we have outlined what general requirements need to be met. For there to be any possibility of reducing a complex network, the coupling strength between loops formed needs to be weak. When the coupling becomes too strong, the band structure is distorted away from that of a single ring. This then eliminates any possibility of equivalence. With weaker coupling, there are class and terminal restrictions to meet the necessary conditions. In this work, we have focused on exploring these restrictions and providing examples that demonstrate the principle. For any general quantum network, an equivalence may be possible if the portion of the network to be replaced has weak coupling and no disorder.

IV. SIXTEEN TWO-VARIABLE BOOLEAN FUNCTIONS FROM QUANTUM NETWORKS OF AHARONOV-BOHM RINGS

C. A. Cain[1]

[1]*Department of Electrical & Computer Engineering*

Missouri University of Science & Technology

301 W 16th St, Rolla, Missouri 65409, USA

ABSTRACT*

Ballistic transport through four Aharonov-Bohm ring quantum networks that can satisfy all sixteen Boolean functions for two variables are reported here. A ring is considered an input flux qubit, which can be tuned in cooperation with a terminal configuration to satisfy the given rules for a function. Higher order functions require coupling two rings (inputs) together, where the entanglement between the spin states allow for a more complex set of rules to be satisfied. In order to achieve meaningful readouts, the superposition of the qubit state(s) must be eliminated first even before perturbing the system. The requirements for each of the four circuits are provided. Some comparisons are made between other types of quantum architectures that focus on Boolean algebra and sequential operations.

*In preparation for Journal of Applied Physics (2015).

1. INTRODUCTION

Transport in mesoscopic systems under the Aharonov-Bohm (AB) effect has been well studied for the past few decades [5, 16, 17, 18, 19, 21, 22, 39, 40, 41, 61]. More recently, renewed interest in these quantum networks has focused on spin transport and interference effects [64, 66, 67, 68, 69, 70, 72, 73]. This has been in large response to quantum computing architectures that operate on the basis of controlling quantum bits (qubits), which are in a superposition of $|1\rangle$ and $|0\rangle$ states. This is often accomplished optically or electronically, through the spin basis of a photon or electron. Unitary operations are performed on these input qubits to yield a final state as a complete closed system. It then has to couple to an external perturbation for measurement. The advantage of such a scheme is the potential for massive parallel processing due to the superposition. Instead of a single well-defined state of N bits, a superposed system of qubits can represent 2^N states at once. A significant amount of recent research has investigated such possible experimental configurations [78, 79, 80, 81, 82, 83, 84]. Some examples have been Shor's algorithm for prime factorization [12], and solving a linear set of equations [13].

The primary application of spintronics is for calculations that are parallel in nature. For example, Shor's algorithm relies on the quantum Fourier transform. The superposition of states is transformed repeatedly, wiping any periodicities along the way to arrive at a result. There is no sequential dependence of one state (or its result) with another. Obviously not all computing behaves this way. An example of a purely sequential calculation would be N-bit addition, where there is a state-to-state coupling due to the carry between bit positions. While Vedral et al. gave a quantum description for addition in the 90s [85], to date no physical implementation exists. There is clearly room in the quantum computation space to tackle sequential computing. One example of this has been Quantum Cellular Automata (QCA) by

Lent et al [86]. In this scheme, cells consist of quantum dots that electrons can occupy. The well-defined polarization state of each cell acts as the binary bit, and the system "computes" through a propagation of cell-to-cell Coulomb interactions. All of the cell states are then updated by a set of rules and are ready for the next cycle. Another more recent paradigm has been proposed which exploits the AB effect. Instead of a cell, this scheme uses a single AB ring as the basic unit for computation [34, 35]. This is shown in Fig. 1.1(a). The diameters are typically on the order of a micron. The applied flux penetrating the ring acts as an input and varies the phase of the electron wavefunction across a period equal to the universal flux quantum $\Phi_0 = hc/e$. This can be used to control the transport in a network when terminals are attached between reservoirs. More complicated calculations are achieved by coupling two single rings together [1, 36, 62], as shown in Fig. 1.1(b)-(c). If the coupling is strong the periodicity becomes a rational number. The "computing" mechanism itself is a shared interaction between the applied flux(es) and the terminal configuration. It was shown that a half-adder circuit was possible for two coupled rings (two flux qubits), albeit at a loss of superposition. There are a total of sixteen Boolean logic operations that can be performed on two binary bits. Strictly speaking, a logic device set is considered functionally complete if it can compute $\{AND, OR, NOT\}$. These are then used to construct logic gates for the other thirteen Boolean functions. In this paper AB ring networks that satisfy all sixteen Boolean functions are reported. This is accomplished with a single rule-based circuit for each function. They do not require a buildup of simpler gates as in the truth-table approach for current design methodologies.

In the remainder of the paper, a concise description of these networks and their operation is given. Sec. 2 first provides the calculation methods used to analyze the networks. This leads into Sec. 3, which describes four unique AB networks that satisfy the sixteen Boolean functions. Sec. 4 discusses practical considerations in the

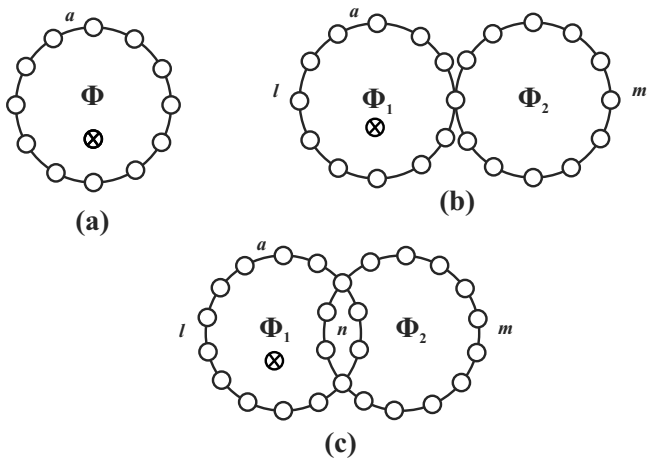

Figure 1.1: Generalized AB ring configurations for (a) a single ring, (b) point-contact coupling between two rings, and (c) two rings coupled by two center common paths. The applied flux Φ penetrating the ring is assumed to be positive pointing into the page. (l, m, n) represent the total path lengths of the segment in units of lattice spacing a. The networks can be classified by the number of nodes (open dots) M in each ring. There are scaling relations (see Sec. 2) that describe how the properties of the networks behave under a change in lattice spacing or M.

approach and methodology, as well as some of the pros and cons compared to other implementations such as QCA. Lastly, concluding remarks are provided in Sec. 5.

2. BASIC CALCULATIONS

In this section, a brief description of a node equation approach for calculating the band structure and transport in AB networks will be given. A more complete treatment is given in previous work [1, 4]. One-dimensional quantum networks, such as those in Fig. 1.1, can be considered as a set of elastic scattering nodes interconnected by uniform bonds of length a in a uniform background of positive charge. At any point in the network the Schrödinger equation must be satisfied. In the presence of a magnetic field, the propagating electron inherits an additional phase factor. For any point x, with neighbor at point j and path length l_{xj} (in units of a), the Schrödinger equation can relate the wavefunctions $\Psi(x)$ and $\Psi(j)$ between the two points. If all neighbors j are considered, a Kirchhoff-like conservation equation for the free electron can be formed as in Eq. (1) of Ref. [1]:

$$\big(\sum_j \cot kl_{xj} - iD\big)\Psi(x) - \sum_j \csc kl_{xj} e^{i\phi l_{xj}}\Psi(j) = 0. \qquad \text{(IV.1)}$$

k is the wavevector, while ϕ is related to flux Φ and number of nodes M in the loop/ring by $\phi = \pm(2\pi/M)(\Phi/\Phi_0)$. D is a perturbation term in relation to node x, where $D = 0$ if no external terminal is attached, $D = (1-R)/(1+R)$ if an input (R is reflection amplitude), and $D = -1$ if an output. This form is similar to the de Gennes-Alexander theory in superconducting networks [37].

In order to calculate the band structure, the isolated system must be considered first. All of the perturbation terms D in the node equations of Eq. (IV.1) vanish. This leads to a set of N homogeneous equations, where N is the total number of nodes in the network. A secular equation can be formed, yielding N solutions for the wavevector k by solving for the roots of the cosine terms. The eigenenergies then become $E_n = (\hbar^2 k_n^2)/(2m)$, with m the electron mass. The Fermi energy E_F is then found in the half-filled situation at absolute zero. The persistent current I

circulating in the ring is calculated by the relation $I = \sum_n -c\partial E_n/\partial\Phi$, with n up to E_F [87]. To calculate the transport, terminals at a slight chemical potential gradient are attached to perturb the isolated system. The node equations now have non-zero D terms for at least two nodes, and are calculated at E_F. By conservation, solving for R leads to the transmission probability $T = 1 - |R|^2$. In the Landauer-Büttiker formulation [39, 40], linear transport is satisfied with conductance G being proportional to T. Additionally, the symmetry principle of transport between two terminals is satisfied [43, 77]. The node equation calculations for the transport are equivalent to the S-matrix results of the same network [41].

There are four primary classes of AB rings, grouped by the number of nodes in the ring. The two odd classes are $(M = 3, 7, 11, ..)$ and $(M = 5, 9, 13, ..)$. The two even classes are $(M = 4, 8, 12, ..)$ and $(M = 6, 10, 14, ..)$. For any AB network, there are scaling laws that allow a given network to be scaled up or down and still preserve transport behavior. This has been investigated in earlier work [62]. The lattice spacing a in a network can be scaled by any rational factor f and not affect the transport. The cosine form factors in Eq. (IV.1) are scaled up as $\cos kfl_{xj}$. This of course reduces all k values by $1/f$, and persistent current by $1/f^2$. In addition to scaling the lattice spacing, the path lengths (l, m, n) shown in Fig. 1.1 can be scaled by an odd f. This changes the number of nodes in the ring(s). The transport is preserved, but the persistent current is reduced by a factor now of $1/f$. Odd scaling always preserves the class of the ring. Even scaling is not viable in the general case since scaling by an even factor can cause the resulting new network to fall into a different class.

3. LOGIC CIRCUITS

There are a total of sixteen Boolean operations for two binary variables. In this section, it will be shown how four different AB ring networks of different classes can satisfy all of these operations. The circuits themselves can be considered as flux qubits, as shown in Fig. 3.1. They can be isolated, as in the single odd ring of panel (a), entangled weakly (as in (b)), or entangled strongly (as in (c)-(d)). A terminal configuration then perturbs the system to get a readout of the circuit. The challenge to satisfying digital logic is to first identify the class of AB ring(s) that can be useful for the given operation, and then find an appropriate terminal configuration and flux values to give the correct readout. For two flux qubits Φ_1 and Φ_2, there are a total of four input states: $\uparrow\uparrow, \downarrow\downarrow, \uparrow\downarrow, \downarrow\uparrow$. They are equal in magnitude but can differ in spin. Any of the four classic binary states can be assigned to any state of the flux qubits in the circuit. This is called "flux mapping." The flux qubits individually can be in a superposition at zero flux or the zone boundary. However, when two rings are coupled there is entanglement. At the weakest point-contact coupling, the superposition is unaffected. But at stronger coupling such as panels (c) and (d) in Fig. 3.1, the superposition of states may be destroyed. There is an interplay between the internal coupling of the AB networks and the terminal configuration, which is necessary to measure the result classically [74]. In the following four subsections each individual circuit is introduced, along with their Boolean functionality and operating parameters.

3.1. CIRCUIT I: ODD M=3 RING

The first circuit is a simple single ring with three nodes. Terminal A is the source (not to be confused with the flux input operands), and the drain outputs are (B, C) as shown in Fig. 3.1(a). The node equations of the network, as discussed in

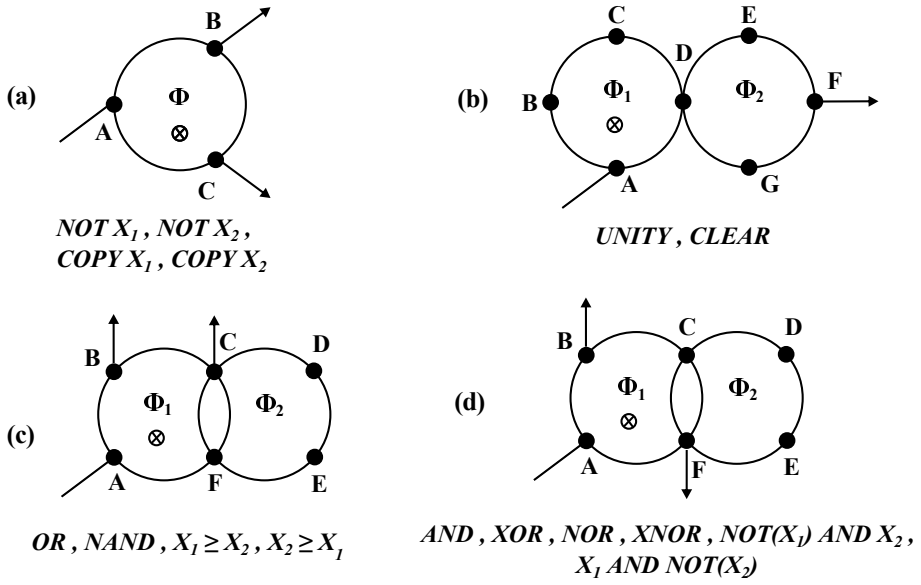

Figure 3.1: The four AB ring circuits that form a complete logic set for the sixteen Boolean operations on two binary variables X_1 and X_2. The operations each circuit can compute are listed below them. The inputs are the applied flux qubits to each ring. They are equal in magnitude but can vary by spin. The terminals are then attached in a configuration satisfying all the function rules for the four input flux states. A single ring (a) can be used for the most simple operations that have an output dependent upon only one of the inputs. (b) Point-contacted rings are suitable for functions that require the same result for all inputs over a wide flux range. (c)-(d) More complicated networks that strongly couple two rings together with two shared paths. They are capable of more complex computations due to the interaction effect between the spins. Note that while each individual flux qubit starts out in a superposed state, this interaction may destroy the superposition when bringing them together.

Sec. 2, lead to the secular equation

$$8\cos^3 ka - 6\cos ka - 2\cos 3\phi = 0. \tag{IV.2}$$

The energy band structure and persistent current are shown in Fig. 3.2. There are a total of three states (since there are three nodes), with the Fermi level E_F as the second lowest state in the half-filled situation. At zero flux, the Fermi level is sharply

Table 3.1: Summary of the four Boolean functions that the single $M = 3$ ring of Fig. 3.1(a) can perform. Due to only having a single flux input, the circuit is limited to being able to perform logic operations where one of the two inputs (X_1, X_2) are a "don't care," and thus is irrelevant to the computation. The flux mappings for the input states (in units of Φ_0) and the transmission T_B and T_C for output terminals B and C are provided.

Boolean function	$\|\Phi(state = 0,0)\rangle$	$\|0,1\rangle$	$\|1,0\rangle$	$\|1,1\rangle$
$NOT\ X_1$	$\|-0.25\rangle\ , T_C = 1$	$\|-0.25\rangle\ , T_C = 1$	$\|+0.25\rangle\ , T_C = 0$	$\|+0.25\rangle\ , T_C = 0$
$NOT\ X_2$	$\|-0.25\rangle\ , T_C = 1$	$\|+0.25\rangle\ , T_C = 0$	$\|-0.25\rangle\ , T_C = 1$	$\|+0.25\rangle\ , T_C = 0$
$COPY\ X_1$	$\|-0.25\rangle\ , T_B = 0$	$\|-0.25\rangle\ , T_B = 0$	$\|+0.25\rangle\ , T_B = 1$	$\|+0.25\rangle\ , T_B = 1$
$COPY\ X_2$	$\|-0.25\rangle\ , T_B = 0$	$\|+0.25\rangle\ , T_B = 1$	$\|-0.25\rangle\ , T_B = 0$	$\|+0.25\rangle\ , T_B = 1$

pulled up to a degenerate state and thus the flux qubit (persistent current) is in a superposition of spin-up or spin-down. However, at this flux, perturbing the system to measure the outputs is not distinct because one terminal does not dominate the transport. The electron wave is distributed at roughly 2/5 each between the two outputs, with 1/5 being reflected. This is shown in Fig. 3.3, and is not suitable for a useful readout of the circuit. By tuning the flux to $\pm\Phi_0/4$, a dominant transmission mode appears where the electron is fully transported to either B or C. So the loss of superposition is required in order to get a strong readout. This now becomes useful to perform Boolean logic. For two binary inputs X_1 and X_2, there are obviously four input states. However, since the circuit only accepts one flux input, there are limited applications to what it can process. Four Boolean operations have "don't care" logic, where the computation is dependent upon only one of the inputs: $NOT\ X_1$, $NOT\ X_2$, $COPY\ X_1$, and $COPY\ X_2$. All of these cases have a flux mapping that assigns each of the usual binary input states $|0,0\rangle$, $|0,1\rangle$, etc. for each function to the magnitude and spin of the flux qubit. For example, a NOT function can be achieved by measuring the transmission from terminals A to C. A flux input state $|0\rangle$ is set to $|-\Phi_0/4\rangle$, and $|1\rangle$ is set to $|+\Phi_0/4\rangle$. This is what is referred to as "flux mapping." A summary of these functions and their operation in the circuit are given in Table 3.1.

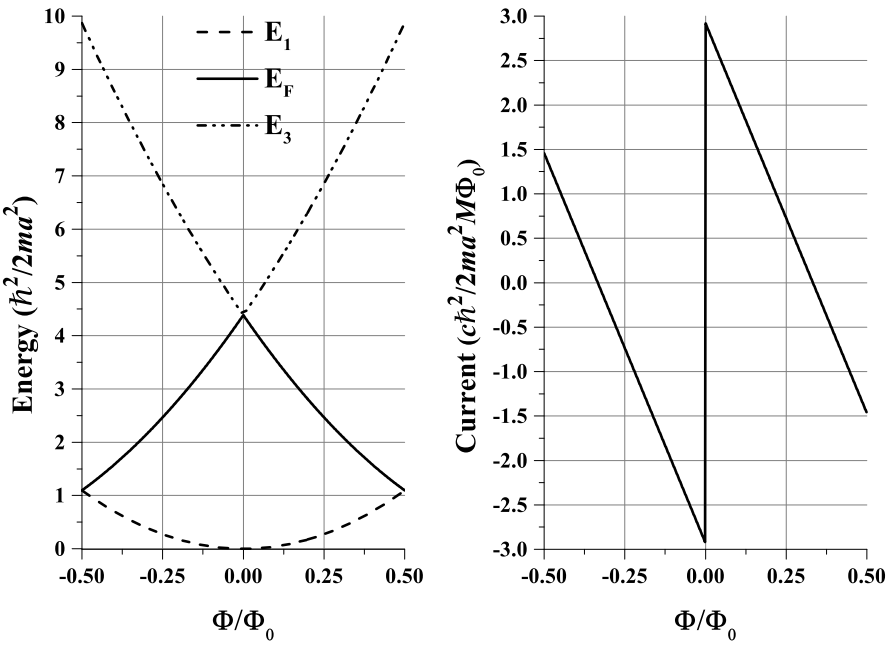

Figure 3.2: Normalized eigenenergy (left) and persistent current (right) vs. flux across the first Brillouin zone for the single $M = 3$ ring in Fig. 3.1(a). At zero flux, the spin state is in a superposition. This is a manifestation of the Fermi level E_F (second lowest state) being pulled up to a corner degeneracy with the excited state.

3.2. CIRCUIT II: EVEN POINT-CONTACTED M=4 RINGS

The second circuit is two even $M = 4$ rings that are coupled at point-contact, as shown in Fig. 3.1(b). There are two terminals with the source at A and drain output at F. There are two flux inputs to the circuit, denoted Φ_1 and Φ_2, that lead to four possible states. The node equations for this network lead to the secular equation

$$\begin{aligned} &256\cos^7 ka - 384\cos^5 ka \\ &+ (160 - 16\cos 4\phi_1 - 16\cos 4\phi_2)\cos^3 ka \\ &+ (8\cos 4\phi_1 + 8\cos 4\phi_2 - 16)\cos ka = 0 \end{aligned} \tag{IV.3}$$

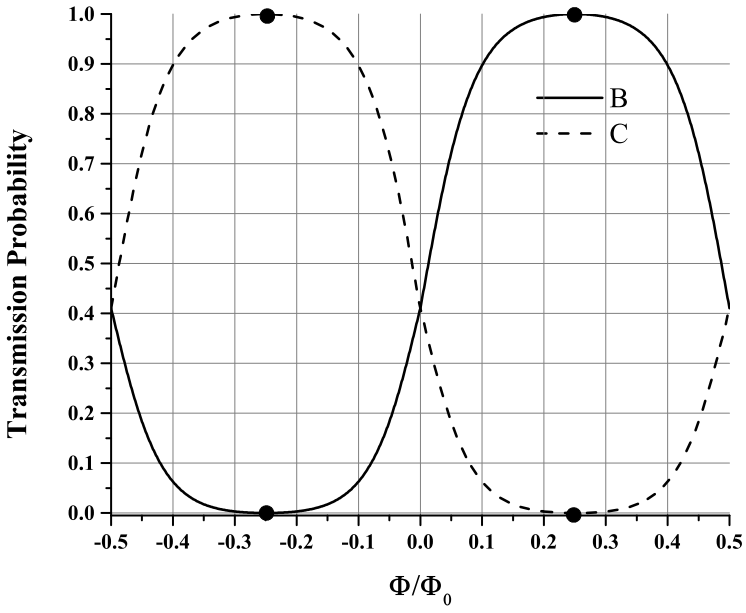

Figure 3.3: Transmission results for the single ring network of Fig. 3.1(a) whose band structure is depicted in Fig. 3.2. At $|\Phi| = \Phi_0/4$ for the spin states, there is perfect transmission to exactly one terminal. However, this comes at a loss of superposition to get a meaningful readout. At superposition (zero flux), the readout is not dominant and therefore the results of the computation are unclear. With only a single input flux to work with, this particular transmission behavior is useful for Boolean functions whose outputs depend upon only one of the two inputs. Assigning an input $|0\rangle$ or $|1\rangle$ is done arbitrarily with a "flux mapping" that satisfies all of the operation rules, as shown in Table 3.1. The flux operating points are marked by bold dots.

The energy band structure and persistent current are shown in Fig. 3.4. There are a total of seven states, with the Fermi level residing at the fourth lowest level. This state is of importance because it is flux-invariant across the entire Brillouin zone. This is a manifestation of the point-contact's weak entanglement of the flux qubits, where the band structure is identical to a single $M = 4$ ring with three extra invariant states added. The secular equation has no interacting flux cosine terms. This indicates that whether the input states of $\Phi_1 = \Phi_2$ or $\Phi_1 = -\Phi_2$ are considered, the energy

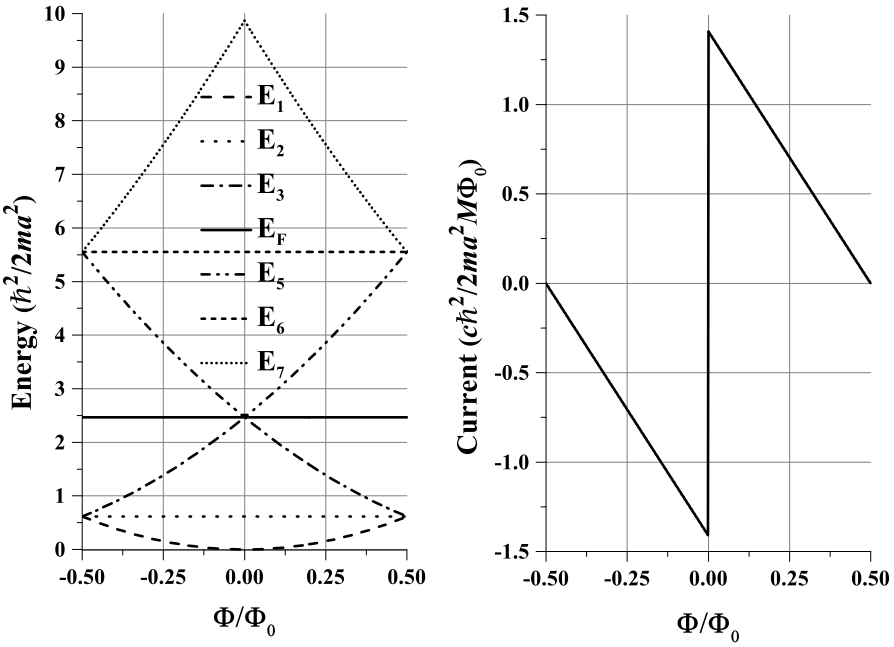

Figure 3.4: Normalized eigenenergy (left) and persistent current (right) vs. the four input flux states, denoted by (Φ_1, Φ_2), across the first Brillouin zone for the two point-contacted $M = 4$ rings in Fig. 3.1(b). Only the two spin-up and spin-down $\Phi_1 = \Phi_2 = \Phi$ states are shown, since the two $\Phi_1 = -\Phi_2$ states are identical due to the secular equation's non-interacting cosine terms. The Fermi level E_F (fourth lowest state) is flux invariant across the entire period. At zero flux, the spin state is in a superposition. This is a manifestation of the three-fold degeneracy, with the third energy level of the ground state being pulled up to a corner with E_F and the excited state.

spectrum and persistent current are the same. At zero flux there is a three-fold degeneracy at the Fermi level. The third lowest state, part of the total ground state energy, is sharply pulled up leading to a superposed persistent current. Across the entire zone, there is complete reflection of the source input wave. In this instance the transport is the same regardless of whether the system is in a superposition or not. There are two useful Boolean operations that can take advantage of this circuit: $0/CLEAR$, and $1/UNITY$. Both of these functions yield the same value regardless of the four input combinations. The output F will be used to measure $CLEAR$, and

the reflected wave will be used to measure $UNITY$. This can be accomplished with the use of a quantum circulator at the source [34]. The flux mappings for the input states can be any arbitrary values, but still need to be equal in magnitude. Taking power into consideration, as in a solenoidal setup for the fluxes, choosing a small flux operating point is desirable.

3.3. CIRCUIT III: DOUBLE-BONDED M=4 RINGS

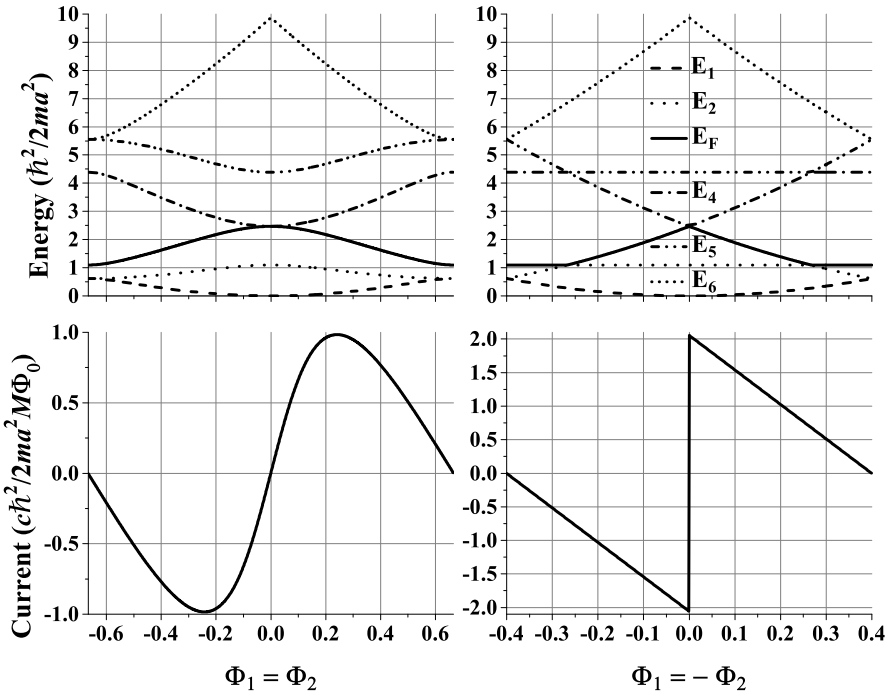

Figure 3.5: Normalized eigenenergy (top) and persistent current (bottom) vs. the four input flux states, denoted by (Φ_1, Φ_2), across the first zone for the two double-bonded $M = 4$ rings in Fig. 3.1(c)-(d). The periodicity is no longer Φ_0, but a rational number due to the circulating vector potentials. While superposition is preserved at zero flux when the fluxes differ, it is destroyed due to the strong interaction when $\Phi_1 = \Phi_2$. There is a clear pulling-up and down of the bonding and anti-bonding states, respectively. Having a strong entanglement of the spins is crucial to being able to perform more complex Boolean operations.

The third circuit is two even $M = 4$ rings that are coupled together sharing two bonds, as shown in Fig. 3.1(c). There are three terminals with the source at A

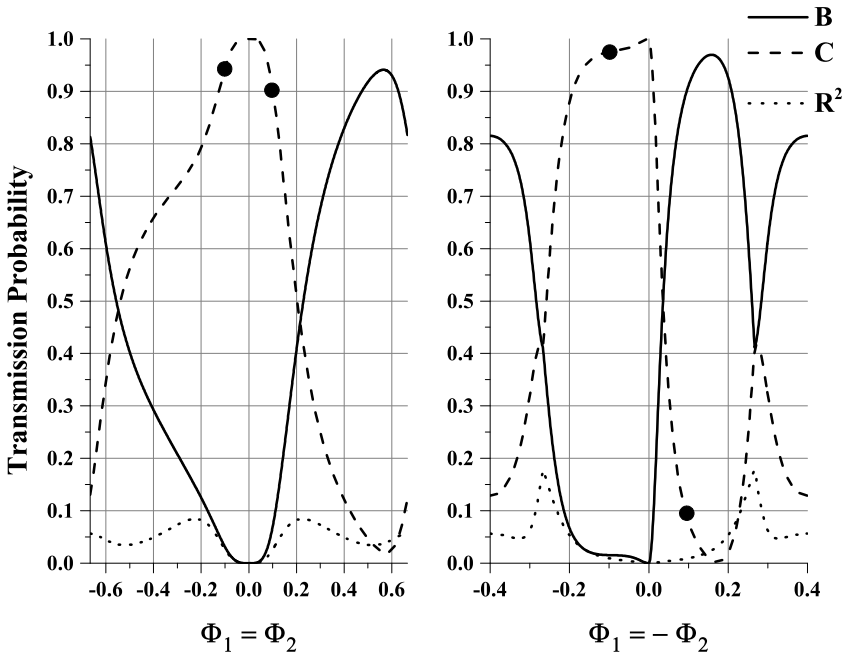

Figure 3.6: Transmission results for the two double-bonded $M = 4$ rings in Fig. 3.1(c), whose band structure is depicted in Fig. 3.5, vs. the four input flux states. Due to the strong entanglement among the spin states when $\Phi_1 = \Phi_2 = \pm 0.1\Phi_0$, terminal C can be useful when only one of the four input states needs to have a low result. Assigning the input states $\{|0,0\rangle \,..\, |1,1\rangle\}$ is done arbitrarily with a "flux mapping" that satisfies all of the operation rules, as shown in Table 3.2. The flux operating points are marked by bold dots.

and drain outputs at (B, C). There are two flux inputs to the circuit, denoted Φ_1 and Φ_2, that lead to four possible states. The node equations for this network lead to the secular equation

$$\begin{aligned} 256\cos^6 ka - 320\cos^4 ka \\ + [96 - 16\cos(4\phi_1 - \phi_2) - 16\cos(4\phi_2 - \phi_1)]\cos^2 ka \\ +4\left[\cos(4\phi_1 - \phi_2) + \cos(4\phi_2 - \phi_1)\right] \\ -2\cos 3(\phi_1 + \phi_2) - 6 = 0. \end{aligned} \tag{IV.4}$$

The energy band structure and persistent current are shown in Fig. 3.5. There are a total of six states with the Fermi level residing at the third lowest level. The cosine terms in the secular equation now have interaction between the fluxes, indicating a stronger entanglement than a point-contact situation. The periodicity of the system is altered, which for $\Phi_1 = \Phi_2$ becomes a rational number $(4/3)\Phi_0$. This is due to a change in topology where the circulating vector potentials interact along the center path. There is a pulling up of the bonding states, and pulling down of the anti-bonding states. Note that the superposition, which existed before the two rings were merged, is now destroyed even at zero flux. For the case of $\Phi_1 = -\Phi_2$, the periodicity is $(4/5)\Phi_0$. The entanglement for this case is less strong, resulting in the band structure being less distorted from the general shape of a single ring. A portion of the Fermi level is flux-invariant, where $|\Phi| > (17/64)\Phi_0$. A superposition at zero flux however does exist when the fluxes differ in spin and is a manifestation of slightly weaker entanglement. This is because when the spins are equal, the net persistent current flowing in the center common path is zero. A quarter of each ring therefore has no current. When the spins differ, the current is now doubled along this center path. Since the stronger coupling alters the band structure from that of a single ring, the transport through this three-terminal network is also more complex as a result of the interaction. This is shown in Fig. 3.6. Three terminals allow for an additional path to transmit (or dump) to, and is useful to ensure another specified output receives a low transmission. This is used to satisfy all the function rules. At small flux values, the transport is dominant through the network to one of the two outputs B or C. This allows more complicated Boolean logic to be computed. If output C is chosen, the following four operations are possible: OR, $NAND$, $X_1 \geq X_2$, and $X_2 \geq X_1$. Taking for example the function OR, there is only a single input state $|0,0\rangle$ that has an output of zero. Clearly output C satisfies this for the four different flux states at $|\Phi| = 0.1\Phi_0$, with high outputs for three states and a single state with very low

Table 3.2: Summary of the four Boolean functions that the double-bonded $M = 4$ network of Fig. 3.1(c) can perform. The flux mappings (in units of Φ_0) for the input states and the transmission T_C for output terminal C are provided.

Boolean function	$\|\Phi_1, \Phi_2(state = 0, 0)\rangle$	$\|0, 1\rangle$	$\|1, 0\rangle$	$\|1, 1\rangle$
$X_1\ OR\ X_2$	$\|+0.1, -0.1\rangle$, $T_C = 0.1$	$\|-0.1, +0.1\rangle$, $T_C = 0.95$	$\|-0.1, -0.1\rangle$, $T_C = 0.95$	$\|+0.1, +0.1\rangle$, $T_C = 0.9$
$X_1\ NAND\ X_2$	$\|-0.1, -0.1\rangle$, $T_C = 0.95$	$\|-0.1, +0.1\rangle$, $T_C = 0.95$	$\|+0.1, +0.1\rangle$, $T_C = 0.9$	$\|+0.1, -0.1\rangle$, $T_C = 0.1$
$X_1 \geq X_2$	$\|-0.1, -0.1\rangle$, $T_C = 0.95$	$\|+0.1, -0.1\rangle$, $T_C = 0.1$	$\|-0.1, +0.1\rangle$, $T_C = 0.95$	$\|+0.1, +0.1\rangle$, $T_C = 0.9$
$X_2 \geq X_1$	$\|-0.1, -0.1\rangle$, $T_C = 0.95$	$\|-0.1, +0.1\rangle$, $T_C = 0.95$	$\|+0.1, -0.1\rangle$, $T_C = 0.1$	$\|+0.1, +0.1\rangle$, $T_C = 0.9$

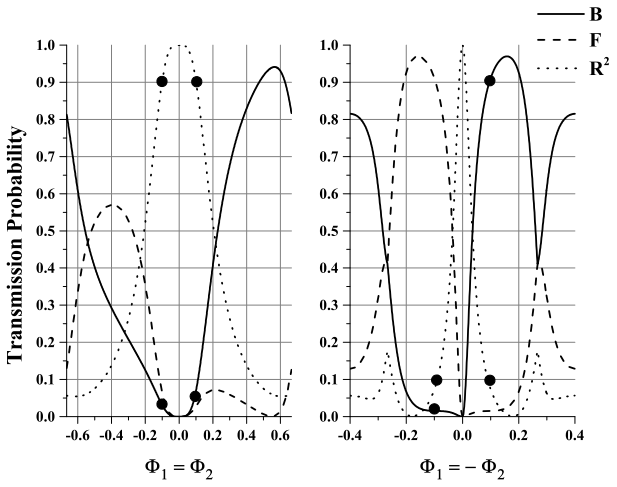

Figure 3.7: Transmission results for the two double-bonded $M = 4$ rings in Fig. 3.1(d), whose band structure is depicted in Fig. 3.5, vs. the four input flux states. Due to the strong entanglement among the spin states when $\Phi_1 = \Phi_2 = \pm 0.1\Phi_0$, it can be useful when only two of the four input states need to have a result of high or low (R^2). It can also be useful when only one of the input states needs a high result (B). Assigning the input states $\{|0, 0\rangle .. |1, 1\rangle\}$ is done arbitrarily with a "flux mapping" that satisfies all of the operation rules, as shown in Table 3.3. The flux operating points are marked by bold dots.

transmission. A summary of these four functions and their operation in the circuit are given in Table 3.2.

3.4. CIRCUIT IV: ALTERNATE DOUBLE-BONDED M=4 RINGS

The final circuit is similar to the last, with two even $M = 4$ rings that are coupled together sharing two bonds. This is shown in Fig. 3.1(d). There are three

Table 3.3: Summary of the four Boolean functions that the double-bonded $M = 4$ network of Fig. 3.1(d) can perform. The flux mappings (in units of Φ_0) for the input states, the transmission T_B for output terminal B, and reflection R^2 are provided. Here R^2 refers to source terminal A.

Boolean function	$\|\Phi_1, \Phi_2(state = 0, 0)\rangle$	$\|0, 1\rangle$	$\|1, 0\rangle$	$\|1, 1\rangle$
$X_1\ AND\ X_2$	$\|+0.1, +0.1\rangle$, $T_B = 0.05$	$\|-0.1, +0.1\rangle$, $T_B = 0.02$	$\|-0.1, -0.1\rangle$, $T_B = 0.02$	$\|+0.1, -0.1\rangle$, $T_B = 0.9$
$X_1\ XOR\ X_2$	$\|-0.1, +0.1\rangle$, $R^2 = 0.1$	$\|+0.1, +0.1\rangle$, $R^2 = 0.9$	$\|-0.1, -0.1\rangle$, $R^2 = 0.9$	$\|+0.1, -0.1\rangle$, $R^2 = 0.1$
$X_1\ NOR\ X_2$	$\|+0.1, -0.1\rangle$, $T_B = 0.9$	$\|-0.1, +0.1\rangle$, $T_B = 0.02$	$\|-0.1, -0.1\rangle$, $T_B = 0.02$	$\|+0.1, +0.1\rangle$, $T_B = 0.05$
$X_1\ XNOR\ X_2$	$\|-0.1, -0.1\rangle$, $R^2 = 0.9$	$\|-0.1, +0.1\rangle$, $R^2 = 0.1$	$\|+0.1, -0.1\rangle$, $R^2 = 0.1$	$\|+0.1, +0.1\rangle$, $R^2 = 0.9$
$X_1\ AND\ NOT(X_2)$	$\|-0.1, -0.1\rangle$, $T_B = 0.02$	$\|-0.1, +0.1\rangle$, $T_B = 0.02$	$\|+0.1, -0.1\rangle$, $T_B = 0.9$	$\|+0.1, +0.1\rangle$, $T_B = 0.05$
$NOT(X_1)\ AND\ X_2$	$\|-0.1, -0.1\rangle$, $T_B = 0.02$	$\|+0.1, -0.1\rangle$, $T_B = 0.9$	$\|-0.1, +0.1\rangle$, $T_B = 0.02$	$\|+0.1, +0.1\rangle$, $T_B = 0.05$

terminals with the source at A and drain outputs at (B, F). There are two flux inputs to the circuit, denoted Φ_1 and Φ_2, again used for the four input states. The secular equation is identical to the circuit of the previous subsection, given in Eq. (IV.4). Therefore the band structure and persistent current properties are identical between the two circuits, and differ by the external perturbation's terminal arrangement. The transport, as shown in Fig. 3.7, shows a very important capability. For the four input flux states with magnitude $0.1\Phi_0$, the source terminal has very dominant reflection for two input states, and very low reflection for the other two. No other AB network in any of the classes has a terminal configuration with this quality. This circuit has been studied before for performing half-adder addition [1]. Half-adder addition incorporates two Boolean functions, XOR (exclusive OR) for a sum bit, and AND for a carry bit. However this circuit is capable of performing four additional operations: NOR, $XNOR$, $NOT(X_1)\ AND\ X_2$, and lastly $X_1\ AND\ NOT(X_2)$. A summary of these six functions and their operation in the circuit are given in Table 3.3.

4. PRACTICAL CONSIDERATIONS

It is important to discuss some of the limitations to the toy-model (lowest-order mode) calculations provided here. In this single-particle calculation for perturbing the AB network, terminals are considered as reservoirs at infinity with a slight chemical potential difference: $E_F + \delta$, and $E_F - \delta$. In this context, we settle for an electron being perfectly incident at the source terminal. The main challenge is in fabricating the devices themselves. There have been many recent interesting developments in fabricating AB rings [6, 88, 89, 90]. Self-assembly methods have been reported [91], as well as the AB effect being demonstrated in the quantum Hall effect (QHE) regime [92]. However, having a defect-free ring with perfectly spaced scattering sites is not achievable. Moreover, the terminals themselves that measure the circuit have their own associated parasitics. The resulting inelastic scattering and localization will lead to a reduction in transmission. To deal with this dispersion, any practical device will need to have a low noise floor and a large ratio between measured logical outputs $|1\rangle$ and $|0\rangle$. In this work, a rough factor of 9 is calculated between states. The experimental basis for measuring AB oscillations in a metal ring has existed since the 80s [5]. More recent experimental setups have focused on 2DEG (electron gas) heterostructures with diameters less than a couple microns. In one experiment, an AB ring constructed from InGaAs/InAlAs with a radius of $650nm$ was studied [6]. At $T = 400mK$, the AB oscillation period corresponded to flux density $\Delta B = 2.5mT$. The phase coherence length was estimated to be $3\mu m$. A recent different approach involved a planar Si:P dopant ring [7]. The ring had an $85nm$ diameter and at $T = 100mK$ yielded a phase coherence length of $\approx 100nm$. The AB oscillation period was found to be $\Delta B \approx 670mT$. The width of the rings are kept small relative to the diameter. The circuits presented here that are coupled strongly and share two center paths could be physically represented as a single channel that is twice as wide

as the rest of the ring. An extra third terminal would then be a minor modification to the setup.

Another challenge for coupled rings is being able to individually address the input flux states to each ring. Experimentally, this would be similar to the QHE. Since the fluxes are always equal in magnitude, a 3D architecture could be employed with embedded current-controlled solenoids. Another possibility is the use of nanomagnets [8]. The "switching" of input states could then be driven by conventional microelectronics. It is generally desirable to fabricate devices to use less area and consume as little power as possible. In general, a ring that is enlarged in area can provide a larger flux for a fixed magnetic field. On the other hand, this extra area adds to cost and can lead to coherence problems if sized too large. Thus there is a tradeoff between these two competing goals.

Current microelectronics have very hard limitations due to parasitics introduced by the interconnects. These effects severely hamper switching time and power consumption for synchronous systems, in large part due to the capacitive elements charging and discharging. The QCA architecture mitigates this problem since the propagation of the signal states is through the Coulomb interaction between cells. The system operates in the ground state after a relaxation due to input boundary conditions perturbing the system. This is to negate dissipative effects with the environment. While the AB effect approach also computes in the ground state (provided the energy gap is sufficiently large), since charge is transported there is no escaping some of these parasitic issues. The measured outputs need to somehow be converted back to a flux input. This likely will consume more power than QCA arrays due to the dynamic power and charge leakage in some of the circuits with $\approx 10\%$ transmission as a "low" output. However, it could potentially be faster for the higher order logic operations. QCA still requires an array of cells, while the quantum network approach proposed here requires at most two rings. Additionally, AB rings can be

further implemented in a cellular automata framework [76]. One major advantage the AB approach has over other schemes is that the perturbation of the system itself is an integral part of the computation. While other methods may try to keep from disturbing the system, the interplay between the flux states and terminals here provides the computing mechanism for the circuit.

5. CONCLUSION

In this work, quantum networks of AB rings have been explored for sequential computing. They can potentially be used for replacing classical electronics in a smaller space. Here the focus has been to construct circuits that can perform all sixteen possible Boolean operations on two inputs. There is a total of four circuits necessary to form the entire logic set and have been shown. The inputs are the flux qubits, which can exist in a superposed state. Simple logic functions such as NOT can be computed with only a single AB ring. Higher-order logic such as $\geq$ (implication) requires two rings that are coupled, leading to an interaction between the spin states. A three-terminal configuration is necessary to perform these operations, as it provides the "switching" capability to satisfy each of the output rules. The terminal locations are adjusted in cooperation with tuning the flux. It is this interplay that actually performs the computing. While the isolated ring starts in a superposed state, the superposition must be collapsed first before any measurement for strong readouts. For coupled AB rings the possibility of superposition depends on the entanglement strength. Traditional transistor design for logic circuits relies on a truth table. When more complicated logic is needed, such as XOR, a buildup from more simple gates such as NOT is used. In the quantum network approach presented, there is no need for such a buildup. All of the Boolean functions can be achieved with a single fundamental circuit. At most, two AB rings are necessary. Discounting speedup due to decreased dimensions, the simplification of the circuit logic alone will lead to faster calculations for any sequential operation. The circuits can be resized, consistent with the scaling laws. While there are drawbacks, there are numerous advantages that this architecture potentially offers. This paper has focused on highlighting them and creating a blueprint for future work.

SECTION

2. CONCLUSIONS

The purpose of this dissertation was to undertake a more in-depth examination of Aharonov-Bohm ring quantum networks from an electronic engineering perspective. While much of the applied physics research in the field has focused on building AB devices from new materials and measuring their effects, very little work has been done in the area of circuit applications. Interferometer-type devices have been shown to be very powerful from a logic perspective since optical-based computing was introduced. As spintronic qubit-based quantum computing has struggled to become relevant from a sequential computing point of view, there is a large vacuum for a next-generation type of nanoelectronic architecture that is a natural evolution from our current CMOS technology and fabrication processes. Quantum networks have the potential to fit very well in this void due to their charge-based operation, and fabrication techniques that are not exotic since they are related to well-known superconducting devices that have been around for decades now. Low temperature on the order of hundreds of mK is a requirement for these effects to be observed and not be washed out by the thermal noise, though this is a requirement for all nanoelectronic architectures. The biggest issue to date, how to generate the magnetic fluxes in a compact and practical manner, is just now beginning to be resolved with the advent of nanomagnetic components that can be integrated on-substrate.

The first part of this dissertation focused primarily on how to characterize the fundamental modes for the various coupled quantum network classes, then relate them to higher-order scaled-up versions that will more closely mimic a fabricated device at the nanoscale. The assumptions were such that the electron waveguides are defect-free, so the partial waves elastically scatter, and the lattice is perfectly

ordered to prevent localization of the electron wave. The scaling is related to a classical rectangular waveguide where the transverse electric (TE) and transverse magnetic (TM) modes are characterized by the indices m, n. These indices relate how many half-integer wavelengths can fit within the waveguide, with the fundamental mode being one of the side lengths a or b. So the lowest-order mode corresponds to the largest size. In a quantum network, this is reversed. The minimum division of spacing is the atomic spacing l, and the lowest-order mode corresponds to the smallest fundamental network within its even or odd classification group. The higher order modes are then scaled up by odd integer factors whose transport behaviors are identical to their fundamental mode. There is an inherent finiteness on the number of nodes M in the network, and one cannot assume the $M \to \infty$ limit. This is no different than the finiteness of length for the rectangular waveguide propagation of different modes. So a mesoscopic ring consists of many 1D rings embedded within it and behaves like a TE_{mn} or TM_{mn} class at a high frequency mode or at a higher-order division of the side lengths. To demonstrate the lowest-order mode, the ring must be divided down by the atomic spacing, hence fewer 1D rings. Three distinctive classes of AB rings can then be demonstrated separately. When considering two coupled rings, there are distinct charge distribution behaviors for the eigenmodes in the different classes of networks. For a closed system, there can be two groups: even or odd. In general, even classes of networks tend to want to store more charge in the center common path. This can be adjusted by increasingly tuning the applied magnetic flux to deplete the path. However, odd classes demonstrate an opposite behavior of rejecting the storage of charge in the center path, unless tuned to a small flux range. In both situations, less than a uniform bond charge is achieved when averaging across the entire flux period. When a closed quantum network is opened (perturbed) by attaching terminals, there is a charge redistribution in the network. Normally when two rings are coupled, the electron wavefunction is spread out more.

This is at the expense of an additional scattering path which causes the forward transmission to generally suffer, leading to Anderson localization for the transport. These observations create an interesting paradox between the bond charge and the transport. Generally as the center path charge increases, the transport tends to improve. As the charge decreases, the transport tends to be reduced or the favorable transmission is restricted to a narrower flux range. Since coupled quantum networks have the ability to store charge in their shared common paths, the ability to accurately measure the circuit to determine whether a majority of charge is present or not could be useful as a memory element.

The second portion of the dissertation made a comparison of the quantum network model with two main concepts from spintronics: internal coupling interaction (entanglement) and external coupling (perturbation). In spintronics, it is expected that all of the qubits present in the system are entangled together and in a superposition of states. The interaction then between the qubits is one of the inherent mechanisms that provides the massive parallel computing potential. At the same time, the system has to be very weakly or indirectly measured, or else the system's wavefunction collapses into one well-defined classical state. Both components are considered as separate processes, with no restrictions of one to the other. The paper started with a simple quantum network (single ring) in a superposition state, and then coupled it together with another ring. At zero flux, the network is in a superposition of the four possible states. However attempting to measure the system produced an uncomputable result, with the test signal being completely reflected. The entanglement was further adjusted (bond strength) at the same time the external terminal coupling was tuned. While weak internal coupling preserves the superposition, stronger internal coupling largely destroys it. The observations were that out of the four possibilities of strong and weak internal/external couplings, only a single combination, strong internal (no superposition) and external coupling, was able to

adequately measure a computation result decisively. This finding was juxtaposed against the requirements commonly accepted for spintronics. The takeaway is that having a perfect quantum computation in a closed system first followed by reading the result turn out not to be valid for quantum networks, and therefore cannot be valid in the general case. An interplay is found between the internal coupling and the terminal configuration setup in order to observe valid logic circuit behavior.

The third segment of the dissertation was to take the standard quantum network model of ballistic transport, and then adapt the well-known Thévenin theorem principles to them. The motivation was originally to see if two phase coherent inputs could produce an equivalent circuit where the amplified transmission was greater than two. This consisted of analyzing the most basic quantum network unit, a single ring, and comparing its various classes to various coupling configurations for multi-ring networks. In typical classical electronic circuits, the equivalent configuration requirements are more relaxed due to the scalar nature of electric potential and current. However in quantum transport, the wave nature of the electron restrictions are considerably more severe. The equivalence must match the vector nature of the wavefunction, which is highly-correlated to the electron band structure and the topology of the network. In other words, the number and configuration of the scattering nodes in the network directly determine the band structure. The energy and hence the wavevectors must be the same between the equivalent models. In order to achieve this, only models that share symmetry or classifications can be considered. At the equivalent nodes, the state of the electron must be equal up to an arbitrary phase factor. In the general case the theorem does not hold, but some special case examples were provided that were able to match the requirements.

Finally, the dissertation finishes up by presenting a minimal functionally complete set of quantum network gate circuits that are able to represent all sixteen of

the Boolean algebra functions for two input variables. This was achieved by searching through all the possible two-ring coupling and terminal configurations to end up with four distinct circuits. A flux mapping scheme was employed to match each of the four logical input states with a particular input flux state that produced the desired charge transport behavior at the output terminal. Each individual circuit was then able to perform different logic operations by simply changing the flux mapping when necessary. The significance of the results are important because not only has the AB-based quantum network architecture been shown to do higher-order computation such as addition, it is also equally-capable of performing the lowest-level algebraic operations. This indicates that, at a minimum, quantum networks can logically form any device that current transistor-based logic can. This is in contrast to other quantum computing schemes, that struggle with the algebraic operations. The quantum network scheme for producing these was contrasted with some other emerging architectures such as the Quantum Cellular Automata (QCA). The major advantage quantum networks enjoy is that it is able to perform many of the more complex Boolean functions with simply two rings. The phase modulation concept and interaction between the rings provides the computing mechanism.

Quantum network-based technologies have a bright future ahead as the material science research and fabrication processes continue to advance. With the recent results of electrically long coherence lengths at reasonably achievable low temperatures, there is room to grow this field in the experimental space. Clearly quantum networks are ideally suited for sequential computing and generalized tasks. It is not intended to replace the more specialized applications of spintronics, which is aimed at highly-parallel tasks where there is no internal state-state coupling (i.e. a carry bit operation). Both can exist in the same space, but the quantum network model is

the correct platform for gaining general-purpose speedup by using quantum mechanical principles. This dissertation work has paved some of the core groundwork and concepts that can be advanced upon by researchers in the future.

APPENDIX A

NODE EQUATION DERIVATIONS FOR TRANSPORT

This appendix is meant to be a more complete set of derivations for the original theory proposed in Ref. [4]. Traditionally, quantum transport through any multiply-connected space is calculated through the scattering (S) matrix approach. For a simple network, such as single AB ring with two external terminals (two node problem), this approach is preferable. However, for more complicated networks, more nodes are involved. This is reminiscent of how classical linear circuit systems are solved. In the classical circuit theory, a given node in a circuit is associated with a linear equation based on the conservation of current (Kirchoff current law, or KCL). Therefore a corresponding quantum Kirchoff current law can be developed by reformulating the traditional S-matrix approach. In addition, one can further impose the uncertainty principle at each node for a generalization of the conservation. It is interesting to note that our node equation approach maps a quantum network into coupled and flux-modulated harmonic oscillators for the given topology. This will be further developed in this section.

A quantum network can be considered as a topology made up of nodes and bond lengths which connect those that are adjacent. In each bond length of cross section s, the Schrödinger equation must be satisfied. In the 8-node ring of Fig. 1.1(b), a node located at $x = m$ is connected with nodes $m + 1$, $m - 1$,... through bond lengths $x_{m,m+1}$, $x_{m,m-1}$,... with cross section $s_{m,m+1}$, $s_{m,m-1}$,... respectively. Along the bond length $x_{m,m+1}$, for example, the generalized 1D time-independent solution in the presence of a magnetic field is given as:

$$\hat{H}\Psi_n(x) = \left[\frac{1}{2m_e}\left(-i\hbar\nabla - \frac{e}{c}\mathbf{A}\right)^2 + eV(x)\right]\Psi_n(x) = E_n\Psi(x) \tag{A.1}$$

where $\hat{H}$ is the Hamiltonian operator, E_n are the eigenenergies for the system, and $V(x)$ is the periodic potential term for the lattice sites. The value of $x = m$ is located at node m, with positive x directed outward toward the other nodes node $m+1$, and

so on. The classical current conservation (KCL) at node m requires:

$$\sum_{\alpha} I_{m,m_\alpha} = 0 \tag{A.2}$$

In the case of the free electron (non-interaction) situation, we can assume $\forall x : V(x) = 0$. With this in mind, the general solution to Eq. (A.1) for the wavefunction between nodes m and m_α in the quantum network becomes:

$$\Psi_{m,m_\alpha}(x) = [A_{m,m_\alpha} e^{-ikx} + B_{m,m_\alpha} e^{ikx}] e^{-iS_{m,m_\alpha}(x)/\hbar} \tag{A.3}$$

where A and B are complex amplitudes, and eigenfunctions $\Psi_n(x) = e^{\pm ik_n x}$. Note that the eigenfunctions are of the exact form as the field-free Hamiltonian $\hat{H}_{FF} = -\hbar^2\nabla^2/2m_e$, but an additional phase factor $S_{m,m_\alpha}(x)/\hbar$ is now introduced for the wavefunction solution between the two nodes. Its origination can be explained due to the electromagnetic potential functions $\mathbf{A}$ and V not being unique, and hence can be transformed by using an arbitrary scalar function. If we transform from the field-free case ($\mathbf{A} = 0$), $\hat{H}_{FF}$ undergoes a unitary gauge transformation into $\hat{H}$ given in Eq. (A.1) as $\hat{U}\hat{H}_{FF}\hat{U}^{-1} = \hat{H}$, where $\hat{U}$ is given as:

$$\hat{U} = e^{i\frac{e}{\hbar}\int V dt - \frac{\mathbf{A}}{c}\cdot d\mathbf{l}} \tag{A.4}$$

with scalar potential V assumed to be zero. Any wavefunction solution $\Psi_{m,m_\alpha}(x)$ for $\hat{H}_{FF}$ is then simply transformed as:

$$\hat{U}\Psi_{m,m_\alpha}(x) = \Psi_{m,m_\alpha}(x) e^{-iS_{m,m_\alpha}(x)/\hbar} \tag{A.5}$$

The phase factor S_{m,m_α} can be defined via the relation $\mathbf{B} = \nabla \times \mathbf{A}$ and help from Stoke's theorem ($\oint_S \mathbf{B}\cdot d\mathbf{S}' = \oint_C \mathbf{A}\cdot d\mathbf{l}$) by the presence of a tangential vector potential

$\mathbf{A}(x)$ in the case of a general closed loop as:

$$S_{m,m_\alpha}(x)/\hbar = \frac{e}{\hbar c}\int_m^x \mathbf{A}(x')\cdot d\mathbf{x}' = \frac{x}{r}\left[\frac{\Phi}{\Phi_0}\right] \tag{A.6}$$

where x/r is the angular displacement in radians, and $\Phi_0 = hc/e$ in CGS units. This phenomena is known as the Aharonov-Bohm effect. With this settled, we can rewrite the wavefunction solution further:

$$\Psi_{m,m_\alpha}(x) = [(A_{m,m_\alpha}+B_{m,m_\alpha})cos(kx) - i(A_{m,m_\alpha}-B_{m,m_\alpha})sin(kx)]e^{-iS_{m,m_\alpha}(x)/\hbar} \tag{A.7}$$

Dividing through by $(A_{m,m_\alpha} + B_{m,m_\alpha})$ will yield:

$$\Psi_{m,m_\alpha}(x) = \Psi_{m,m_\alpha}(m)[cos(kx) + tan\delta_{m,m_\alpha}sin(kx)]e^{-iS_{m,m_\alpha}(x)/\hbar} \tag{A.8}$$

where we introduce the reflection coefficient $R_{m,m_\alpha} = A_{m,m_\alpha}/B_{m,m_\alpha}$ facing m as:

$$tan\delta_{m,m_\alpha} = i\left[\frac{B_{m,m_\alpha} - A_{m,m_\alpha}}{B_{m,m_\alpha} + A_{m,m_\alpha}}\right] = i\left[\frac{1 - R_{m,m_\alpha}}{1 + R_{m,m_\alpha}}\right] \tag{A.9}$$

With all terms now introduced, we may turn our attention back to the KCL condition of Eq. (A.2) for a moment. Since $I_{m,m_\alpha} = s_{m,m_\alpha}J_{m,m_\alpha}$, where J_{m,m_α} is the classical current density within the bond and s_{m,m_α} is the cross-sectional area, we can extend this concept to the quantum regime by introducing the probability current density:

$$j_{m,m_\alpha}(x) = \frac{\hbar}{2m_e i}\left[\Psi^*(x)\nabla\Psi(x) - \Psi(x)\nabla\Psi^*(x)\right] \tag{A.10}$$

We can redefine Eqs. (A.3-A.8) generally as:

$$\Psi_{m,m_\alpha}(x) = \psi_{m,m_\alpha}(x)e^{-iS_{m,m_\alpha}(x)/\hbar} \tag{A.11}$$

Therefore we are able to express Eq. (A.10) at m with use of the product rule as:

$$\begin{aligned} j_{m,m_\alpha}(m) &= \frac{\hbar}{2m_e i}\Big[\psi^*_{m,m_\alpha}(m)e^{iS_{m,m_\alpha}(m)/\hbar}(e^{-iS_{m,m_\alpha}(m)/\hbar}\psi'_{m,m_\alpha}(m) \\ &\quad -\frac{i}{\hbar}\psi_{m,m_\alpha}(m)e^{-iS_{m,m_\alpha}(m)/\hbar}S'_{m,m_\alpha}(m)) \\ &\quad -\psi_{m,m_\alpha}(m)e^{-iS_{m,m_\alpha}(m)/\hbar}(e^{iS_{m,m_\alpha}(m)/\hbar}\psi^{*\prime}_{m,m_\alpha}(m) \\ &\quad +\frac{i}{\hbar}\psi^*_{m,m_\alpha}(m)e^{iS_{m,m_\alpha}(m)/\hbar}S'_{m,m_\alpha}(m))\Big] \\ &= \frac{-\hbar}{2m_e i}\Big[\frac{i}{\hbar}\psi_{m,m_\alpha}(m)\psi^*_{m,m_\alpha}(m)S'_{m,m_\alpha}(m) \\ &\quad +\frac{i}{\hbar}\psi_{m,m_\alpha}(x)\psi^*_{m,m_\alpha}(m)S'_{m,m_\alpha}(m)\Big] \\ &= \frac{-\rho(m)}{m_e}S'_{m,m_\alpha}(m) \end{aligned} \tag{A.12}$$

where $\rho(m) = \psi_{m,m_\alpha}(m)\psi^*_{m,m_\alpha}(m)$ and is defined as the electron density. S' is said to be the momentum since the momentum operator is defined as $\hat{p} = -i\hbar\nabla$. By considering a coupling strength parameter Δ_{m,m_α} as the ratio between the cross-sectional areas, we can now write a quantum mechanical version of KCL for the probability current as the conservation of momentum:

$$\sum_\alpha \Delta_{m,m_\alpha} j_{m,m_\alpha}(m) = \sum_\alpha \Delta_{m,m_\alpha}\frac{-\rho(m)}{m_e}S'_{m,m_\alpha}(m) = 0 \tag{A.13}$$

The next task is to use this KCL expression to write a simpler set of relations that can help lead to the solution for the wavefunction at all M sites in the network. If we consider Eq. (A.10) again, it can be simplified in a slightly different way. If we divide by $\Psi_{m,m_\alpha}(x)\Psi^*_{m,m_\alpha}(x)$ it is possible to rewrite the KCL condition at node m as:

$$\frac{\hbar}{2m_e i}\sum_\alpha \Delta_{m,m_\alpha}\left[\frac{\Psi'_{m,m_\alpha}(m)}{\Psi_{m,m_\alpha}(m)} - \frac{\Psi^{*\prime}_{m,m_\alpha}(m)}{\Psi^*_{m,m_\alpha}(m)}\right] = 0 \tag{A.14}$$

By substituting Eq. (A.8) and going through a lot of manipulation, a simplified equation can be written as:

$$\sum_{\alpha} \Delta_{m,m_\alpha} \left[\frac{i}{\hbar} S'_{m,m_\alpha}(m) - k tan\delta_{m,m_\alpha} \right] = 0 \tag{A.15}$$

Since we already know from Eq. (A.13) that the momenta terms zero out on their own, we can now conclude the necessary condition that:

$$\sum_{\alpha} \Delta_{m,m_\alpha} tan\delta_{m,m_\alpha} = 0 \tag{A.16}$$

Eq. (A.15) holds up to the limit of uncertainty for the momenta of the partial waves at the site. In general, the spatial derivatives must be characterized as:

$$\sum_{\alpha} \Delta_{m,m_\alpha} \Psi'_{m,m_\alpha}(m) = \lambda\delta_m \Psi(m) \tag{A.17}$$

where $\lambda\delta_m$ represents a delta potential. In our calculations, we can assume that this potential is zero. Now we are finally in the position to write a primary node equation. By starting with Eq. (A.8), we can sum over all the connected neighbors m_α of m and enforce the KCL condition of Eq. (A.16):

$$\sum_{\alpha} \Delta_{m,m_\alpha} \Psi_{m,m_\alpha}(m_\alpha) e^{iS_{m,m_\alpha}(l)/\hbar} = (\Delta_{m,m-1} + \Delta_{m,m+1}) \Psi(m) cos(kl) \tag{A.18}$$

where $l = x_{m,\alpha}$ is the constant lattice spacing between sites m and m_α. If we settle for all coupling coefficients $\Delta_{m,m_\alpha} = 1$, then Eq. (A.18) can be simplified to a node equation connecting a given node point (m) with its neighbors:

$$2cos(kl)\Psi(m) - e^{-i\phi}\Psi(m-1) - e^{i\phi}\Psi(m+1) = 0 \tag{A.19}$$

where $\phi = (2\pi/M)(\Phi/\Phi_0)$ and M is the number of sites in the AB ring. This general solution is valid for any of the sites in the ring not connected to the external leads ($x = in$, $x = out$). At these locations the boundary conditions need to account for the extra scattering path, with phase factors $\phi = 0$ since they are outside the flux enclosed area of the AB ring. If we consider the cross sections of the ring to all be s and only the leads being of different thickness s', then $\Delta_{m,m_\alpha} = 1$ except for $\Delta_{in,lead} = \Delta_{out,lead} = s'/s$. This allows us to form:

$$\begin{aligned}
&\left[2cos(kl) - \Delta_{in,lead} tan\delta_{in,lead} sin(kl)\right] \Psi(in) - e^{i\phi}\Psi(in+1) - e^{-i\phi}\Psi(in-1) = 0 \\
&\left[2cos(kl) - \Delta_{out,lead} tan\delta_{out,lead} sin(kl)\right] \Psi(out) - e^{-i\phi}\Psi(out-1) - e^{i\phi}\Psi(out+1) = 0
\end{aligned} \tag{A.20}$$

Since path $x_{in,lead}$ is treated as the input channel, then $tan\delta_{in,lead} = i(1-R_{in,lead})/(1+R_{in,lead})$ describes the reflected component. The path $x_{out,lead}$ is considered as the output lead, therefore it is possible to impose a Bloch condition such that only an outgoing wave exists: $tan\delta_{out,lead} = -i$.

Now that the nodal equation approach has been fully developed, we can then proceed to developing the techniques for determining the transport: the local 1D Green's function approach, and the global node equation method. Both of these will be outlined in the following subsequent sections. Note that other physical models are possible to formulate with the node equation formulation, such as a single-band model where a potential is present, or semiconductor model. The form factor F in our calculations would change to accommodate the new lattice conditions. We focus on the free-electron model because it is the simplest, and gives a good approximation of the behavior.

THE SIMPLEST QUANTUM NETWORK: TWO TERMINAL AB RING

The node equation approach is indeed a partial-wave solution of the scattering event at the nodal point, just like a classical network where at each wire there is a partial current. Thus our node equation method accounts for the scattering events at each site through partial wave decomposition. This partial wave scattering will lead to Anderson localization as the number of scattering events is increased. Let us begin by considering the Hamiltonian of Eq. (A.1) again. In deriving the nodal formulations of the previous section, we have yet to consider the eigenenergies. Before we do so, we need to more precisely describe the vector potential $\mathbf{A}$. If a symmetric gauge is chosen, i.e. $\mathbf{A} = \frac{1}{2}\mathbf{B} \times \mathbf{r}$, then $\mathbf{A}$ is entirely azimuthal. This is reflected in Eq. (A.6). This allow us to define in the polar notation:

$$\mathbf{A} = \frac{\Phi}{2\pi r}\hat{\phi} \tag{A.21}$$

If we consider that our eigenfunctions $\Psi_n(x) = e^{\pm ik_n x}$ can also be written in polar form in terms of angular momenta n as $\Psi_n(\phi) = e^{\pm in\phi}$, we can simply expand the Hamiltonian to get the eigenenergies:

$$\begin{aligned}
\hat{H}\Psi_n(x) &= \frac{1}{2m_e}\left[-\frac{\hbar^2}{r^2}\frac{\partial^2}{\partial\phi^2} + \frac{i\hbar e\Phi}{r^2 c\pi}\frac{\partial}{\partial\phi} + \frac{e^2\Phi^2}{4c^2\pi^2 r^2}\right]\Psi_n(\phi) \\
&= \frac{1}{2m_e}\left[n^2\frac{\hbar^2}{r^2} - n\frac{\hbar e\Phi}{c\pi r^2} + \frac{e^2\Phi^2}{4c^2\pi^2 r^2}\right]\Psi_n(\phi) \\
&= \frac{\hbar^2}{2m_e r^2}\left(n - \frac{\Phi}{\Phi_0}\right)^2\Psi_n(\phi)
\end{aligned} \tag{A.22}$$

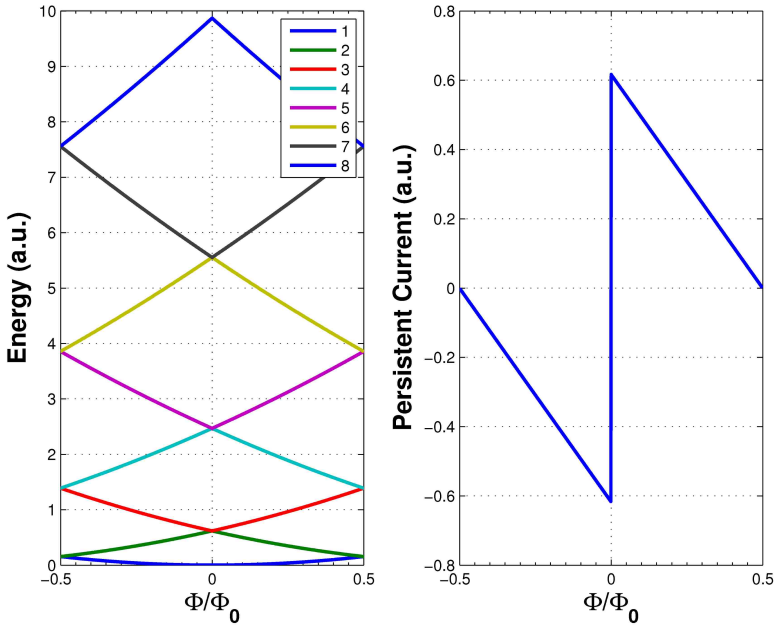

Figure A.1: Band structure (left) within the first Brillouin zone for the $M = 8$ AB ring of Fig. 1.1(b). The corresponding persistent current is shown on the right. Note that since the ground state energy is periodic, so is the persistent current.

where $k_n = (2\pi/Ml)(n - \frac{\Phi}{\Phi_0})$, $Ml = 2\pi r$ and $n = 1, 2, ...M$. This allows us to write the normalized eigenenergies and eigenfunctions as:

$$E_n = \frac{2\hbar^2\pi^2}{m_e M^2 l^2}\left(n - \frac{\Phi}{\Phi_0}\right)^2 \tag{A.23}$$

$$\Psi_n(m) = \frac{1}{\sqrt{M}} e^{\pm i\frac{2\pi}{M}mn} \tag{A.24}$$

In Fig. A.1 we plot the eigenenergies for the $M = 8$ AB ring as shown in Fig. 1.1(b). Naturally the band structure, and therefore the ground state energy, is periodic with respect to Φ_0, so as the energy levels within the band change by a single flux quantum, the angular momentum must also change by a single unit in order to stay at the same level.

The eigenenergies are important because they lead to the calculation of the persistent currents. The persistent current has been shown to be calculated as a function of the ground state energy and flux as [40]:

$$I = -c\frac{\partial E_G}{\partial \Phi} \tag{A.25}$$

where E_G is the ground state energy, or the sum of the energy levels up to the half-filled (Fermi level) situation. To see why this works, let us consider the polar form again. If we calculate the expectation value of this operator $\langle \Psi_n | - c\frac{\partial E_G}{\partial \Phi} | \Psi_n \rangle$ within the entire ring, we find:

$$\int_0^{2\pi} -c\Psi_n^*(\phi)\frac{\partial E_G}{\partial \Phi}\Psi_n(\phi) r d\phi = \int_0^{2\pi} -c\Psi_n^*(\phi)\frac{\partial \hat{H}}{\partial \mathbf{A}}\frac{\partial \mathbf{A}}{\partial \Phi}\Psi_n(\phi) r d\phi \tag{A.26}$$

assuming our wavefunctions are normalized, we can further simplify by:

$$-c\frac{\partial E_G}{\partial \Phi} = \int_0^{2\pi} -c\frac{1}{m_e}\left(-i\hbar\nabla - \frac{e}{c}\mathbf{A}\right)\left(\frac{-e}{2\pi r c}\right)\Psi_n^*(\phi)\Psi_n(\phi) r d\phi = I \tag{A.27}$$

since the integrand is the current density (velocity times charge density), and hence integrating over the entire ring must then obviously yield the total current. In Fig. A.1 we plot the persistent current corresponding to the band structure under consideration. It is important to note that when an extra electron is added to the network, there is a phase shift of $\Phi_0/2$. This causes the current to change sign. Just as the energy is periodic, the persistent current is also periodic with respect to the flux quantum since the angular momentum shifts by a single number to remain in the ground state.

With the energy and current now defined, it is possible to move on to calculating the transport for a simple two-terminal ring. We can use a Green's function

method, or perturbation method, to calculate the response of the system to an incoming electron on one of the leads. From the KCL relations we found previously, we can generally express for each site m in the network (assuming $m+1$ is clockwise, and flux is pointing into the page):

$$2F\Psi(m) - e^{-i\phi}\Psi(m-1) - e^{i\phi}\Psi(m+1) = f(m) \tag{A.28}$$

where form factor (matrix element) $F = cos(kl)$ and $m = 1, 2, ...M$ and:

$$f(m) = \delta_{m,in}[\Psi(lead_{in}) - F\Psi(in)] + \delta_{m,out}[\Psi(lead_{out}) - F\Psi(out)] \tag{A.29}$$

with perturbation terms corresponding to the wavefunctions at the leads:

$$\begin{aligned} \Psi(lead_{in}) &= \left[F + i\left(\frac{1-R}{1+R}\right) sin(kl)\right]\Psi(in) \\ \Psi(lead_{out}) &= \left[F - isin(kl)\right]\Psi(out) \end{aligned} \tag{A.30}$$

If we introduce a Green's function operator g into Eq. (A.28), we can write the general solution as:

$$2Fg(m,m') - e^{-i\phi}g(m-1,m') - e^{i\phi}g(m+1,m') = \delta_{m,m'} \tag{A.31}$$

Mathews and Walker [93] outline the general construction of the Green's function for a Hermitian operator. We will follow this approach. Generally the system can be written as:

$$2F\left|\Psi\right\rangle - \mathcal{L}\left|\Psi\right\rangle = \left|f\right\rangle \tag{A.32}$$

where $\mathcal{L}$ is the Hermitian matrix describing the phase relations for the M node equations, and $\left|\Psi\right\rangle = \left|\Psi(1), \Psi(2), ..\Psi(M)\right\rangle$ is the state describing the wavefunction at each node. If we expand $\left|\Psi\right\rangle$ and $\left|f\right\rangle$ in the eigenstates previously found in Eq.

(A.24), we end up with the result:

$$\sum_n 2c_n(F-\lambda_n)\left|\Psi_n\right\rangle = \sum_n d_n \left|\Psi_n\right\rangle \tag{A.33}$$

where $\lambda_n = cos\frac{2\pi}{M}(n-\Phi/\Phi_0)$ are the known eigenvalues for $\mathcal{L}$. The expansion coefficients c_n can then be written as:

$$c_n = \frac{d_n}{2(F-\lambda_n)} = \frac{1}{2(F-\lambda_n)}\sum_{m'}\Psi_n^*(m')f(m') \tag{A.34}$$

by taking an inner product to produce the coefficient d_n. Now that c_n is known, we can write the expansion for $\Psi(m)$:

$$\Psi(m) = \sum_n \frac{\Psi_n(m)}{2(F-\lambda_n)}\sum_{m'}\Psi_n^*(m')f(m') \tag{A.35}$$

Therefore the wavefunction solution can be written as:

$$\Psi(m) = \sum_{m'=1}^{M} g(m,m')f(m') \tag{A.36}$$

and the Green's function can be explicitly written to be:

$$g(m,m') = \frac{1}{2M}\sum_{n=1}^{M}\frac{e^{\pm i\frac{2\pi n}{M}(m-m')}}{F-cos\frac{2\pi}{M}(n-\Phi/\Phi_0)} \tag{A.37}$$

For calculating the transport, we care only about the wavefunction solutions where the leads connect to the ring, i.e. $\Psi(in)$ and $\Psi(out)$. We can therefore directly apply

Eq. (A.36):

$$\begin{aligned}\Psi(in) &= g(in,in)\left[i\left(\frac{1-R}{1+R}\right)sin(kl)\right]\Psi(in) - g(in,out)\left[isin(kl)\right]\Psi(out)\\ \Psi(out) &= g(out,in)\left[i\left(\frac{1-R}{1+R}\right)sin(kl)\right]\Psi(in) - g(out,out)\left[isin(kl)\right]\Psi(out)\end{aligned} \tag{A.38}$$

This allows one to construct a homogeneous set of linear equations in matrix form. Setting the secular equation to zero will yield the non-trivial solutions, and hence the reflection coefficient R. The transmission probability T, or $|\Psi(out)|^2$, can then be found by the simple relation $T = 1 - |R|^2$. To simplify the expression slightly, we can write $g(in,in) = g(out,out) = g(0)$, $g(out,in) = g(out-in)$, and $g(in,out) = g^*(out-in)$ since the Green's function is symmetric. We find for any arbitrary sized ring $M = L + N$,

$$R = \frac{(1-F^2)[|g(L)|^2 - g^2(0)] - 1}{(1-F^2)[|g(L)|^2 - g^2(0)] + i2\sqrt{1-F^2}g(0) + 1} \tag{A.39}$$

$$\begin{aligned}T = 4[&sin^2L\beta + sin^2N\beta + 2sin(L\beta)sin(N\beta)cos\frac{2\pi\Phi}{\Phi_0}]\Big/\\ &\Big(4[sin^2L\beta + sin^2N\beta + 2sin(L\beta)sin(N\beta)cos\frac{2\pi\Phi}{\Phi_0}]\\ &+[sin(L\beta)sin(N\beta) - 2(cos\frac{2\pi\Phi}{\Phi_0} - cosM\beta)]^2\Big)\end{aligned} \tag{A.40}$$

where $\beta = kl$. For a symmetric ring, where $L = N$, we can simplify this result into:

$$T = \frac{4\left[sin\frac{M\beta}{2}cos\frac{\pi\Phi}{\Phi_0}\right]^2}{[-\frac{5}{4}cosM\beta + cos\frac{\pi\Phi}{\Phi_0} + \frac{1}{4}]^2 + sin^2M\beta} \tag{A.41}$$

Now that the transmission have been firmly established, we can finally relate it to the overall conductance G of the channel by the well-known Landauer formula:

$$G(E) = \frac{e^2}{\pi\hbar} T(E) \tag{A.42}$$

where E is the total energy of the system. In our calculations, we assume we are at the Fermi energy E_F at $T = 0K$.

APPENDIX B

MATLAB CODE FOR TWO COUPLED AB RINGS

MAIN FUNCTION

```
function [T,R]=solution(l,m,n,bond,input,outputs,spin)

%INPUT PARAMETERS
%l,m,n are lattice spacings for left,right,center
%bond is either 's' or 'd', single or double
%input is the terminal number of input
%ter 1 is at bottom of left ring, numbering then clockwise
%outputs are ter numbers, can be [1 2..]
%spin is 'eq' or 'op'

clear all;
close all;
clc;

%determine flux period
if strcmp(spin,'op')
q=floor(1000*0.5*(l+n)/(l+2*n));
else
q=floor(1000*0.5*(l+n)/(l));
end
z=0.001*q; %normalization constant

%determine total number of atoms in network
if strcmp(bond,'d')
atoms=(l-1)+(m-1)+2*n;
```

```
else
atoms=(l-1)+(m-1)+(n+1);
end
M1=(l-1)+(n+1); %atoms in left ring
M2=(m-1)+(n+1); %atoms in right ring

%determine fermi level
f=ceil(atoms/2);

%intialize vectors
phi=zeros(1,2*q+1);
r=zeros(atoms,2*q+1);
k=zeros(atoms,2*q+1);
E=zeros(atoms,2*q+1);
T=zeros(atoms+1,2*q+1);

%compute general matrix and eigen energy coefficients
[matrix,coEff,X,phi1,phi2]=equations(l,m,n,bond);
coEff=matlabFunction(coEff);

%expansion by minors to calculate wave functions and R
syms X;
waveArray=expansion(matrix,X,input,outputs);
waveArray=matlabFunction(waveArray);
```

```
%begin varying the flux
for inc=1:2*q+1

%calculating the fluxes
phi(inc)=-z+z*(inc-1)/q;
p1=(2*pi*phi(inc))/M1;
p2=(2*pi*phi(inc))/M2;
if strcmp(spin,'op')
p2=-1*p2;
end

%substitute numerical vals for the symbolic vars
newCoeff=coEff(p1,p2);

r(:,inc)=sort(roots(newCoeff));
k(:,inc)=sort(acos(r(:,inc)));
E(:,inc)=sort(abs(k(:,inc)).^2);

%define the cos for wave vector k at fermi level
%substitute the numerical values for the symbolic vars
newWaveArray=waveArray(cos(k(f,inc)),p1,p2);

%calculate P(transmission Input->Node)
Waves(:,inc)=newWaveArray;
T(outputs,inc)=abs(newWaveArray(outputs)).^2;
R(inc)=newWaveArray(atoms+1);
```

```
disp(inc);

end

figure(1);
colordef white;
plot(phi,E(1,:),'k:','LineWidth',2); hold on;
plot(phi,E(2,:),'k','LineWidth',2); hold on;
plot(phi,E(3,:),'k–','LineWidth',2); hold on;
plot(phi,E(4,:),'k','LineWidth',6); hold on;
plot(phi,E(5,:),'k:','LineWidth',3); hold on;
plot(phi,E(6,:),'k','LineWidth',3); hold on;
plot(phi,E(7,:),'k–','LineWidth',3); hold on;
plot(phi,E(8,:),'k','LineWidth',4); hold on;
grid on;
set(gca,'XMinorTick','on');
xlabel('Normalized Magnetic Flux');
ylabel('Normalized Energy');
legend('1','2','3','E'_F,' 5',' 6',' 7',' 8');

figure(2);
for in =1:(length(phi)-1)
Etot(in)=2*E(1,in)+2*E(2,in)+2*E(3,in)+2*E(4,in);
Etd(in)=2*E(1,(in+1))+2*E(2,(in+1))+2*E(3,(in+1))+2*E(4,(in+1));
I(in)=-(Etd(in)-Etot(in))/0.001;
end
x = -z:.001:(z-.001);
```

```
plot(x,I,'b-','LineWidth',2);
ylabel('Normalized Persistent Current');
xlabel('Normalized Magnetic Flux');
axis([-z z -10 10]);
set(gca,'XMinorTick','on');
grid on;

figure(3);
plot(phi,T(outputs,:),'LineWidth',2); hold on;
plot(phi,abs(R).^2,'k','LineWidth',2); hold on;
grid on;
axis([-z z 0 1]);
set(gca,'XMinorTick','on');
xlabel('ormalized Magnetic Flux');
ylabel('ransmission Probability');

figure(4);
plot(phi,abs(Waves(5,:)),'k–','LineWidth',2); hold on;
plot(phi,abs(Waves(6,:)),'k','LineWidth',2); hold on;
plot(phi,abs(Waves(7,:)),'k:','LineWidth',2); hold on;
grid on;
set(gca,'XMinorTick','on');
xlabel('Normalized Magnetic Flux');
ylabel('Wavefunction Magnitude');
```

SUPPLEMENTAL FUNCTION: NODE EQUATION SETUP

```
function [matrix,coeff,X,phi1,phi2]=equations(l,m,n,bond)

syms X phi1 phi2;

P1=-exp(j*(phi1));
P2=-exp(-j*(phi1));
P3=-exp(j*(phi2));
P4=-exp(-j*(phi2));
P5=-exp(j*(phi1-phi2));
P6=-exp(j*(phi2-phi1));

if strcmp(bond,'d')
matrix=sym(zeros((l-1)+(m-1)+2*n));
else
matrix=sym(zeros((l-1)+(m-1)+(n+1)));
end

%fill left ring rows
for i=1:(l-1)
matrix(i,i)=2*X;
matrix(i,i+1)=P1;
if i==1
matrix(i,l+m)=P2;
else
matrix(i,i-1)=P2;
```

```
end
end

%fill right ring rows
for i=l+1:l+m-1
matrix(i,i)=2*X;
matrix(i,i+1)=P3;
matrix(i,i-1)=P4;
end

%fill top and bottom nodes of common path rows
if strcmp(bond,'d')
matrix(l,l)=4*X;
matrix(l+m,l+m)=4*X;
else
matrix(l,l)=3*X;
matrix(l+m,l+m)=3*X;
end
matrix(l,l-1)=P2;
matrix(l,l+1)=P3;
matrix(l+m,1)=P1;
matrix(l+m,l+m-1)=P4;
if n==1
if strcmp(bond,'d')
matrix(l,l+m)=2*P5;
matrix(l+m,l)=2*P6;
else
```

```
matrix(l,l+m)=P5;
matrix(l+m,l)=P6;
end

%fill middle nodes in common path rows
else %n > 1

if strcmp(bond,'d')

%fill in phases for common paths at bottom end
matrix(l+m,l+m+1)=P6;
matrix(l+m,l+m+2)=P6;

%top end
matrix(l,(l-1)+(m-1)+2*n-1)=P5;
matrix(l,(l-1)+(m-1)+2*n)=P5;

for i=l+m+1:2:(l-1)+(m-1)+2*n-1

matrix(i,i)=2*X;

if i==l+m+1
%other attached nodes first
matrix(i,i-1)=P5;
matrix(i,i+2)=P6;
```

```
%node to its right in other path
matrix(i+1,i+1)=2*X;
matrix(i+1,i-1)=P5;
matrix(i+1,i+3)=P6;

elseif i==(l-1)+(m-1)+2*n-1
%other attached nodes first
matrix(i,l)=P6;
matrix(i,i-2)=P5;

%node to its right in other path
matrix(i+1,i+1)=2*X;
matrix(i+1,l)=P6;
matrix(i+1,i-1)=P5;
else
matrix(i,i+2)=P6;
matrix(i,i-2)=P5;

matrix(i+1,i+1)=2*X;
matrix(i+1,i+3)=P6;
matrix(i+1,i-1)=P5;
end
end
else
```

```
%bottom end
matrix(l+m,l+m+1)=P6;

%top end
matrix(l,(l-1)+(m-1)+(n+1))=P5;

for i=l+m+1:(l-1)+(m-1)+(n+1)

matrix(i,i)=2*X;
matrix(i,i-1)=P5;

if i==(l-1)+(m-1)+(n+1)
matrix(i,l)=P6;
else
matrix(i,i+1)=P6;
end
end
end
end


%compute the det, extract polynomial coefficients
Det=simplify(det(matrix));
[c,t]=coeffs(Det,X);

coeff=sym(zeros(1,(l-1)+(m-1)+(n+1)+1));
```

```
for i=1:length(t)
%zero power
if t(i)==1
if strcmp(bond,'d')
coeff((l-1)+(m-1)+2*n+1)=c(i);
else
coeff((l-1)+(m-1)+(n+1)+1)=c(i);
end
else
if strcmp(bond,'d')
coeff((l-1)+(m-1)+2*n+1-coeffs(diff(t(i))))=c(i);
else
coeff((l-1)+(m-1)+(n+1)+1-coeffs(diff(t(i))))=c(i);
end
end
end
```

SUPPLEMENTAL FUNCTION: TERMINAL EXPANSION BY MINORS

```
function ret=expansion(matrix,x,input,outputs)

%EXPANSION BY MINORS FOR CALC OF WAVE FUNCTIONS
%input arguments: matrix - general matrix w/o terminals
% x - cos(ka) at fermi level
% input - terminal number of the input
% outputs - vector holding output terminal numbers
%output arguments: ret - vector holding wave functions numbered in
```

```
%successive order, with Reflected wave at end

%Need to use these for the find/nnz's that can't accept symbols
%Convert the symbols into double's with double(sym(matrix(...))
X=1;
phi1=1;
phi2=1;

%apply the output terminals to matrix
for i=1:nnz(outputs)
matrix(outputs(i),outputs(i))=matrix(outputs(i),outputs(i))+1i*sqrt(1-x.^2);
end

%determine dimensions of original matrix
[rows,cols]=size(matrix);

%find the non zeros in the input's row
nonZeros=find(double(subs(matrix(input,:))));

%define subMatrices vector
subMatrices=sym(zeros(rows-1,(cols-1)*nnz(double(subs(matrix(input,:))))));

for y=1:nnz(double(subs(matrix(input,:))))
%get the subMatrix
tempMatrix=matrix;
tempMatrix(input,:)=[];
```

```
tempMatrix(:,nonZeros(y))=[];

%add it into the vector space
subMatrices(1:rows-1,((cols-1)*(y-1)+1):((cols-1)*(y-1)+(cols-1)))=tempMatrix;

end

%now calculate D and R
num=0; %temp variable

%sum up the expansion by minor terms
for i=1:nnz(double(subs(matrix(input,:))))
%omit the input terminal cell
if nonZeros(i) =input
%check to see if we're adding or subtracting
if mod(nonZeros(i),2)==0
num=num-matrix(input,nonZeros(i))*det(subMatrices(1:(rows-1),...
((cols-1)*(i-1)+1):(cols-1)*(i)));
else
num=num+matrix(input,nonZeros(i))*det(subMatrices(1:(rows-1),...
((cols-1)*(i-1)+1):(cols-1)*(i)));
end
end
end

%if the input is odd, flip the sign of the sum of terms
if mod(input,2) =0
```

```
num=-1*num;
end

D=((num/(det(subMatrices(1:(rows-1),((cols-1)*(find(nonZeros==input)-1)+1)...
:(cols-1)*(find(nonZeros==input))))))-matrix(input,input))*1i/sqrt(1-x.^2);

R=(1-D)/(1+D);

%now calculate wave functions
waveInput=1+R;

V=matrix(:,input);
V(input,:)=[];
V=-1*V;

%solve nullSpace A*x=V for x with A \ V command
nullSpace=(subMatrices(1:(rows-1),((cols-1)*(find(nonZeros==input)-1)+1)...
:(cols-1)*(find(nonZeros==input)))) \ V;

%create a vector to hold all wave functions, with R in last cell
waveArray=sym(zeros(rows+1,1));
waveArray(rows+1)=R;
waveArray(input)=waveInput;

for i=1:rows-1
if i >= input
waveArray(i+1)=waveInput*nullSpace(i);
```

```
elseif i < input
waveArray(i)=waveInput*nullSpace(i);
end
end

%return the waveArray
ret=waveArray;
```

BIBLIOGRAPHY

[1] C. A. Cain and C. H. Wu. Electron transport through two irreducibly-coupled aharonov-bohm rings with applications to nanostructure quantum computing circuits. *J. Appl. Phys.*, 110(5):054315, 2011.

[2] Y. Aharonov and D. Bohm. Significance of electromagnetic potentials in the quantum theory. *Phys. Rev.*, 115:485–491, Aug 1959.

[3] Alastair D. McAulay. *Optical Computer Architectures*. Wiley New York, 1991.

[4] C. H. Wu and G. Mahler. Quantum network theory of transport with application to the generalized aharonov-bohm effect in metals and semiconductors. *Phys. Rev. B*, 43:5012–5023, Feb 1991.

[5] R. A. Webb, S. Washburn, C. P. Umbach, and R. B. Laibowitz. Observation of $\frac{h}{e}$ aharonov-bohm oscillations in normal-metal rings. *Phys. Rev. Lett.*, 54:2696–2699, Jun 1985.

[6] S L Ren, J J Heremans, C K Gaspe, S Vijeyaragunathan, T D Mishima, and M B Santos. Aharonov-bohm oscillations, quantum decoherence and amplitude modulation in mesoscopic ingaas/inalas rings. *Journal of Physics: Condensed Matter*, 25(43):435301, 2013.

[7] T. C. G. Reusch, A. Fuhrer, M. Fchsle, B. Weber, and M. Y. Simmons. Aharonov-bohm oscillations in a nanoscale dopant ring in silicon. *Applied Physics Letters*, 95(3):–, 2009.

[8] Yuriy G. Semenov, Xiaopeng Duan, and Ki Wook Kim. Voltage-driven magnetic bifurcations in nanomagnet-topological insulator heterostructures. *Phys. Rev. B*, 89:201405, May 2014.

[9] L. Sun et al L. DiCarlo, M. D. Reed. *Nature*, 467:574–578, 2010.

[10] J. M. Gambetta et al L. DiCarlo, J. M. Chow. *Nature*, 460:240–244, 2009.

[11] Peter W. Shor. Polynomial-time algorithms for prime factorization and discrete logarithms on a quantum computer. *SIAM J. Comput.*, 26(5):1484–1509, October 1997.

[12] Lieven M. K. Vandersypen, Matthias Steffen, Gregory Breyta, Costantino S. Yannoni, Mark H. Sherwood, and Isaac L. Chuang. Experimental realization of Shor's quantum factoring algorithm using nuclear magnetic resonance. *Nature*, 414(6866):883–887, December 2001.

[13] X.-D. Cai, C. Weedbrook, Z.-E. Su, M.-C. Chen, Mile Gu, M.-J. Zhu, Li Li, Nai-Le Liu, Chao-Yang Lu, and Jian-Wei Pan. Experimental quantum computing to solve systems of linear equations. *Phys. Rev. Lett.*, 110:230501, Jun 2013.

[14] T. Meunier, V. E. Calado, and L. M. K. Vandersypen. Efficient controlled-phase gate for single-spin qubits in quantum dots. *Phys. Rev. B*, 83:121403, Mar 2011.

[15] Thomas Monz, Philipp Schindler, Julio T. Barreiro, Michael Chwalla, Daniel Nigg, William A. Coish, Maximilian Harlander, Wolfgang Hänsel, Markus Hennrich, and Rainer Blatt. 14-qubit entanglement: Creation and coherence. *Phys. Rev. Lett.*, 106:130506, Mar 2011.

[16] A. Tonomura, N. Osakabe, T. Matsuda, T. Kawasaki, and J. Endo. *Phys. Rev. Lett.*, 56:792, 1986.

[17] S. Washburn and R. A. Webb. *Adv. Phys.*, 35:375, 1986.

[18] H. Ajiki and T. Ando. *Physica B*, 201:349, 1994.

[19] A. Tonomura. *Proc. Jpn. Acad. Ser. B: Phys. Biol. Sci.*, 82:45, 2006.

[20] R. Jackiw, A. I. Milstein, S. Y. Pi, and I. S. Terekhov. *Phys. Rev. B*, 80:033413, 2009.

[21] X. C. Xie and S. D. Sarma. *Phys. Rev. B*, 36:9326, 1987.

[22] N. Byers and C. N. Yang. *Phys. Rev. Lett.*, 7:46, 1961.

[23] H. van Houten and C. W. J. Beenakker. Quantum point contacts. *Phys. Today*, 49(7):22–27, 1996.

[24] C. W. J. Beenakker and H. van Houten. *Solid State Physics*, volume 44, chapter Quantum Transport in Semiconductor Nanostructures, pages 1–228. Academic, 1991.

[25] B. J. van Wees, H. van Houten, C. W. J. Beenakker, J. G. Williamson, L. P. Kouwenhoven, D. van der Marel, and C. T. Foxon. Quantized conductance of point contacts in a two-dimensional electron gas. *Phys. Rev. Lett.*, 60:848–850, Feb 1988.

[26] M. A. Topinka, B. J. LeRoy, R. M. Westervelt, S. E. J. Shaw, R. Fleischmann, E. J. Heller, K. D. Maranowski, and A. C. Gossard. Coherent branched flow in a two-dimensional electron gas. *Nature*, 410(6825):183–186, March 2001.

[27] M. P. Jura, M. A. Topinka, M. Grobis, L. N. Pfeiffer, K. W. West, and D. Goldhaber-Gordon. Electron interferometer formed with a scanning probe tip and quantum point contact. *Phys. Rev. B*, 80:041303, Jul 2009.

[28] P. Havu, M. J. Puska, R. M. Nieminen, and V. Havu. Electron transport through quantum wires and point contacts. *Phys. Rev. B*, 70:233308, Dec 2004.

[29] Toshihiro Itoh, Nobuyuki Sano, and Akira Yoshii. Effects of width increase in the ballistic quantum wire. *Phys. Rev. B*, 45:14131–14135, Jun 1992.

[30] T. Hatano, T. Kubo, Y. Tokura, S. Amaha, S. Teraoka, and S. Tarucha. Aharonov-bohm oscillations changed by indirect interdot tunneling via electrodes in parallel-coupled vertical double quantum dots. *Phys. Rev. Lett.*, 106:076801, Feb 2011.

[31] Saverio Russo, Jeroen B. Oostinga, Dominique Wehenkel, Hubert B. Heersche, Samira Shams Sobhani, Lieven M. K. Vandersypen, and Alberto F. Morpurgo. Observation of aharonov-bohm conductance oscillations in a graphene ring. *Phys. Rev. B*, 77:085413, Feb 2008.

[32] T. Chwiej and B. Szafran. Few-electron artificial molecules formed by laterally coupled quantum rings. *Phys. Rev. B*, 78:245306, Dec 2008.

[33] M. Flatte D. Awschalom and N. Samarth. Spintronics. *Scientific American*, 2002.

[34] C. H. Wu and Diwakar Ramamurthy. Logic functions from three-terminal quantum resistor networks for electron wave computing. *Phys. Rev. B*, 65:075313, Jan 2002.

[35] Diwakar Ramamurthy and C. H. Wu. Four-terminal quantum resistor network for electron-wave computing. *Phys. Rev. B*, 66:115307, Sep 2002.

[36] Lee Tran. Master's thesis, Missouri University of Science and Technology, 2006.

[37] S. Alexander. Superconductivity of networks. a percolation approach to the effects of disorder. *Phys. Rev. B*, 27:1541–1557, Feb 1983.

[38] R. Landauer. Electrical resistance of disordered one-dimensional lattices. *Philosophical Magazine*, 21(172):863–&, 1970.

[39] R. Landauer and M. Büttiker. *Phys. Rev. Lett.*, 54:2049, 1985.

[40] M. Büttiker, Y. Imry, and R. Landauer. *Phys. Lett.*, 96A:365, 1983.

[41] M. Büttiker, Y. Imry, and M. Ya. Azbel. Quantum oscillations in one-dimensional normal-metal rings. *Phys. Rev. A*, 30:1982–1989, Oct 1984.

[42] M. Büttiker, Y. Imry, R. Landauer, and S. Pinhas. Generalized many-channel conductance formula with application to small rings. *Phys. Rev. B*, 31:6207–6215, May 1985.

[43] M. Büttiker. Symmetry of electrical conduction. *IBM J. Res. Dev.*, 32(3):317–334, may 1988.

[44] P. W. Anderson, D. J. Thouless, E. Abrahams, and D. S. Fisher. New method for a scaling theory of localization. *Phys. Rev. B*, 22:3519–3526, Oct 1980.

[45] David P. DiVincenzo. *Fortschritte der Physik*, 48:771–783, 2000.

[46] Daniel Loss and David P. DiVincenzo. Quantum computation with quantum dots. *Phys. Rev. A*, 57:120–126, Jan 1998.

[47] Guido Burkard, Daniel Loss, and David P. DiVincenzo. Coupled quantum dots as quantum gates. *Phys. Rev. B*, 59:2070–2078, Jan 1999.

[48] R. A. Buhrman et al S. A. Wolf, D. D. Awschalom. *Science*, 294:1488–1495, 2001.

[49] A. Imamoglu, D. D. Awschalom, G. Burkard, D. P. DiVincenzo, D. Loss, M. Sherwin, and A. Small. Quantum information processing using quantum dot spins and cavity qed. *Phys. Rev. Lett.*, 83:4204–4207, Nov 1999.

[50] David D. Awschalom and Michael E. Flatte. *Nature Physics*, 3:153–159, 2007.

[51] S. E. Nigg et al M. D. Reed, L. DiCarlo. *Nature*, 482:382–385, 2012.

[52] Ronald Hanson and David D. Awschalom. *Nature*, 453:1043–1049, 2008.

[53] Ronald Hanson and Guido Burkard. Universal set of quantum gates for double-dot spin qubits with fixed interdot coupling. *Phys. Rev. Lett.*, 98:050502, Jan 2007.

[54] R. Hanson, F. M. Mendoza, R. J. Epstein, and D. D. Awschalom. Polarization and readout of coupled single spins in diamond. *Phys. Rev. Lett.*, 97:087601, Aug 2006.

[55] J. M. Elzerman, R. Hanson, J. S. Greidanus, L. H. Willems van Beveren, S. De Franceschi, L. M. K. Vandersypen, S. Tarucha, and L. P. Kouwenhoven. Few-electron quantum dot circuit with integrated charge read out. *Phys. Rev. B*, 67:161308, Apr 2003.

[56] N. Cody Jones, Rodney Van Meter, Austin G. Fowler, Peter L. McMahon, Jungsang Kim, Thaddeus D. Ladd, and Yoshihisa Yamamoto. Layered architecture for quantum computing. *Phys. Rev. X*, 2:031007, Jul 2012.

[57] L. Pauling. *J. Chem Phys.*, 4:673, 1936.

[58] C. Coulson. *Proc. Phys. Soc. (London)*, 67:608, 1954.

[59] K. Rudenberg and C. Sherr. *J. Chem. Phys.*, 21:1965, 1953.

[60] S. Alexander M. Weger and G. Della Riccia. *J. Math. Phys.*, 14:259, 1973.

[61] E. Montroll. *J. Math. Phys.*, 11:635, 1970.

[62] C. H. Wu, L. Tran, and C. A. Cain. Scaling relations and the role of bond-charge to the electron transmission through two coupled aharonov-bohm rings. *J. Appl. Phys.*, 111(9):094304, 2012.

[63] Janine Splettstoesser, Michele Governale, and Ulrich Zülicke. *Phys. Rev. B*, 68:165341, 2003.

[64] Moumita Dey, Santanu K. Maiti, and S. N. Karmakar. Spin transport through a quantum network: Effects of rashba spin-orbit interaction and aharonovbohm flux. *J. Appl. Phys.*, 109:024304, 2011.

[65] Zehao Li and L. R. Ram-Mohan. The aharonov-bohm effect with a twist: Electron transport through finite-width mobius rings. *Journal of Applied Physics*, 114(16), 2013.

[66] Feng Chi and Jun Zheng. Spin separation via a three-terminal aharonov-bohm interferometers. *Applied Physics Letters*, 92(6), 2008.

[67] M. W. Wu, J. Zhou, and Q. W. Shi. Spin-dependent quantum transport in periodic magnetic modulations: Aharonovbohm ring structure as a spin filter. *Applied Physics Letters*, 85(6):1012–1014, 2004.

[68] Cui Jiang, Wei-Jiang Gong, and Guo-Zhu Wei. Tunable spin manipulation in a quantum dot embedded in an aharonov-bohm interferometer. *Journal of Applied Physics*, 111(5), 2012.

[69] Weijiang Gong, Hui Li, Sha Zhang, and Guozhu Wei. The aharonov-bohm-fano interferometer as a spin-manipulating device. *Journal of Applied Physics*, 109(7):–, 2011.

[70] Eric R. Hedin and Yong S. Joe. Sensitive spin-polarization effects in an aharonov-bohm double quantum dot ring. *Journal of Applied Physics*, 110(2):–, 2011.

[71] Feng Chi, Jin-Long Liu, and Lian-Liang Sun. Fano-rashba effect in a double quantum dot aharonov-bohm interferometer. *Journal of Applied Physics*, 101(9):–, 2007.

[72] Ji Chen, Mansoor Bin Abdul Jalil, and Seng Ghee Tan. Spin interference in rashba metal ring in a time-dependent magnetic field. *Journal of Applied Physics*, 113(17), 2013.

[73] Leo Diago-Cisneros and Francisco Mireles. Quantum-ring spin interference device tuned by quantum point contacts. *Journal of Applied Physics*, 114(19):–, 2013.

[74] C. A. Cain and C. H. Wu. Quantum network theory of computing with respect to entangled flux qubits and external perturbation. *J. Appl. Phys.*, 113:154309, 2013.

[75] L. Thévenin. *Annales Télégraphiques (Troisieme série)*, 10:222, 1883.

[76] C.H. Wu and C.A. Cain. A non-qubit quantum adder as one-dimensional cellular automaton. *Physica E*, 59:243–247, 2014.

[77] M. Büttiker. Four-terminal phase-coherent conductance. *Phys. Rev. Lett.*, 57:1761–1764, Oct 1986.

[78] Philipp R. Struck, Heng Wang, and Guido Burkard. Nanomechanical readout of a single spin. *Phys. Rev. B*, 89:045404, Jan 2014.

[79] M. S. Tame, B. A. Bell, C. Di Franco, W. J. Wadsworth, and J. G. Rarity. Experimental realization of a one-way quantum computer algorithm solving simon's problem. *Phys. Rev. Lett.*, 113:200501, Nov 2014.

[80] Mateus Araújo, Fabio Costa, and Časlav Brukner. Computational advantage from quantum-controlled ordering of gates. *Phys. Rev. Lett.*, 113:250402, Dec 2014.

[81] Cyril Branciard, Denis Rosset, Yeong-Cherng Liang, and Nicolas Gisin. Measurement-device-independent entanglement witnesses for all entangled quantum states. *Phys. Rev. Lett.*, 110:060405, Feb 2013.

[82] N. Bonesteel and D. DiVincenzo. Quantum circuits for measuring levin-wen operators. *Phys. Rev. B*, 86:165113, Oct 2012.

[83] Nathan Wiebe, Daniel Braun, and Seth Lloyd. Quantum algorithm for data fitting. *Phys. Rev. Lett.*, 109:050505, Aug 2012.

[84] D. Kielpinski, D. Kafri, M. Woolley, G. Milburn, and J. Taylor. Quantum interface between an electrical circuit and a single atom. *Phys. Rev. Lett.*, 108:130504, Mar 2012.

[85] Vlatko Vedral, Adriano Barenco, and Artur Ekert. Quantum networks for elementary arithmetic operations. *Phys. Rev. A*, 54:147–153, Jul 1996.

[86] C S Lent, P D Tougaw, W Porod, and G H Bernstein. Quantum cellular automata. *Nanotechnology*, 4(1):49, 1993.

[87] Ho-Fai Cheung, Yuval Gefen, Eberhard K. Riedel, and Wei-Heng Shih. Persistent currents in small one-dimensional metal rings. *Phys. Rev. B*, 37:6050–6062, Apr 1988.

[88] B.C Lee, O Voskoboynikov, and C.P Lee. Iii-v semiconductor nano-rings. *Physica E: Low-dimensional Systems and Nanostructures*, 24(12):87 – 91, 2004. Proceedings of the International Symposium on Functional Semicond uctor Nanostructures 2003.

[89] Magdalena Huefner, Franoise Molitor, Arnhild Jacobsen, Alessandro Pioda, Christoph Stampfer, Klaus Ensslin, and Thomas Ihn. The aharonov-bohm effect in a side-gated graphene ring. *New Journal of Physics*, 12(4):043054, 2010.

[90] F Nichele, Y Komijani, S Hennel, C Gerl, W Wegscheider, D Reuter, A D Wieck, T Ihn, and K Ensslin. Aharonov-bohm rings with strong spin-orbit interaction: the role of sample-specific properties. *New Journal of Physics*, 15(3):033029, 2013.

[91] Takaaki Mano, Takashi Kuroda, Stefano Sanguinetti, Tetsuyuki Ochiai, Takahiro Tateno, Jongsu Kim, Takeshi Noda, Mitsuo Kawabe, Kazuaki Sakoda, Giyuu Kido, and Nobuyuki Koguchi. Self-assembly of concentric quantum double rings. *Nano Letters*, 5(3):425–428, 2005. PMID: 15755088.

[92] F. Camino, W. Zhou, and V. Goldman. Aharonov-bohm electron interferometer in the integer quantum hall regime. *Phys. Rev. B*, 72:155313, Oct 2005.

[93] Jon Mathews and Robert L. Walker. *Mathematical Methods of Physics*. W. A. Benjamin, 1970.

VITA

Casey Andrew Cain was born on September 16, 1986 in Cape Girardeau, Missouri. He attended high school in southern Illinois at Egyptian Community Unit District 5. After high school, in 2005 he moved to Rolla, Missouri to attend the University of Missouri-Rolla (now Missouri University of Science and Technology, or Missouri S&T) for Electrical and Computer Engineering. In December 2008 he earned a B.S. in Computer Engineering at Missouri S&T, and entered the defense industry workforce at Ft. Leonard Wood, Missouri. While working, he began studying toward the M.S. degree at Rolla. In 2010, he became a full-time graduate student and began research on quantum networks and novel computing technologies under the supervision of Dr. Cheng-Hsiao Wu. He completed the M.S. in Electrical Engineering at Missouri S&T in May 2011 and began working toward the Ph.D. degree in the same area. Over the course of several years, he studied various topics in advanced electromagnetics, digital circuits, solid-state physics, quantum mechanics, and numerical methods. He has taught several introductory lecture and lab courses during his graduate studies. He received the Ph.D. degree in Computer Engineering at Missouri S&T in August 2015. Casey is a member of the American Physical Society, and has published a number of peer-reviewed journal articles in his field. In his free time he enjoys hiking and the outdoors, travel and photography, shooting and hunting, as well as reading and following modern American history.